Tracking massive black hole binary mergers in highly-resolved galactic centres

---

Kate Attard
Supervisor: Alessia Gualandris
Co-Supervisor: Justin Read

Astrophysics PhD
University of Surrey
March 27, 2024

Abstract

Massive Black Holes (MBHs) are a key ingredient of the Universe, inhabiting the centers of most galaxies. Despite their abundance there is still much that is unknown about MBHs, but Gravitational Waves (GWs) offer the opportunity for new insight. MBH binary formation and coalescence follows the galactic mergers of their hosts, and these MBH mergers are responsible for the loudest GWs in the Universe. Observation of these events is possible through Pulsar Timing Array observatories, and their detection will offer a new insight into the histories of MBHs, providing information on the origin and growth of MBHs in the Universe.

Interpretations of the detected Gravitational Wave Background (GWB) signal will be aided by predictions of MBH merger statistics. In modelling individual mergers, numerical challenges arise as a high resolution is required for avoiding stochastic effects, but is difficult to achieve at the galaxy scales being modelled. First, I explore the utility of a multi-resolution scheme to preferentially increase the resolution at the centers of galaxies where MBH binaries reside. This is applied to isolated and merging models, for which I show the scheme is effective at increasing central resolution, reducing spurious relaxation and stochastic effect without adverse effects on the model stability. I continue by following each of the embedded MBH binaries to coalescence and obtaining merger timescales. I show the evolution of the orbital elements is sensitive to the resolution, improved by the use of the multi-resolution scheme at lower resolutions but still requiring high particle numbers to begin reaching convergence. Finally, I continue the analysis of the multi-resolution models with subsequent galaxy mergers, examining both new binary formation and triple interactions with an intruder MBH.

The tools developed and investigated in this thesis can be utilised in interpretation of GW detections, aiding in accurate assessments of MBH binary evolution and merger timescales.

Declaration

I confirm that the submitted work is my own work. No element has been previously submitted for assessment, or where it has, it has been correctly referenced. I have clearly identified and fully acknowledged all material that should be attributed to others (whether published or unpublished, and including any content generated by a deep learning/artificial intelligence tool, and have also included their source references where relevant) using the referencing system required by my course or in this specific assignment. I agree that the University may submit my work to means of checking this, such as the plagiarism detection service Turnitin® UK and the Turnitin® Authorship Investigate service. I confirm that I understand that assessed work that has been shown to have been plagiarised will be penalised. If in completing this work I have been assisted with its presentation by another person, I will state their name and contact details of the assistant in the 'Comments' text box below. In addition, if requested, I agree to submit the draft material that was completed solely by me prior to its presentational improvement.[1]

Parts of Chapter 3 and Chapter 4 have been submitted to the Monthly Notices of the Royal Astronomical Society (MNRAS).

---

[1] This declaration is not in my own words but was downloaded from `https://www.surrey.ac.uk/sites/default/files/2023-04/b2-regulations-for-academic-integrity-2022-2023.pdf`

Acknowledgements

I would like to thank the following people for their help throughout my PhD:

My supervisors Alessia Gualandris and Justin Read for all of their guidance and support over the course of my PhD, and who have helped me develop as a researcher.

To my family: my parents Jane and Karl, my sister Rose, and Willow. Thank you for the encouragement and for being there for me.

Tariq Hilmi, for his friendship and all the time we spent together during our PhDs. It wouldn't have been the same without you, and I'm looking forward to the trips we can take in the future.

The University of Surrey Astrophysics Group, for all of their support and kindness.

To all the people I have shared office space with over the years, with special thanks to Matthew Orkney for his invaluable advice and friendship, and to David Hendriks for all his technical help and interesting discussions.

My PhD cohort Arman Aryaeipour, Tariq Hilmi, Noushin Karim, and Sophia Lilleengen, for starting this journey together with me.

My examiners Marta Volonteri and Denis Erkal for giving their time to read this thesis and for their discussion and comments during the examination.

Contents

List of Figures

List of Tables

Introduction

1.1 Massive Black Holes

Massive black holes (MBHs) play an important role in the formation and evolution of massive galaxies and their dynamics (Kormendy & Ho, 2013), and in the era of gravitational wave astronomy, a new window has opened into the properties of astrophysical bodies and structures in the Universe. With the data collected from the currently functioning gravitational wave (GW) detector LIGO and the anticipation of future detections across the GW frequency spectrum opportunities to study astrophysical sources of GWs have arisen, from MBH binary mergers at the lower frequency end below LIGO sensitivity, to supernovae at higher frequencies (Martynov et al., 2016; Abbott et al., 2016a; Colpi et al., 2019; The LIGO Scientific Collaboration et al., 2021). Measurements of MBH coalescence will provide the means to obtain information on key physical parameters up to redshifts of $z = 2$ for detections with the Pulsar Timing Array (PTA) observatories, and beyond $z = 20$ for some MBH masses with the Laser Space Interferometer (LISA), opening the possibility to further our understanding of the formation models and following the growth of isolated MBHs and their binaries (Sesana et al., 2008b; Abbott et al., 2016b; Amaro-Seoane et al., 2017). Proposed third-generation GW detectors, such as the ground-based Einstein Telescope, will also have the ability to observe light seed MBHs out to $z = 20$ (Valiante et al., 2021). The recent low-frequency signal detection thought to be composed of GWs released by a population of merging MBHs adds to this impetus, with the anticipation that it will soon be a confirmed detection (Agazie et al., 2023b; Antoniadis et al., 2023c; Afzal et al., 2023).

Supermassive black hole binaries are the strongest source of GWs in the Universe (Peters, 1964), emitted at the final stage of inspiral. Such MBH binaries are brought together when their host galaxies merge, a scenario made common by the hierarchical formation of the Universe. Predicted to reside at the centres of most galaxies (Ferrarese & Ford, 2005), the constituent MBHs formation and growth is linked to their host galaxies. Observational relations between the galaxy and central MBH arise from their growth together, with MBH mass being associated with the stellar content of their hosts, including the velocity dispersion and bulge masses (Kormendy & Ho, 2013; Reines & Volonteri, 2015).

1.1.1 From Theory to Observations

Black holes were predicted by the equations of general relativity by Einstein (1916), the first solutions of which were derived by Schwarzschild (1916) and described a region of spacetime around a highly dense mass where the gravitational field becomes so strong that nothing can escape the surrounding event horizon boundary. Since this first prediction, many further developments have been made in understanding the properties and effects of black holes on their environment. Observed black hole masses span from $\sim 10\,\mathrm{M}_\odot$ up to $\sim 10^{10}\,\mathrm{M}_\odot$, with the lowest masses observed at $\sim 4\,\mathrm{M}_\odot$ (El-Badry et al., 2023), requiring different GW detectors to cover the potential detection range (Amaro-Seoane et al., 2017). Supermassive black holes reside at the top end of the black hole mass

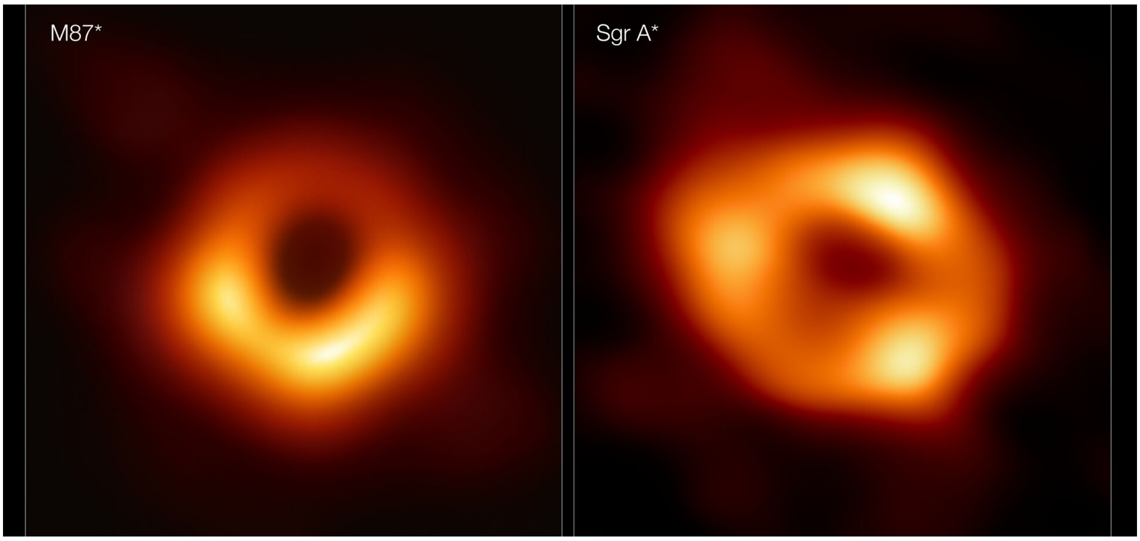

Figure 1.1: Composite images of the accretion disk emissions surrounding the black holes M87* (left) and Sagittarius A* (right), taken with the Event Horizon Telescope. Figure from Chandran (2022).

spectrum, at $M_{\rm bh} > 10^5\,{\rm M}_\odot$, and have been found at the centres of most galaxies in the Universe (Inayoshi et al., 2020; Amaro-Seoane et al., 2022).

Quasars, a highly luminous subset of Active Galactic Nuclei (AGNs), were first observed from radio measurements of a galaxy cluster that identified as originating from a new type of 'quasi-stellar' object through unfamiliar broad emission lines in the optical spectrum (Minkowski, 1960; Hazard et al., 1963; Matthews & Sandage, 1963). Further analysis developed this initial understanding through observation of their properties including high observed redshifts, implying distant objects were responsible for these luminous observations, although there was not then an explanation for the physical mechanism that could produce such a signal (Schmidt, 1963). This mechanism was then commonly established as central MBHs that powered the luminosity (as detailed further in Sec. 1.3.1) with the onset of evidence for black holes after the first accepted black hole Cygnus X-1 (Pringle & Rees, 1972; Thorne & Price, 1975). Dynamical measurements taken of the rotation and velocity dispersion of galactic nuclei via their integrated stellar spectra from analysis of the galaxies M31 and M32 revealed that there was strong evidence for a massive central object in each (Dressler & Richstone, 1988). Measurements of central MBH masses have been performed by both direct measurements of stellar orbits surrounding an MBH which allow the MBH mass to be inferred, such as by the star S2 around Sgr A* (e.g. Gillessen et al., 2009), and measurements of the broadening of AGN emission lines that can be related to the MBH mass through the reverberation mapping technique (e.g. Peterson, 1993); and via indirect methods including through the radius-luminosity relation constructed between the broad emission line region of the AGN and the optical luminosity (e.g. Bentz et al., 2006, 2009). Both observations and models show a dearth of MBHs hosted within dwarf galaxies, indicating it may not be possible for low mass galaxies form MBHs (Ferrarese et al., 2006a; Volonteri et al., 2008).

Observational confirmation of black holes finally came in the form of GW measurements from the LIGO observations of stellar mass black holes (Abbott et al., 2016a; The LIGO Scientific Collaboration et al., 2021). Central MBHs have since been established through observational evidence to be at the centres of most galaxies across the Universe, with the

MBH Sagittarius A* located at the Milky Way Galactic centre (Kormendy & Ho, 2013; GRAVITY Collaboration et al., 2018). Sagittarius A* was imaged following the first MBH imaging of M87* at the centre of Messier 87 by the Event Horizon telescope, as seen in Figure 1.1 (Goddi et al., 2019; Event Horizon Telescope Collaboration et al., 2022). Not all galaxies host central black holes however, with some notable exceptions including the galaxy M33. This potentially arises from ejections of the MBH, either in the wake of a host galaxy merger or from an earlier ejection of the MBH seed during evolution (Gebhardt et al., 2001; Askar et al., 2021).

Observations of MBHs have shown a correlation with the properties of their host galaxies, including with the bulge mass (e.g. Marconi & Hunt, 2003), and more weakly with the stellar mass (e.g. Reines & Volonteri, 2015) and the dark matter halo mass (Ferrarese, 2002) (see Section 1.4.1). MBH masses also appear to correlate with the presence of nuclear star clusters (NSCs), highly dense star clusters that are found in the central regions of galaxies. Between stellar masses of $\sim 10^8 - 10^{10}\,\mathrm{M}_\odot$ NSCs occupy galaxy centres, above which the presence of MBHs is expected, but it is not clear if this is a causal relation with several extant examples of both NSCs and MBHs co-existing in a host galaxy, including the Milky Way. Below $M_* \sim 10^8\,\mathrm{M}_\odot$, lower mass galaxies may not contain an NSC, with the nucleation fraction decreasing with decreasing host galaxy mass (Carlsten et al., 2022). NSCs may also provide a formation environment for MBHs owing to their high density (Genzel et al., 2010; Kormendy & Ho, 2013; Neumayer et al., 2020).

The place of MBHs in galaxy evolution and what we can discern via observations is an open area of study, from their origins to mergers with other high mass black holes. With constraints placed upon their final masses via measurement at early redshifts, the investigation into potential formation channels for the large observed masses is ongoing (e.g. Colpi et al., 2019; Perera et al., 2019; Amaro-Seoane et al., 2022).

1.2 Origins of Massive Black Holes

The question of MBH formation relates directly to their expected numbers and observed properties in the present day. The exact origin of how such large BHs form is uncertain; with observations of quasars at high redshifts the seeds are generally accepted to have been created at early times, with an origin at $z \sim 10 - 30$ depending on the formation method (Johnson et al., 2013). With the significance of MBHs and their exact origins remaining an open topic of investigation, future GW observations will hopefully shed light on both how these objects are seeded and their future evolution including mergers with other MBHs (e.g. Colpi et al., 2019; Perera et al., 2019; Amaro-Seoane et al., 2022).

1.2.1 MBH seeds

Currently, there are three major seed models in contention for how MBH formation occurs: seeds from Population III stars (e.g. Heger et al., 2003), from dense stellar clusters that experience core collapse with the constituent stars then forming seeds (e.g. Devecchi & Volonteri, 2009), and seeds from collapsing supermassive stars (e.g. Begelman et al., 2006). Also a possibility for seed formation are the primordial MBHs formed in the early stages of the Universe (e.g. Novikov et al., 1979). Within these scenarios, there is a distinction between the higher and lower mass seeds, with lower mass seeds requiring more effort to explain the mass growth needed to achieve the observed MBH populations (Amaro-Seoane et al., 2022). The redshifts and the resultant MBH masses of the potential seed pathways are shown in Figure 1.2.

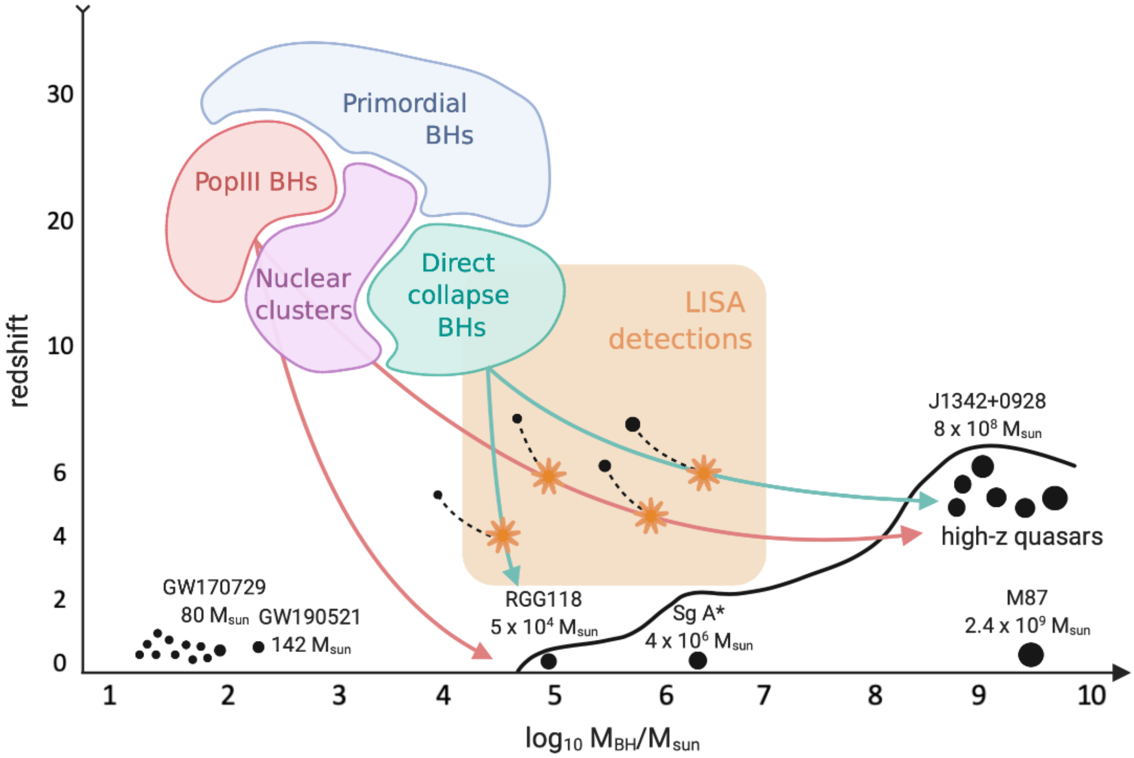

Figure 1.2: Illustration of the different formation channels theorised for MBH seeds; the collapse of Population III stars, from the collapse or coalescence of stars in dense stellar clusters, from supermassive remnant stars, and from primordial black holes. Potential LISA detections are shown within the shaded orange region, in contrast to the current detector ranges shown beneath the solid black line. Figure from Amaro-Seoane et al. (2022).

Examining each of these formation scenarios is important to determining the potential impact they will have on the resultant MBH population and their subsequent mergers, and hence the expected detection rate by GW detectors (Dayal et al., 2019; Barausse et al., 2020). Constraining seed models will reduce uncertainties in these predictions as we cannot observe the seeds at the high redshifts they would exist at (Johnson et al., 2013). The predicted populations also need to match observational constraints on numbers and masses. Subsequent MBH mass growth is discussed in Sec. 1.4.2.

Population III stars

In the Population III (Pop III) formation scenario, MBH seeds are formed when these stars collapse into a black hole in the early Universe. Pop III stars are theorised to originate from primordial gas clouds within dark matter halos that had not been enriched with heavier elements (Bond, 1981). These first-generation stars are large and generally metal-free, having formed from such early gas clouds. Direct collapse into a black hole occurs for the largest Pop III stars (at $M_\star \gtrsim 260\,\mathrm{M}_\odot$) rather than an explosion, with the MBH seed left behind suffering minimal mass loss (Madau & Rees, 2001; Heger et al., 2003; Inayoshi et al., 2020) owing to such metal-free stars being largely unable to drive stellar winds (Krtička & Kubát, 2006). The resultant MBHs formed are of the order of $10\,\mathrm{M}_\odot \lesssim M_{\mathrm{bh}} \lesssim 10^3\,\mathrm{M}_\odot$, with enough Pop III stars being predicted to form at the required high masses to drive a large present-day population of MBHs (Hirano et al., 2014; Amaro-Seoane et al., 2022).

The existence of Pop III stars is currently unproven, and they are also uncertain candidates for MBH seeds based on current observations. In order for the resulting population of Pop III seeds to match the largest MBH observations at high redshift, the seeds would need undergo rapid accretion to accrue the necessary mass. This super-Eddington accretion exceeds the Eddington rate (at which the MBH accretes mass to match the maximum luminosity at hydrostatic equilibrium), a condition it is theoretically possible for black holes to achieve with a high gas inflow present (Volonteri & Rees, 2005; Pezzulli et al., 2017; Tsai et al., 2018; Windhorst et al., 2018; Inayoshi et al., 2020).

Dense star clusters

Dense stellar clusters are formed when the gas contained in dark matter halos breaks up into smaller clumps, resulting in an environment producing closely packed star formation in the early stages of the cluster evolution (Omukai et al., 2005; Clark et al., 2008). This creates a compact collisional environment, with masses $\sim 10^5\,\mathrm{M}_\odot$ and half-mass radii $\sim 1\,\mathrm{pc}$. Within these star clusters, the creation of supermassive stars is made possible from runaway star-star collisions incited by their close proximity (Devecchi & Volonteri, 2009). The resultant supermassive stars have masses in the range of $10^2 - 10^4\,\mathrm{M}_\odot$ (Portegies Zwart & McMillan, 2002; Amaro-Seoane et al., 2022). These supermassive stars collapse into remnant MBHs at low cluster metallicities common in the early Universe, as mass loss from stellar winds increases with the metallicity (Devecchi & Volonteri, 2009; Mapelli, 2016).

Alternatively, MBH seeds can also be formed in this environment via a series of stellar-mass black hole mergers. These BHs, formed via supernova, may undergo rapid mergers with one another in the center of the cluster when enough are retained within dense clusters after their formation, or the cluster contracts after experiencing a significant gas infall (Davies et al., 2011; Giacobbo & Mapelli, 2018). A barrier to this scenario is the recoil kicks that result from these mergers have the potential to eject the MBH from the central cluster, with a retention factor of ~ 0.3 following a GW kick (Morawski et al., 2018). The MBH seeds formed from this scenario have masses of the order $10^2\,\mathrm{M}_\odot \lesssim M_\mathrm{bh} \lesssim 10^4\,\mathrm{M}_\odot$ (Davies et al., 2011; Lupi et al., 2014; Antonini et al., 2019).

Supermassive remnant stars

Seeds can also theoretically form from supermassive remnant stars (SMS), stars with masses $> 10^4\,\mathrm{M}_\odot$ that have one route of origin from a fast, high level of gas accretion onto a protostar during the formation period. For this to occur, star formation is prevented by high halo temperatures until it reaches a great enough mass at $10^7 - 10^8\,\mathrm{M}_\odot$ for the gas to collapse. The SMS is formed and evolves as a cool, red star at the center of the resulting accretion flows (Begelman et al., 2006; Smidt et al., 2018; Haemmerlé et al., 2018; Woods et al., 2021). These are most likely to form within atomic cooling halos, halos of hot gas (at virial temperatures of $T_{vir} \gtrsim 10^4\mathrm{K}$) in the early Universe that provide an ideal source of the gas necessary for this type of growth. The gas cooling within a halo that has a higher mass in comparison to the gas clouds of the Pop III scenario, and the subsequent lack of fragmentation in metal-poor early halos allows for formation of an SMS (Tanaka & Haiman, 2009; Volonteri, 2010; Becerra et al., 2015).

The SMS collapses directly into a BH once the accumulated mass in the center has reached general relativistic instability (Haemmerlé et al., 2021). In this formation channel larger MBH seeds are formed at early times, providing seed masses of $\gtrsim 10^4\,\mathrm{M}_\odot$, with some models predicting potential masses of $10^5 - 10^6\,\mathrm{M}_\odot$ (Volonteri & Begelman, 2010; Becerra et al., 2015). These masses are consistent with the large initial MBH masses predicted from observational constraints of high redshift quasars. A resulting issue in comparison to Pop III seeds is these seeds form later, and as such there less time for SMS-origin MBHs to grow, although this is at least partly mitigated by their larger initial masses (Volonteri, 2010; Johnson et al., 2013).

Primordial black holes

Finally, primordial black holes offer another pathway to MBH evolution, with their origin in the early Universe allowing them ample time to evolve to the observed MBH masses (Novikov et al., 1979; Düchting, 2004). Their formation may involve a range of different processes, each with the assumption that in an area of space with significant density fluctuations the gravitational force may outweigh the pressure, but differing as to how these formation scenarios may arise (Carr, 2003; Carr et al., 2021, and references therein for an accounting of the potential formation channels). The resultant masses occupy a range dependant on redshift they originate at, approximately at the particle horizon mass at that time. As such, those formed in e.g. the Planck epoch would have masses $\sim 10^{-5}$g, whilst those at later epochs may reach up to $10^5\,\mathrm{M}_\odot$ at 1s (Hawking, 1971; Volonteri, 2010). Although there is no current definitive observational evidence of their existence, the stochastic GWs released by small-scale perturbations at early epochs could provide a signal of primordial black holes (Carr et al., 2021). Future PTA detectors such as SKA-PTA (Square Kilometer Array), in exploring the perturbations that instigate collapse into a black hole, could provide clear evidence of primordial black holes (Orlofsky et al., 2017; Kalaja et al., 2019; Amaro-Seoane et al., 2022).

Whilst MBH seed models are still an unresolved topic of research, each model must also contend with the subsequent growth of a seed into MBHs in their host environment. Subsequent analysis into seed growth models make the distinction between heavier and lighter seeds, with masses at $M \leq 10^3\,\mathrm{M}_\odot$ being considered a light seed formed from early star remnants. The heavier seed masses are typically induced from direct formation collapse channels (Volonteri, 2010).

1.3 The Host Galaxies of Massive Black Holes

1.3.1 Galaxies in the Cosmological Context

In the Lambda Cold Dark Matter (ΛCDM) framework, structure within the Universe was formed in a hierarchical progression, with dark matter clustering under the effect of gravity to construct larger structures (White & Rees, 1978; Kauffmann et al., 1999). ΛCDM predictions are in good agreement with observations at the large-scale structure of the Universe (e.g. Dawson et al., 2013; Planck Collaboration et al., 2016, 2020).

As the dark matter halos created from clustering together accumulate gas and grow larger, the gas cools and collapses to form the stellar content of galaxies (White & Frenk, 1991). Galaxy mergers occur often over the Universe's lifetime in the hierarchical formation scenario, leading to many opportunities for MBHs hosted in these galaxies to form binaries (Begelman et al., 1980).

Dark Matter Halos

The distribution of dark matter in galaxies was historically detected through classical means, with Zwicky (1933) notably observing that the velocities of galaxies within the Coma cluster were too great to be explained by visible matter. These results were later generalised as a standard to encompass all galaxies, with the rotation curves of a range of spiral galaxies showing evidence of dark matter (Rubin & Ford, 1970; Rubin et al., 1985). Further observations then branched out to include evidence from gravitational lensing (e.g. Massey et al., 2010), anisotropies in the cosmic microwave background (CMB) (e.g. Hu & Dodelson, 2002), and other original approaches to account for the unseen mass. When measured by these techniques, DM halos have since been shown to extend beyond the area covered by the baryonic component, forming a halo encompassing the stars (Wechsler & Tinker, 2018). Dwarf galaxies typically contain a greater percentage of DM in comparison to their more massive counterparts, with observations showing high mass-to-light ratios of $10 \lesssim M/L \lesssim 1000$ for dwarf spheroidal galaxies (Walker et al., 2009; Wolf et al., 2010; Collins et al., 2013). For bright ellipticals the ratio is lower, at $5 \lesssim M/L \lesssim 10$ (Faber & Jackson, 1976; Mamon & Łokas, 2005; Cappellari et al., 2006). The Navarro-Frenk-White (NFW) profile put forward in Navarro et al. (1996) describes the DM halo density profile as

$$\rho(r) = \frac{\rho_0}{(r/r_s)(1 + r/r_s)^2} \tag{1.1}$$

where ρ_0 is the critical density of the halo, and r_s is the scale radius. It has been shown to be an effective fit to DM halos of galaxies, with a density profile that follows $\rho \propto r^{-1}$ at the centres and $\rho \propto r^{-3}$ at the outer regions (Łokas & Mamon, 2001; Shajib et al., 2021).

The Galactic Environment

The stellar component of galaxies has an important impact on the galaxy evolution. The velocities of the stars residing in the central regions of galaxies have a measured correlation to the galaxy luminosity; depending on their hosts morphology, observational relations can link the central velocity dispersion of stars, σ, and the luminosity, L. The Tully-Fisher and Faber-Jackson relations describe this correlation for spiral and elliptical galaxies respectively (Faber & Jackson, 1976; McGaugh et al., 2000). The distribution of stars at the centre of galactic halos is dependent on several factors, including galaxy morphology. Observations of stellar density profiles have shown a distinction between cores and cusps, where the surface brightness profile remains constant for a ‘cuspy’ galaxy, and exhibits a discontinuity via a flat central profile in a ‘cored’ galaxy. Bright elliptical galaxies have been observed to possess large stellar cores (Faber et al., 1997), the causes of which are discussed further in Section 1.5.1.

All galaxies are collisionless systems, which defines a system wherein the time it takes for gravitational encounters between the individual elements of the stellar population to significantly perturb a single star is longer than a Hubble time, allowing two-body interactions to be disregarded. Relaxation is a diffusive process in which the interactions between a given star and the field stars gradually deflect its velocity over successive encounters, causing a cumulative effect over time. The process induces an equipartition of energy in the galaxy in which heavier stars sink to the galaxy centre, known as mass segregation. The relaxation time can be defined for a given star by considering the time taken for two-body interactions to change a stars velocity by of order itself, given by (Binney & Tremaine, 2008)

$$t_{relax} \simeq \frac{N}{8\ln\Lambda} t_{dyn} \tag{1.2}$$

where N is the number of stars, $\ln\Lambda$ is the Coulomb logarithm, a factor equal to the logarithm of the ratio between the maximum and minimum impact parameters $\ln(b_{max}/b_{min})$, and t_{dyn} is the dynamical time - a measure of how long it takes for the star to cover a notable part of its orbit. Galaxies may contain collisional regions, such as stars within the phase-space that can interact with a central binary MBH, but these are comparatively small areas of the galaxy that are not always present, and the majority of interactions remain collisionless.

Galaxies are classified into different morphologies, with the smooth brightness profiles of elliptical galaxies standing in contrast to disk galaxies containing spiral arm structure (with or without a central bar). Giant elliptical galaxies are of note, constituting of older stars in a low-gas and dust environment (Mo et al., 2010). Their surface brightness profiles can be described well by the Sérsic profile across morphologies (Sérsic, 1963; Sersic, 1968)

$$I(r) = I_0 \exp[-b_n(r/r_s)^{1/n}] \tag{1.3}$$

where I_0 is the surface intensity, r_s is the scale radius, n is the Sérsic index, and b_n is a function of n, where $b_n \approx 2n - \frac{1}{3} + \frac{4}{405n}$ (Ciotti & Bertin, 1999). Increasing the chosen value of n yields fits suited to larger more luminous galaxies, with $n = 1$ giving an exponential profile applied to dwarfs, and $n = 4$ corresponding to elliptical galaxies as in the de Vaucouleurs profile (de Vaucouleurs, 1948; Merritt, 2013). The agreement with the observed profiles of galaxies is generally good for appropriate choices of n (Graham & Driver, 2005; Kelvin et al., 2014).

The standard Sérsic profile may no longer describe a cored galaxy profile well at the innermost densities. To compensate for this, a cored Sérsic model was conceived to describe the flattened stellar centres of bright elliptical galaxies. The original profile to introduce a move from the original cusp fitting Sérsic model was the Nuker model (Lauer et al., 1995), which describes a clean switch between the two. Later studies have since shown that this is not applicable for all galaxies (e.g. Seigar & James, 2002; Graham et al., 2003), without a connection between the outer profile and the cored region. An updated profile that compensates for this is defined by Graham & Driver (2005) as

$$I(r) = I' \left[1 + \left(\frac{r_b}{r}\right)^{\alpha}\right]^{\gamma/\alpha} \exp\left\{-b[(r^{\alpha} + r_b^{\alpha})/r_s^{\alpha}]^{1/(\alpha n)}\right\} \tag{1.4}$$

with

$$I' = I_b 2^{-(\gamma/\alpha)} \exp\left\{b(2^{1/\alpha} r_b/r_s)^{1/n}\right\} \tag{1.5}$$

where r_b describes the radius at which the density appears to 'break' and become flattened, α is a dimensionless constant for which $0 \leq \alpha \leq 1$ that serves to regulate the steepness of the transition from the original power law to the new central profile, and γ describes the logarithmic slope of the original Sérsic model. I_b here describes the intensity at the transition point between the models at r_b. This model differs from the Nuker model in its application to the entire galaxy rather than focusing on the central density, and has been shown to more accurately represent the observed profiles of cored galaxies (Trujillo et al., 2004; Ferrarese et al., 2006b).

Giant ellipticals harbour the most massive black holes at their centres (Ferrarese, 2002). They are thought to have a rich merger history through their formation via the successive major mergers of disk galaxies (De Lucia et al., 2006; Naab & Ostriker, 2017), making them of interest as sources of GWs from coalescing MBHs.

1.3.2 Large Elliptical Galaxies

Large ellipticals are spheroidal galaxies with smooth bright profiles, distinct from spirals (Larson, 1975; Mo et al., 2010). They are the largest galaxies, generally thought to form from the mergers of smaller progenitor galaxies in hierarchical models, and have been identified in observations by photometry of surface brightness profiles judged from their ellipticity (Kormendy & Djorgovski, 1989), with sizes spanning from dwarf ellipticals to supergiant galaxies (Ferguson & Binggeli, 1994; Harris et al., 1995). Ellipticals are preferentially found in galaxy clusters, a suitable environment for this mode of formation (Postman & Geller, 1984; Kormendy et al., 2009; Graham, 2013). First identified as a separate morphological classification by Hubble (1926), elliptical galaxies are further grouped as eight types denoted by En, where n increases with observed ellipticity. They are termed 'early-type' galaxies; this is a historical term referring to the morphology of galaxies, which includes ellipticals at the early end of the sequence and spirals grouped from 'early-type' to 'late-type' spirals (Binney & Tremaine, 2008).

Stellar Bulges

The stellar populations of bright ellipticals are composed of red stars; here, the 'redness' of a stellar population refers to older, more metal-rich stars being observed. These characteristics originate from the stellar formation in the early stages of the galaxy lifetime, which then experiences a subsequent dearth of star formation as the galaxies lack gas and cold dust, resulting in an ageing population (e.g. Bernardi et al., 2003). The brightness of an elliptical galaxy is correlated with the redness of the population, with the largest and most luminous galaxies possessing an older stellar composition, as illustrated in Figure 1.3 (De Lucia et al., 2006). Brighter ellipticals (at an absolute magnitude of $M_B \geq -20.5$) have been observed with cored surface brightness profiles, as discussed in Sec. 1.3.1, with the flattened interior brightness indicating a central deficit of stars. The population is bifurcated between these brighter galaxies and the fainter ellipticals, which have cuspy profiles (Kormendy et al., 2009; Graham, 2019). With photometric observations, high mass ellipticals have been observed to be frequently triaxial from evidence of 'isophote twists', wherein the major-axis position angles turn at increasing radii (Leach, 1981; Kormendy, 1982), and later observations of kinematically decoupled components, wherein the stellar core and outer radii are counter-rotating (Franx & Illingworth, 1988; Ene et al., 2018); all consistent with some degree of triaxiality for the stellar components (Neureiter et al., 2023).

The gas content of massive ellipticals is typically low, meaning they contain a dearth of star-forming environments; another contributor to the old stellar population observed (De Lucia et al., 2006; Mo et al., 2010). With a lack of gaseous material, a substantial proportion of the growth of elliptical galaxies occurs through mergers (Haehnelt & Kauffmann, 2002).

Scaling relations

Considering the shared evolution of galaxy components, it seems natural observable relations would have arisen across the galaxy lifetime. For ellipticals, one such example is the well-established Faber-Jackson relation (Sec. 1.3.1) which links the luminosity with the stellar velocity dispersion initially as $L \propto \sigma^4$ with scatter observed for lower luminosity ellipticals (Faber & Jackson, 1976; Davies et al., 1983). A later adjustment to account for the scatter in data is $L \propto \sigma^\gamma$, where γ is dependent on the size of the galaxy (Desroches et al., 2007).

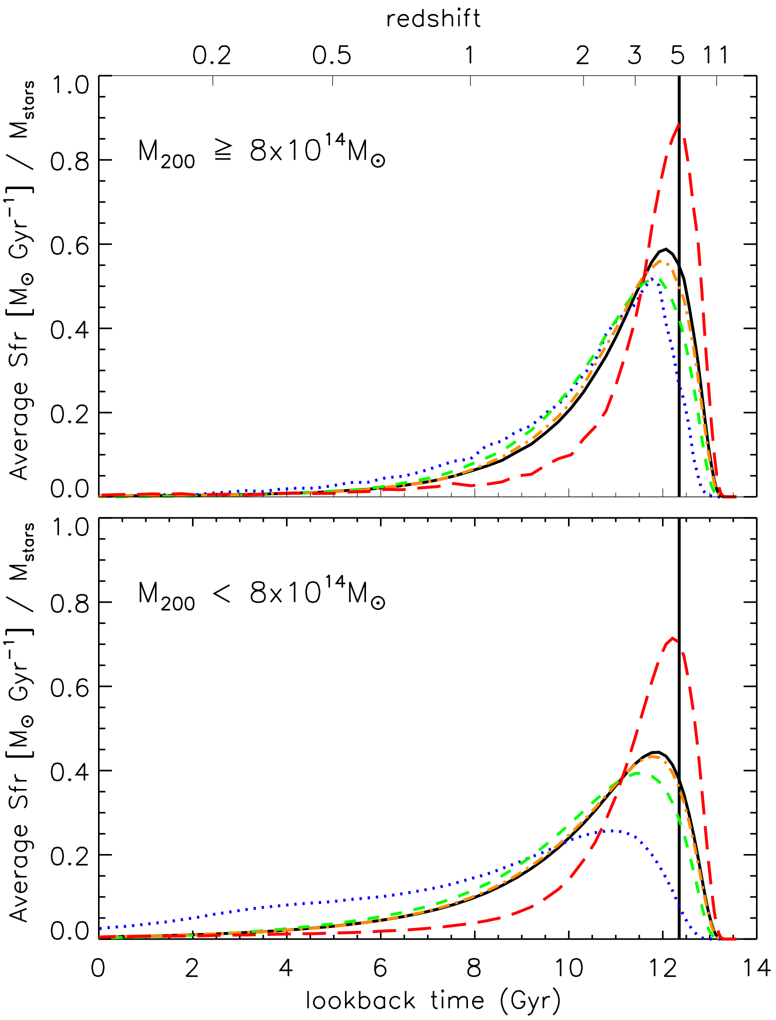

Figure 1.3: The average star formation rates of a set of elliptical galaxies from the Millennium simulation, divided by their stellar masses. The solid black line gives the average star formation, and the other lines refer to individual galaxies. The vertical line at $z = 5$ provides a comparison point. The ellipticals with greater stellar masses peak at higher redshifts with less extended time distributions. Figure from De Lucia et al. (2006).

A more recent relation to be proposed is the halo-stellar mass scaling relation, wherein the dark matter halo has been linked to the bulge for massive ellipticals (More et al., 2011; Chae et al., 2014). The relation has been presented by Behroozi et al. (2013); Moster et al. (2010), with a more recent version being given in Chae et al. (2014), identified from a sample of ∼2000 galaxies and constructed using a set of observations and abundance matching in comparison to N-body simulations. The relation is shown in Figure 1.4.

Scaling relations between the central MBH and the surrounding galaxy are indicative of their co-evolution, and are discussed further in the next section.

1.4 Observed Properties of Massive Black Holes

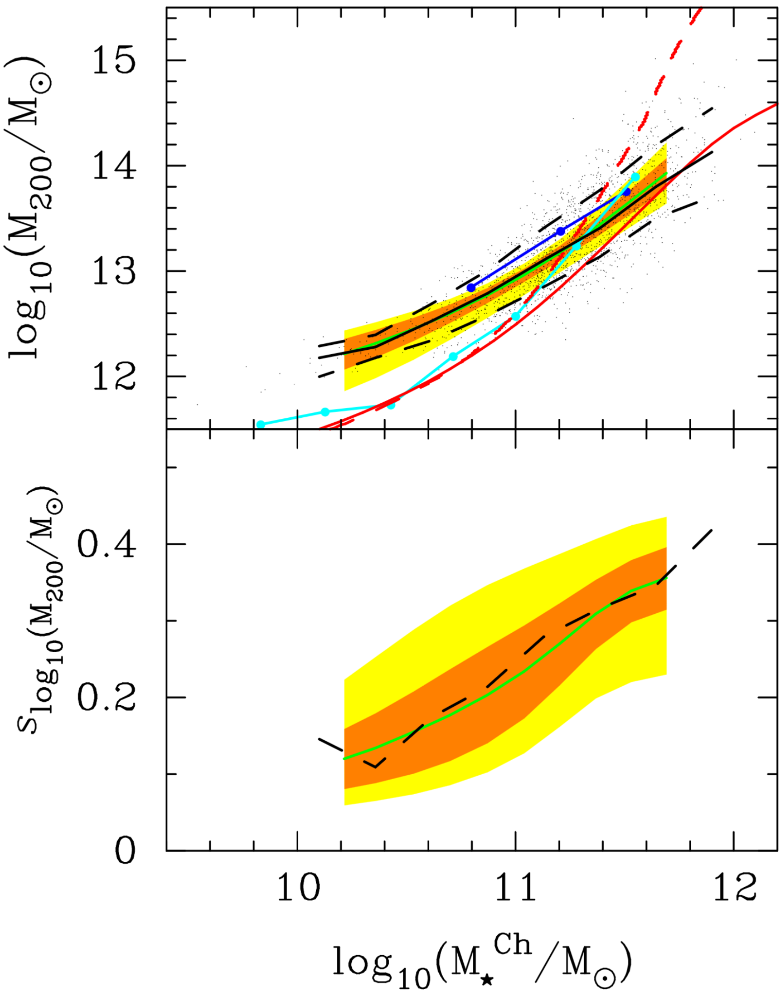

Figure 1.4: Top: Relation between the galaxy stellar mass and dark matter bulge mass, given by the solid black line for ~ 2000 modelled galaxies (black dots). The other curves represent relations from sample methods, and the orange and yellow regions show the 68% and 95% confidence ranges. Bottom: The associated intrinsic scatter of the relation, as in the top figure. Figure from Chae et al. (2014).

1.4.1 MBH-Galaxy Co-Evolution

With MBHs having been detected at the center of most local galaxies, they are considered an essential feature to modelling galaxy evolution, likely to be found in massive galaxies across the Universe (Kormendy & Ho, 2013). MBHs form part of the basic structure of a typical galaxy, alongside constituent dark matter, stars, and gas (Binney & Tremaine, 2008). The study of central MBHs is of particular importance to the current exploration of observed GWs, and as such questions about their formation and subsequent evolution need to be addressed.

Observational relations between the central MBHs and their host galaxies have been recognised, showing their influence on the development of the galaxy structure. These relations suggest the MBHs co-evolve with their host galaxies, with MBHs seeded at high redshifts (see Sec. 1.2.1) impacting the galaxy components at the central radii (Gebhardt et al., 2000; Kormendy & Ho, 2013; Reines & Volonteri, 2015). One such relation links

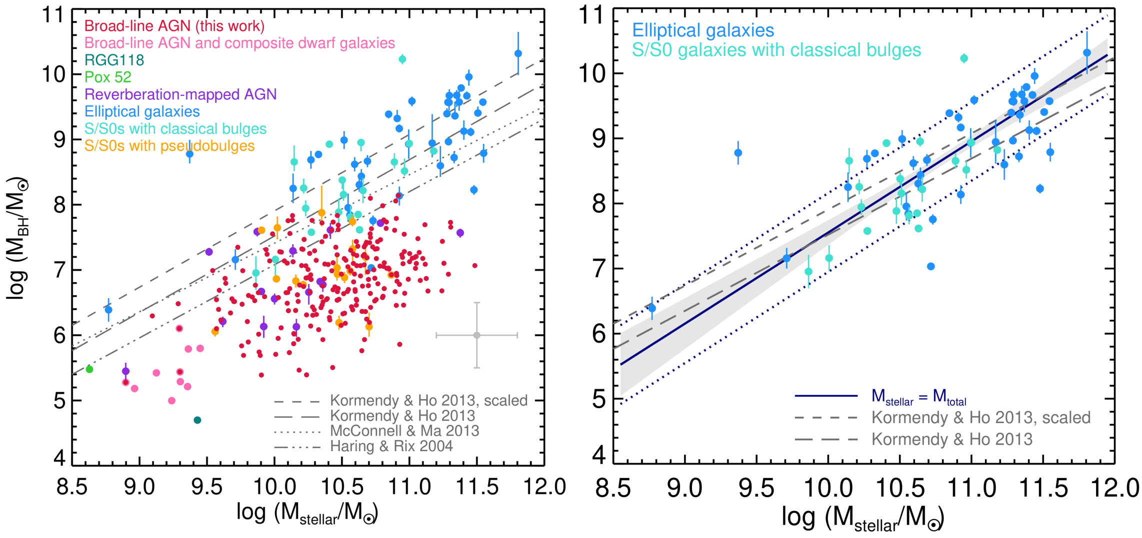

Figure 1.5: Left: The relationship between the central MBH mass and the total stellar mass of the host galaxy. The points are divided by galaxy morphology and observations, with dynamical BH mass measurements for a sample of elliptical galaxies (blue), and S/S0 galaxies with classical bulges (turquoise). The gray lines show various $M_{\rm bh} - M_{\rm b}$ relations for the galaxy morphologies. Right: As in the left panel, isolating the elliptical and S/S0 galaxies and showing the corresponding $M_{\rm bh} - M_{\rm b}$ relation with the solid dark blue line. Figure adapted from Reines & Volonteri (2015).

the central MBH masses and the stellar luminosity of their hosts, the $M_{\rm bh} - L$ relation. This luminosity can be translated to the stellar mass with the mass-to-light ratio M/L (Merritt, 2013), where the mass represents the bulge mass component of the galaxy (e.g. Beifiori et al., 2012; Kormendy & Ho, 2013).

The MBH-bulge mass relation $M_{\rm bh} - M_{\rm b}$ correlates the mass of the stars within the central bulge of a galaxy to their central MBH, the discovery of which through dynamical observations has since spawned investigation into how the relations manifest for different galaxy morphologies (and hence different evolution pathways) (e.g. Marconi & Hunt, 2003; McConnell & Ma, 2013; Reines & Volonteri, 2015). The utility of these relations is that they enable estimations of central MBHs in relation to their host galaxy as an alternative to the typical indirect measurements. For ellipticals, the bulge and the total stellar masses can be considered equivalent (Kormendy & Ho, 2013). The MBH-bulge relation for ellipticals can then be expressed as (Reines & Volonteri, 2015)

$$\log\left(\frac{M_{\rm bh}}{M_{\rm b}}\right) = \alpha + \beta \log\left(\frac{M_{\rm b}}{10^{11}\,{\rm M}_\odot}\right) \tag{1.6}$$

where $M_{\rm b}$ denotes the bulge mass. The coefficients may be set to $\alpha = 8.95 \pm 0.09$ and $\beta = 1.40 \pm 0.21$ for elliptical galaxies, taken from fits to local observations at $z \sim 0$ The elliptical $M_{\rm bh} - M_{\rm b}$ relation is shown in Figure 1.5, alongside the trends for a range of galaxy morphologies (Reines & Volonteri, 2015). The most tightly correlated fits in this relation are from early-type galaxies where star formation is dormant, including ellipticals (Beifiori et al., 2012; Savorgnan et al., 2016).

The velocity dispersion of central stars can also be linked to the MBH mass via the $M_{\rm bh} - \sigma$ relation (Gebhardt et al., 2000). This relation initially showcased a tighter

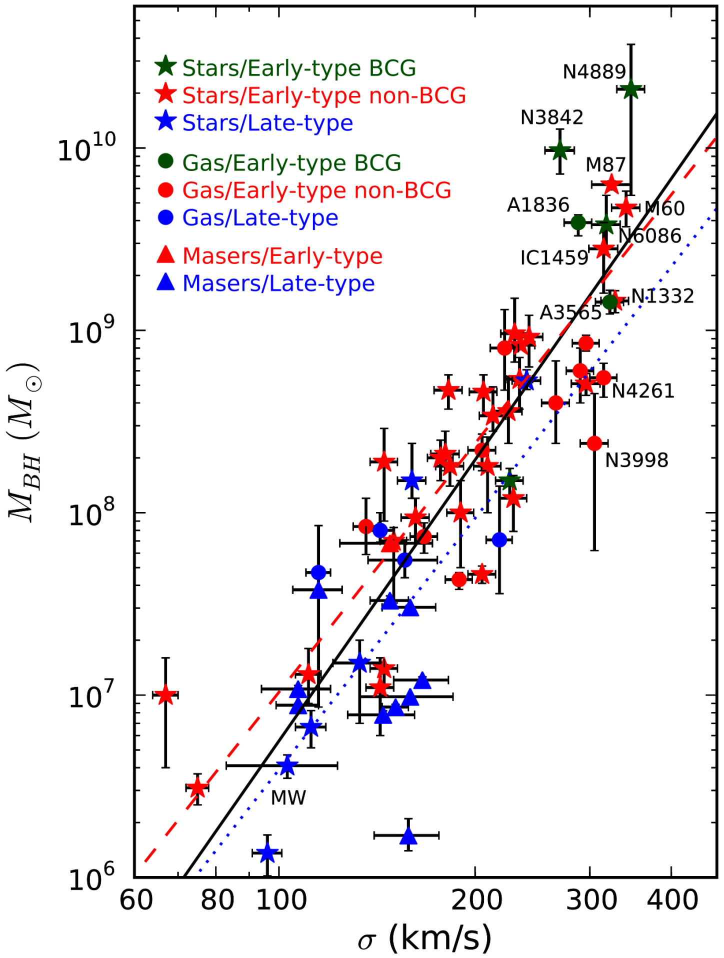

Figure 1.6: The relationship between the central MBH mass and the host galaxy stellar velocity dispersion. The points are divided by observation and galaxy type; the most luminous galaxies in a cluster (green), other elliptical and S0 galaxies (red), and late-type spiral galaxies (blue). The MBH masses are measured using the dynamics of stars (stars), gas (circles), and masers (triangles). Figure adapted from McConnell et al. (2011).

correlation than the $M_{\rm bh} - M_{\rm b}$ relation, and indicates the joint evolution between the host galaxies and MBHs. Similarly to the $M_{\rm bh} - M_{\rm b}$ relation, elliptical galaxies again show a reduced scatter in the observed data (King, 2003; Hu, 2008; Kormendy & Ho, 2013). The relation can be expressed as (McConnell et al., 2011)

$$\log\left(\frac{M_{\rm bh}}{{\rm M}_\odot}\right) = \alpha + \beta \log\left(\frac{\sigma}{200\,{\rm km\,s^{-1}}}\right) \tag{1.7}$$

where $\alpha = 8.29 \pm 0.06$ and $\beta = 5.12 \pm 0.36$ for a fit to all galaxies, and $\alpha = 8.38 \pm 0.06$ and $\beta = 4.53 \pm 0.40$ specifically considering early-type galaxies. Figure 1.6 shows the relationship between $M_{\rm bh}$ and σ for measurements of 65 galaxies.

One of the fundamental scales in a galaxy system with a central MBH is $R_{\rm infl}$, the radius of the sphere of influence of the MBH. Within this radius, the gravitational potential is dominated by the effect of the central MBH and the stars orbit on bound orbits, defined as (Peebles, 1972)

$$R_{\rm infl} = \frac{GM_{\rm bh}}{\sigma^2} \tag{1.8}$$

where G refers to the gravitational constant. Another form of the equation takes the radius of influence to be the radius at which the enclosed stellar mass is equal to twice the mass of the central MBH (Merritt, 2013)

$$R_{\mathrm{infl,m}} = R(2M_{bh}). \tag{1.9}$$

Using the first definition, the velocity dispersion at the galaxy core includes stars on wider orbits and as such compares the MBH influence with the galaxy, whilst the second compares the nearby forces with the MBH.

These relations arise from the co-evolution of central MBHs with their host galaxies, influencing their surrounding environment from early periods in the galaxy lifetime as they grow. Both experience major mergers together, and the effects of radiative feedback from AGN. As described in Sec. 1.4.3, the AGN feedback shapes the stellar population of the host galaxy through accretion flows during the early active phase. Galaxy star formation has exhibited an association with the central MBH activity, with recent studies relating the MBH mass to the star formation rate in nearby galaxies (Fabian et al., 2000; Martín-Navarro et al., 2018; Martín-Navarro & Mezcua, 2018). These relations are most significant for early-type galaxies, with a smaller scatter observed in the $M_{\mathrm{bh}} - M_{\mathrm{b}}$ and the $M_{\mathrm{bh}} - \sigma$ relations of elliptical galaxies (Gültekin et al., 2009; Kormendy & Ho, 2013; Heckman & Best, 2014).

1.4.2 Massive Black Hole Seed Growth and Feedback

MBHs grow over time through two main mechanisms: mass accretion onto the MBH, and mergers with other MBHs following galactic mergers as discussed in Section 1.5 (Begelman et al., 1980; Amaro-Seoane et al., 2022). As with the initial seed possibilities, models of the evolution of MBH populations from a chosen formation scenario must also match the MBH population observations made across cosmic time. Models of mass growth must correspond with the observations of quasars powered by MBHs of masses $\sim 10^9\,\mathrm{M}_\odot$ at the high redshift of $z \sim 7.5$ (Yang et al., 2020; Wang et al., 2021a,b).

A large contribution to MBH mass growth comes from high efficiency accretion during the quasar epoch, as determined from observations relating the accreted black hole mass to the quasar luminosity during the bright quasar phase (Soltan, 1982; Yu & Tremaine, 2002). Growth through accretion is the dominant contribution across much of the MBH lifetime, particularly for the larger MBHs where $M > 10^6\,\mathrm{M}_\odot$ beyond the earlier redshifts at $z \sim 8$. Whilst MBH mergers following galactic mergers can only contribute to the mass growth by at most a factor of 2, they can still dominate the mass growth, playing a significant role at $M < 10^5\,\mathrm{M}_\odot$ while $z > 5.5$ and at $M > 10^8\,\mathrm{M}_\odot$ while $z < 2$ (Pacucci & Loeb, 2020; Piana et al., 2021). The two mechanisms are not separate throughout the MBH lifetime, with accretion episodes following major mergers as the merger of two galaxies brings in in cold gas to the remnant galaxy (Kauffmann & Haehnelt, 2000; Li, 2012). Accretion and mergers also contribute to another observable MBH parameter alongside the mass, the spin. Observations and cosmological simulations have both suggested that the effects of mergers are less impactful to the spin evolution than gas accretion, which depend on the spins of the progenitor black holes and the alignment of the binary black hole spins with the external gas orbital angular momentum respectively (Kesden et al., 2010; Pacucci & Loeb, 2020; Dong-Páez et al., 2023).

Light seeds require a large growth to match such observations of MBHs seen at the earliest redshifts. Beginning from masses of $M \leq 10^3\,\mathrm{M}_\odot$, they must maintain near-Eddington accretion rates for an extended period of time to reach the bright quasar numbers of observations, but only a fraction of such seeds would need to reach high rates to match the later populations of MBHs (Haiman & Loeb, 2001; Greif et al., 2008). This would require overcoming the difficulties of reaching such high accretion rates, and even with some achieving near-Eddington accretion rates it is unlikely a seed population with such initial masses could replicate later MBH populations (Pacucci et al., 2017; Smith et al., 2018). Another possibility for such growth is the MBH reaching super-Eddington accretion rates at which the mass inflow would be very rapid, under the circumstances where the MBH has continuous access to a high gas reservoir, making it possible to reach the necessary masses at early times (Volonteri et al., 2015; Pezzulli et al., 2016; Smith et al., 2018; Regan et al., 2019). Pop III seeds, at their smaller masses, also do not initially sink to the centers of host galaxies; instead they are considered wandering black holes within a galaxy until their growth has reached a critical mass of at least $\sim 10^5\,\mathrm{M}_\odot$ (Bellovary et al., 2019; Greene et al., 2020). By contrast the heavier MBH seeds do not face such a growth barrier, and hence avoid the issues associated with such growth requirements.

Feedback plays a role in many different galaxy processes, and similarly within MBH mergers affects the accretion rate and hence the resultant mass. The feedback generated by supernovae impacts the supply of cold gas in galaxies, particularly in lower mass galaxies with $M_\star \lesssim 10^{10}\,\mathrm{M}_\odot$, removing gas with strong winds driven by the supernova. With less gas in the surrounding environment, it reduces the accretion onto seeds and hence regulates the potential mass growth (Dubois et al., 2014, 2015; Habouzit et al., 2017). The feedback generated by the MBH also affects the seed growth, with the jets produced by AGN (as described in Sec. 1.3.1) removing surrounding gas from within 1 pc around the black hole. This limits the accretion rate that can be attained by the seed, with the internal MBH feedback regulating the growth by $0.1 - 0.5$ times the Eddington accretion rate (Johnson & Bromm, 2007; Volonteri, 2010; Regan et al., 2019; Toyouchi et al., 2023).

1.4.3 Central MBHs and Feedback

Stars in close proximity to the central MBH of a galaxy will have a mutual effect on one another, beginning from the early era of galaxies hosting Active Galactic Nuclei (AGNs). AGN are highly dense, luminous central regions of a galaxy that can be observed in galaxies at high redshift owing to their brightness. Quasars are the most luminous subset of AGN, with observations at high redshift providing a means to examine the formation of the MBHs that drives them (Begelman et al., 1984; Wang et al., 2021b). Within AGN, the central MBH is surrounded by an accretion disk that functions as a powerful source of radiation. This disk is fed efficiently by the surrounding material including dust and gas, and emits radiation across the electromagnetic spectrum with a higher luminosity than the rest of the galaxy, and can release relativistic jets of outflowing material (Rees, 1984; Padovani et al., 2017; Hickox & Alexander, 2018; Chan et al., 2019).

Feedback from sources within the galaxy also helps to shape the stellar population, impacting the star formation rates within giant gaseous clouds. The mechanisms by which feedback occurs include supernovae, active galactic nuclei, and stellar winds, all of which expel energy and mass into the local environment (Mo et al., 2010). Feedback from AGN and supernovae in particular are important to star formation in galaxy formation, with positive and negative feedback supporting and preventing star formation respectively (Morganti, 2017). AGNs expel energy as a result of the accretion of gas and dust onto the disk orbiting the MBH, through which a massive amount of radiation is generated; with some AGN producing large scale outflows up to order $\sim$ Mpc in the form of high energy jets when the central MBH has spin or the disk has a magnetic flux (Blandford et al., 2019). Feedback is generally separated into two modes, the 'Radiative' and 'Kinetic' mode. The

Radiative mode occurs for cold gas where the MBH accretion is approaching the Eddington limit in which energy emission takes place via the release of photons, versus the Kinetic mode with a lower accretion rate and luminosity for galaxies with hot gas surrounding the centre, where relativistic particles are expelled (Fabian, 2012; Harrison et al., 2018).

Through this early regulation of star formation, AGN have a large scale impact on the evolution of galaxies, ending once the 'active' phase is over after accretion is done in quiescent galaxies, with observations placing the peak of quasar luminosity at $z \sim 2\,\mathrm{Gyr}$ (Hopkins et al., 2007). Stellar feedback also serves to hinder star formation in molecular clouds (Krumholz & Tan, 2007; Maiolino et al., 2017; Olivier et al., 2021).

1.5 Formation and Coalescence of Massive Black Hole Binaries

The host galaxies of central MBHs undergo mergers in the hierarchical formation model, creating a remnant galaxy containing the central MBHs of the previous two hosts (Merritt, 2013). Within cosmological simulations, major galactic mergers (often set by a mass ratio of $> 1/4$) have been shown to take place across the galaxy lifetime and can experience merger rates of $\sim 0.4\,\mathrm{Gyr}^{-1}$ over $12\,\mathrm{Gyr}$ for large dark matter halo masses ($> 10^{14}\,\mathrm{M}_\odot$), increasing as z increases (Fakhouri et al., 2010).

These MBHs travel to the center of the remnant galaxy and form a binary before coalescing into a single central MBH. As they merge, they release potentially detectable GWs, observations of which will provide information on the MBH population of the Universe (as discussed in Sec. 1.6.2). The processes by which this inspiral occurs are divided into three major phases of evolution - dynamical friction (e.g. Antonini & Merritt, 2012), stellar scattering (e.g. Sesana et al., 2008a), and the final inspiral releasing GWs bringing the MBHs to coalescence.

1.5.1 Dynamical Friction

The evolution of MBH binaries proceeds over three major phases, beginning with the dynamical friction phase during which the MBHs sink to the centre of the merger remnant. During a galaxy merger, the MBHs previously hosted at the centres interact with the surrounding stellar background of the new galaxy, decelerating and hence spiralling in closer to the centre as the orbit decays and the MBH separation decreases (Kelley et al., 2017). Considering a particle in a field of background stars, Chandrasekhar (1943) formulated that the particle would experience a reduced acceleration as it travelled owing to the combined effect of the background stars. Later works on dynamical friction consider other cases, such as where the object being acted upon is significantly heavier than the individual particles that compose the background distribution (i.e. in the case of a black hole $M_{bh} \gg m_\star$) (e.g. Begelman et al., 1980). As the MBH under consideration travels through the field of background particles, the wake created in its path is composed of an overdensity of particles which exert a drag force on the MBH. Gas may also contribute to the gravitational wake, although in the case of massive ellipticals the lack of a gaseous component renders this effect negligible (Ostriker, 1999; Li et al., 2020). Dynamical friction circularises the orbits of massive bodies for values of $\gamma > 1.5$, and increases the eccentricity for $\gamma < 1.5$ (Antonini & Merritt, 2012).

The dynamical friction timescale for a black hole travelling to the centre of a galaxy, considering the secondary MBH, may be calculated from the change in angular momentum of the MBH as a result of the frictional force. One such derivation is given by Merritt

(2013), in which the stellar density profile of the galaxy is taken as $\rho(r) = \rho_0(r/r_s)^{-\gamma}$ and the two galaxies are approximated as isothermal spheres, with $\gamma = 2$ for a single isothermal sphere. The derivation also makes the assumptions that the secondary MBH inspirals on a circular orbit, $\rho_0 = r_{1/2}$, the half-mass radius, and that the initial orbit radius of the infalling MBH is much greater than the distance from the centre of the larger galaxy at which the smaller galaxy has lost most of its constituent stars. This gives a dynamical friction timescale of

$$T_{\rm df} \simeq 1.3 \times 10^8 \left(\frac{\sigma}{200\,{\rm km\,s^{-1}}}\right)^2 \left(\frac{\sigma_2}{100\,{\rm km\,s^{-1}}}\right)^{-3} \left(\frac{2}{\ln\Lambda}\right) \left(\frac{r_i}{1\,{\rm kpc}}\right) {\rm yr} \tag{1.10}$$

where σ_2 is the constant velocity dispersion of the secondary galaxy stars, and r_i is the initial orbital radius of the MBH.

For an isotropic system, the drag on the MBH is given by (Binney & Tremaine, 2008)

$$\dot{\mathbf{V}} = -16\pi^2 G^2 M_{bh} m \ln\Lambda \left[\int_0^V {\rm d}v\ v^2 f(v)\right] \frac{\mathbf{V}}{V^3} \tag{1.11}$$

where V is the relative velocity of the MBH to the galaxy centre, and m and v are the field star mass and velocity respectively. The velocity of the surrounding stars plays a role in their contribution to the dynamical friction force on the MBH - considering a local star travelling at a velocity higher than the MBH, with $v > V$ for Eqn. 1.11 this implies the star does not contribute to the drag on the MBH (Chandrasekhar, 1943; Dosopoulou & Antonini, 2017). This is not completely accurate, with N-body simulations showing that fast stars contribute less and so frictional force decays but does not fall to 0, matched by an additional term to the dynamical friction force (Antonini & Merritt, 2012).

Dynamical friction continues to sink the MBHs to a distance of the order $\sim R_{\rm infl}$ (Eqn. 1.8) of the primary MBH. As a result of the effect of dynamical friction on the black holes moving against the stellar background causing the MBHs to sink to the centre of the remnant galaxy, they pair as a bound binary at a distance of a_f from one another, at which point dynamical friction loses efficacy. At a_f, the enclosed stellar mass is equal to twice the mass of the secondary MBH, as

$$M_*(a_f) \simeq 2M_{bh,2}\ . \tag{1.12}$$

Here three-body interactions take over, and the influence of dynamical friction wanes as the binary moves into reaching thermal equilibrium with the surrounding stars (Antonini & Merritt, 2012; Gualandris & Merritt, 2012a; Kelley et al., 2017).

1.5.2 Stellar scattering

Once the MBHs have formed a bound binary at scales of order a_f, stellar scattering takes over as the dominant hardening process. This phase of binary evolution proceeds faster than the dynamical friction phase as the MBHs experience three-body interactions with local stars and lose energy, hardening the binary (Sesana et al., 2008a).

As the MBHs orbit one another, they incur strong three-body interactions with individual stars within the losscone, driving a rapid gravitational slingshot phase (Quinlan, 1996; Sesana et al., 2008a). The losscone is the region in phase space that hosts the stars on orbits that may interact with the MBHs, typically within a few $\sim a$, the semi-major axis of the binary (Milosavljević & Merritt, 2001). The specific mechanical energy, eccentricity and semi-major axis of the binary orbit are given by

$$E = 0.5v^2 - \frac{GM_{bh}}{r} \tag{1.13}$$

$$a = -0.5\frac{M_{bh}}{E} \tag{1.14}$$

$$e = \left(1 + \frac{2Ej^2}{G^2M_{bh}^2}\right)^{0.5} \tag{1.15}$$

where v and r is the relative velocity and separation between the MBHs respectively, j is the specific angular momentum defined as $j = |\mathbf{r} \times \mathbf{v}|$, and M_{bh} is the total MBH mass. As the binary continues to shrink via interactions with stars in the surrounding losscone, the gravitational slingshot mechanism in which stars in the losscone of the binary are accelerated by the MBHs removes energy and angular momentum from the binary with the ejection of these stars. This causes the two MBHs to spiral closer together (Begelman et al., 1980; Merritt, 2013). The hardening rate of the binary shrinks over time as the binary ejects stars within the losscone and the orbit becomes smaller, and evolves as (Gualandris et al., 2022)

$$\left.\frac{da}{dt}\right|_{*} = -s(t)a^2 \tag{1.16}$$

where the time-dependant hardening rate $s(t)$ is defined as

$$s(t) = \frac{d}{dt}\left(\frac{1}{a}\right) \ . \tag{1.17}$$

The dimensionless eccentricity growth rate K is defined as (Quinlan, 1996)

$$K = \frac{de}{d\ln(1/a)} \ , \tag{1.18}$$

and the contribution to the eccentricity evolution from three-body stellar interactions is

$$\left.\frac{de}{dt}\right|_{*} = s(t)Ka \ . \tag{1.19}$$

Following these strong encounters, stars are ejected with velocities comparable to the binary's orbital velocity and a core is carved in the stellar distribution (e.g. Merritt & Milosavljević, 2005; Gualandris & Merritt, 2012a). As described in Sec. 1.3.1, stellar cores have been observed in elliptical galaxies of magnitudes $M_B \lesssim -21$ with significant central flattened density profiles (Bertola & Capaccioli, 1975; Faber et al., 1997; Graham, 2019). Large bright ellipticals exhibit such cores, with core scouring by MBH binaries the leading explanation for the depleted central stellar density (Quinlan, 1996; Thomas et al., 2014; Nasim et al., 2021).

Once all stars initially on losscone orbits have been ejected and the binary is formally bound and hard at roughly $\sim$ parsec scale separations for a typical MBH of mass 10^8 $\mathrm{M}_{\odot}$, further hardening relies on overcoming the lack of stars available for three-body interactions. This is known as the final parsec problem (Vasiliev et al., 2014, 2015).

Final parsec problem

At $\sim$ pc MBH separations, once all stars within the losscone have been ejected the continued hardening of the binary relies on the scattering of stars into the losscone from larger distances, a process known as losscone refilling. Steady state losscone theory makes the distinction between the 'empty-losscone regime' and the 'full-losscone regime'. In the former, the stars in the losscone have a change in angular momentum over one orbit less than the angular momentum of the losscone boundary, and in the latter the losscone never fully depletes through efficient refilling, with the rate of stars moving into the losscone proportional to the hardening rate $s(t)$ (Merritt, 2013).

Stalling of the binary occurs in simulations where the only mechanism for losscone repopulation is 2-body gravitational encounters within spherical galaxies. The collisional relaxation timescales of stars extends beyond a Hubble time for the majority of galaxies, and without another method of repopulating the losscone the binary cannot harden further (Milosavljević & Merritt, 2003a,b; Vasiliev et al., 2014). Investigation into the repopulation rate requires a sufficiently high particle number, as a stellar mass resolution below $N \simeq 10^6$ can artificially induce relaxation, refilling the losscone spuriously (Merritt et al., 2007; Bortolas et al., 2016).

Different models have been explored to find a solution. Idealised spherical galaxy model do not accurately reflect the actual potential of galaxies post-merger, when MBH binaries form. In non-spherical galaxies with axisymmetric and triaxial potentials, stars may travel along close to centrophilic and centrophilic orbits respectively as the angular momentum is not conserved. The process by which orbits are affected by torques in non-spherical potentials and become irregular is called angular momentum diffusion (Yu, 2002; Vasiliev & Merritt, 2013; Gualandris et al., 2017). Further investigations with triaxial models have shown that collisionless losscone refilling can overcome the final parsec problem with efficient repopulation of the stellar orbits through angular momentum diffusion. This mechanism which has been proven efficient in non-spherical models. Merger remnants have some degree of triaxiality, and so collisionless diffusion can continue binary hardening past parsec scales (Vasiliev et al., 2015; Gualandris et al., 2017; Frigo et al., 2021).

Hard binary formation

At a separation of a_h, the MBHs form a hard binary (which typically occurs at roughly pc scale distances for $M_{\rm bh} \sim 10^8\,{\rm M}_\odot$) (Quinlan, 1996; Milosavljević & Merritt, 2001). a_h has several possible definitions, with one such description being where the relative velocity of the binary surpasses the velocity dispersion of local stars (Merritt, 2013)

$$a_h = \frac{G\mu}{4\sigma^2} \tag{1.20}$$

where $\mu = M_1 M_2/(M_1 + M_2)$ is the reduced mass of the two MBHs. For an equal mass binary, $a_h = \frac{R_{\rm infl}}{8}$. Beyond a_h, the orbit continues to shrink through efficient ejection of local stars (Gualandris et al., 2017), and the binary evolves according to the hardening rate Eqn. 1.17 (Merritt, 2013). Figure 1.7 shows the binary separations a_f and a_h for two MBH binaries from the end of the dynamical friction phase into the GW phase in Gualandris & Merritt (2012a). Collisionless losscone refilling is then able to drive the MBH binary to separations of the order of milliparsecs or less, where emission of GWs commences (Gualandris et al., 2017).

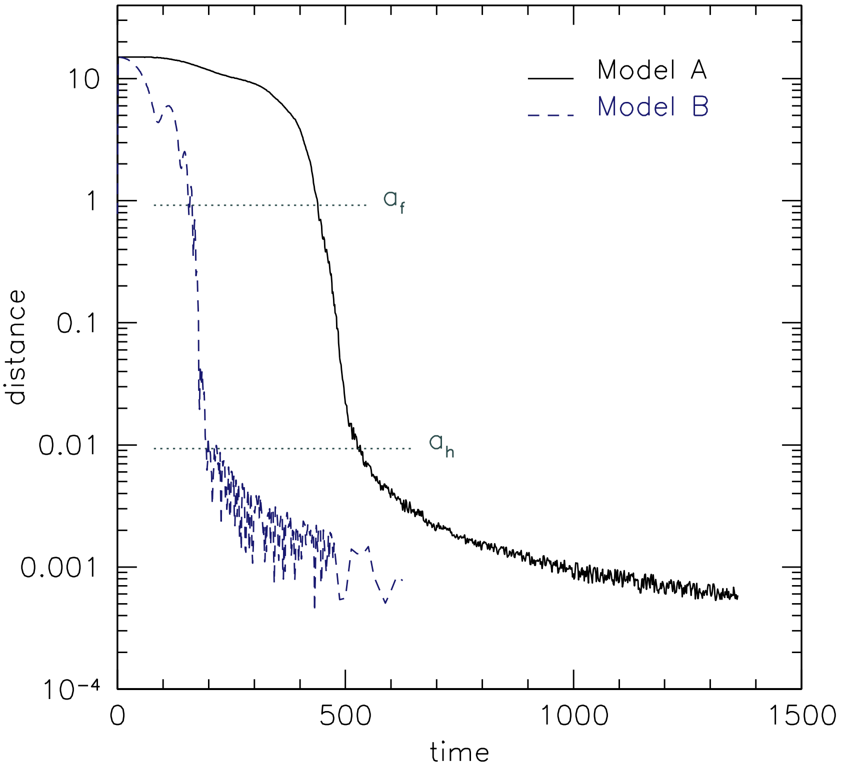

Figure 1.7: Separation of two MBH binaries over time. a_f and a_h are marked with horizontal black dotted lines. Figure from Gualandris & Merritt (2012a).

1.5.3 GWs (Final inspiral)

At the final stage of inspiral, GWs are released by the binary as the MBHs orbit hardens past a separation of $\sim 10^{-3}$ pc. The GWs carry energy away from the binary, bringing them to a rapid coalescence (Begelman et al., 1980).

At this stage the post-Newtonian (PN) formalism may be employed to obtain approximate solutions to the Einstein field equations in the weak field regime. GWs are modelled with the correction of order 2.5PN (Blanchet, 2014). Peters (1964) provides approximate analytic solutions to the field equations for the evolution of an MBH binary orbit, with the semi-major axis a and ellipticity e decaying as

$$\left\langle \frac{da}{dt} \right\rangle_{GW} = -\frac{64}{5}\frac{G^3 M_1 M_2 M}{c^5 a^3 (1-e^2)^{7/2}}\left(1 + \frac{73}{24}e^2 + \frac{37}{96}e^4\right) \tag{1.21}$$

$$\left\langle \frac{de}{dt} \right\rangle_{GW} = -\frac{304}{15} e \frac{G^3 M_1 M_2 M}{c^5 a^4 (1-e^2)^{5/2}}\left(1 + \frac{121}{304}e^2\right) \tag{1.22}$$

for an average over one orbital period of the binary, where $M = M_1 + M_2$ is the total MBH mass. The onset of the GW-dominated phase of evolution depends strongly on the eccentricity, which hence has a significant influence on the coalescence timescale of MBH binaries (Khan et al., 2018).

The GWs released by the inspiral of the most massive MBH binaries are potentially detectable as the low-frequency GWB, as described in Section 1.6, and within the frequency range for these GWs given in Figure 1.8. Considering detectable individual sources, the chirp is a signal where the frequency changes with time. The chirp mass of the source system can be determined from measurements of the chirp time of GW signals, allowing the distance to the source to be determined in combination with the signal strain h (Sesana et al., 2009; Merritt, 2013). The chirp mass of the binary is defined as

$$\mathcal{M} = \frac{(M_1 M_2)^{3/5}}{M^{1/5}} \, . \tag{1.23}$$

Ringdown is the denouement of the binary, taking place once the MBHs have coalesced (Scheel et al., 2009). The remnant mass and spin can be determined from measurements of the GWs emitted in the ringdown phase (Berti et al., 2018; Amaro-Seoane et al., 2022).

1.6 Gravitational Wave Astronomy

The detection of Gravitational Waves (GWs) from two merging black holes by the LIGO scientific collaboration (Abbott et al., 2016a) has opened a new window on the Universe, providing new insights into the astrophysical sources of measurable GWs. With both direct proof of the existence of black holes and the confirmation of the prediction that binaries of black holes coalesce, this first detection commenced the GW era with 90 events to date having since been observed, including both black hole and neutron star mergers (The LIGO Scientific Collaboration et al., 2021). These detections provide direct measurements of the mass alongside information on their spins, and have given new impulse to the ongoing efforts in detecting GWs from binaries of supermassive black holes.

GWs are disruptions in the space-time fabric of the Universe, which cause the tidal compression of space-time as they propagate (Dirkes, 2018). Unlike electromagnetic radiation, GWs travel essentially unobstructed across space and enable investigation into the early evolution of MBHs and their host galaxies at high redshifts (Colpi et al., 2019). The prediction of gravitational radiation arose as a consequence of Einstein's theory of general relativity, as published in Einstein (1915), with solutions to his equations of general relativity predicting tidal disturbances in the fabric of space-time as a result of the acceleration of massive bodies (Einstein, 1916, 1918). Black hole binaries emit GWs at their final stage of coalescence, and binaries of MBHs represent the loudest sources of GWs in the Universe (Peters, 1964).

The range of possible astrophysical sources of GWs and their associated detection methods is shown in Figure 1.8. Mergers of the most massive MBHs ($M > 10^7\,\mathrm{M}_\odot$) are detectable by the Pulsar Timing Array (PTA) at the lowest frequencies in the spectrum of $10^{-9} - 10^{-6}$ Hz (Desvignes et al., 2016a; Reardon et al., 2016a; Perera et al., 2019), while MBHs in the mass range $10^4 - 10^7\,\mathrm{M}_\odot$ will be the main target of the Laser Space Interferometer (LISA) in the frequency range $(10^{-4} - 1)$ Hz (Amaro-Seoane et al., 2017; Barack et al., 2019). A greater detector arm length is required to observe GWs emitted by larger sources such as MBH binaries, as the amplitude of a GW is proportional to the mass and velocity of the source (see Sec. 1.6.1). Detection of GWs from black hole binaries will provide accurate estimates of masses, spins and orbital parameters up to redshifts of $z = 2$ with PTA, and beyond redshifts of 20 for some BH masses with LISA (Colpi et al., 2019).

1.6.1 Gravitational Wave Emission

The generation of GWs were predicted as a consequence of Einstein's theory of general relativity, emitted by the acceleration of objects as they radiate oscillations in space-time. GWs are radiated under the condition that the system is not spherically or rotationally

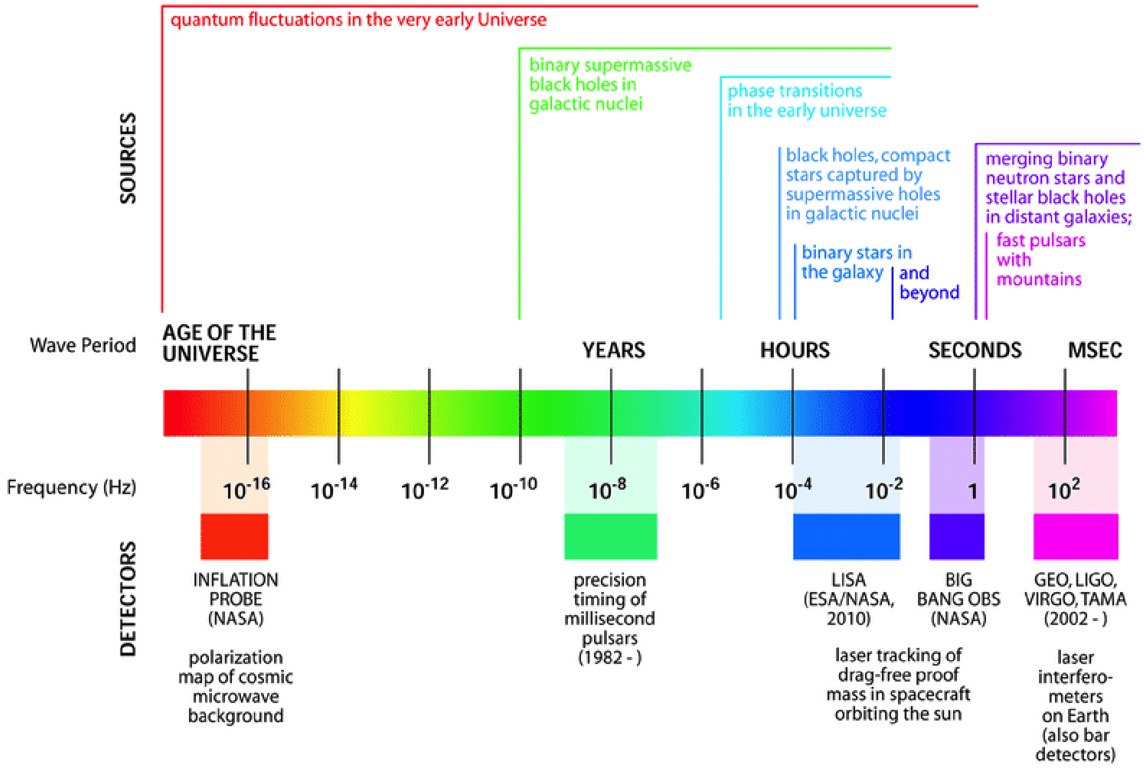

Figure 1.8: The gravitational wave spectrum shown across the age of the Universe, with corresponding GW sources and detection instruments. Figure adapted from (Romano & Cornish, 2017).

symmetric, and the source bodies need to be sufficiently massive in order to emit detectable GWs. The oscillations distort material they pass through, tidally compressing and stretching matter as the wave travels (Eardley et al., 1973). This spatial deformation is described by the dimensionless strain, a measure of the change in the particle position with reference to a chosen length. They propagate through space-time at c (the speed of light) (Creighton & Anderson, 2011), with wavelengths λ of orders that are typically of the size or larger than their sources (for example the radius of the system, in the case of a GW emitting binary) (Amaro-Seoane, 2013; eLISA Consortium, 2013; Dirkes, 2018).

The Einstein field equations describe how space-time is affected by matter, dependent on the momentum, energy, and stress of local mass. The quadrupole formula solution gives the metric perturbation for a GW, concerning a weak gravitational field far from the source

$$\mathbf{h}^{ij}(ct, \mathbf{x}) = -\frac{2G}{c^4 r}\left[\frac{d^2 I^{ij}(ct')}{dt'^2}\right]_r \tag{1.24}$$

for a reduced time $t_r = t - r/c$, with the quadrupole-moment tensor I^{ij} of the source energy density

$$I^{ij}(ct) = \int T^{00}(ct, \mathbf{y}) y^i y^j d\mathbf{y} \tag{1.25}$$

where T^{00} is the relativistic mass density. The emitted GWs carry energy away from their source with a wavelength that is dependent on the size of the system (Ryder, 2009). Using Eqn. 1.24, the GW luminosity can be first derived in terms of I^{ij}, from which the approximation $\partial^3 I^{ij}/\partial t^3 \sim MR^3/T^3$, with T the period for an object to travel across the source, leads to an approximation for the GW luminosity of

$$L_{GW} \sim \frac{G^4}{c^5}\left(\frac{M}{R}\right)^5 \sim \frac{c^5}{G}\left(\frac{r_{Sch}}{R}\right)^2\left(\frac{v}{c}\right)^6 \tag{1.26}$$

where r_{Sch} is the Schwarzschild radius, defined as the radius of the event horizon of a Schwarzschild black hole at $r_{Sch} = 2GM/c^2$. Eqn. 1.26 shows the highest L_{GW} is achieved with a very dense, relativistic source. The amplitude of GW oscillations can similarly be estimated as

$$h \sim \frac{G}{c^4}\frac{\epsilon E_k}{r} \tag{1.27}$$

for the dimensionless strain h, where ϵE_k is the kinetic energy of the source that contributes to the GWs (with $0 \leq \epsilon \leq 1$), at a distance r (Camp & Cornish, 2004; Moore et al., 2015; Abbott et al., 2017). For a binary system, such as in the case of an MBH binary, the emitted GWs shrink the binary separation as they carry away energy (Begelman et al., 1980).

1.6.2 Gravitational Wave Detections - LISA and PTA

Sufficiently high frequency GWs from large sources cause measurable changes in the length of objects as they compress and lengthen space-time - in this way, their passage can be detected. At the low frequency end of the GW spectrum shown in Figure 1.8, GW emissions from MBH binaries are detectable as a superimposed stochastic gravitational wave background, while higher frequency detectors can observe emissions from stellar mass black hole binaries (e.g. Perera et al., 2019). The physical detection of GWs can be achieved as travelling GWs deform the objects as they travel through space as a time dependent quadrupolar strain h given by Eqn. 1.27, with GW oscillations acting perpendicular to the direction of travel (Bailes et al., 2021).

The first GW detectors, called resonant mass detectors, utilised this variation to attempt measure the vibrations of an isolated metal bar induced by passing GWs, but only have the sensitivity required to observe the strongest GWs, and no detections have been achieved to date (Creighton & Anderson, 2011; Aggarwal et al., 2021). Further efforts have since employed the more sensitive laser interferometers which measure the GW-induced deformation via changes in light interference patterns, and pulsar timing arrays (PTA) which measure the difference in arrival times of radio pulses rather than light. The frequency spectrum the GW detectors work across spans a wide range of orders of magnitude, as shown in Figure 1.8, and as such the detectors are designed to be sensitive to specific ranges. Both utilising interferometry, the ground-based LIGO has detected GWs at the high-frequency end of the spectrum (Abbott et al., 2016a; The LIGO Scientific Collaboration et al., 2021), and the upcoming space-based LISA will probe the lower frequency range $(10^{-4} - 1)$ Hz, enabled by avoiding ground-based seismic interference (eLISA Consortium, 2013; Bailes et al., 2021). PTA detectors are sensitive at lower frequency ranges of $(10^{-9} - 10^{-6})$ Hz, where MBH binaries emit GWs.

LISA

LISA (Laser Interferometer Space Antenna) is a space-based GW observatory, currently aimed to launch in 2037. Working in the frequency range of $(10^{-4} - 1)$ Hz, it will have the ability to detect black hole masses in the range of $(10^4 - 10^7)\,\mathrm{M}_\odot$, precise measurements of stellar mass black hole binaries that can be followed with electromagnetic observations, and extreme mass ratio inspirals (Enoki et al., 2004; Sesana, 2016; Amaro-Seoane et al., 2017; Barack et al., 2019; Amaro-Seoane et al., 2022).

The detector is planned to operate using an adapted Michelson interferometer to measure the disturbance that will result from a passing GW deformation. LISA will consist of three spacecrafts in a triangular configuration with a 2.5 million km arm length (Cornish & Robson, 2017). These separations remain constant unless affected by the passage of GWs. The Michelson-like interferometer method has been adapted for the LISA spacecraft, which uses signal frequency changes from the spacecraft to create the time-delay interferometry technique, measuring the amplitude of the passing GWs from the phase shifts of the lasers caused by the GW (Creighton & Anderson, 2011; Bailes et al., 2021). The LISA Pathfinder mission launched in 2015 successfully tested the LISA configuration with a short arm, returning the first results in 2016. The Pathfinder mission could not detect GWs owing to the shorter arm length, but the performance demonstrated the precision of the proposed methodology (Armano et al., 2016, 2018; Wanner, 2019). LISA will travel on a heliocentric orbit, for a proposed mission length of 4 years. Following on from the LIGO observations of signals from black holes, the LISA GW observations will bring new sensitivity to the GW spectrum (Bailes et al., 2021; Barack et al., 2019).

Pulsar Timing Arrays

Sensitive to the lower frequency end of the GW spectrum, Pulsar Timing Arrays (PTAs) can detect GWs from the change they induce in the electromagnetic radiation emitted by pulsars. PTAs utilise a set of millisecond pulsars, which can serve as stable clocks owing to the regularity of their pulses. The time of arrivals (TOAs) of the signals can then be compared across the pulsars to search for correlated differences, which could indicate a disturbance in the emissions caused by passing GWs. As shown in Figure 1.9, the emitted radio pulses are detected by telescopes on Earth, and the timing residuals are corrected for systematic delays. These delays are composed of temporally uncorrelated white noise, which includes induced by radiometer noise and the pulse profile shape variations generated by the signal emission; and the correlated red noise, which includes the intrinsic spin noise from the pulsar (Shannon et al., 2014; Goncharov et al., 2021). The mean pulse profiles across the observation timescale are obtained from the dataset, and the TOAs are compared to look for spatially correlated red noise that marks the passage of GWs (Arzoumanian et al., 2020; Bailes et al., 2021).

With the regularity of the millisecond pulsar signal TOAs, PTAs are able to detect GWs in the frequency range of $(10^{-9} - 10^{-6})$ Hz, lower than other such detectors, and so enabling measurement of the GW remnants of mergers of the most massive MBHs ($M > 10^7\,\mathrm{M}_\odot$) (Desvignes et al., 2016b; Reardon et al., 2016b; Perera et al., 2019). They are expected to measure the amplitude of the stochastic gravitational wave background (GWB) produced by an unresolved population of close binary MBHs (Kelley et al., 2017; Arzoumanian et al., 2018; Christensen, 2019), and potentially bright individual sources in the future (Lee et al., 2011; Rosado et al., 2015; Kelley et al., 2018). Following PTA detection of the GWB, the amplitude in the nano-Hz regime of the detection can then be determined from subsequent analysis of isolated noise from the results, providing information on the large-scale structure of the Universe, the occupation fraction of MBHs in galaxies, the merger rate of galaxies, scaling relations between MBHs and host galaxies and the efficiency of pairing and merging of MBH binaries (Sesana, 2013; Burke-Spolaor et al., 2019; Amaro-Seoane et al., 2022).

Currently active PTAs include the International Pulsar Timing Array (IPTA) group, with two data releases so far (Verbiest et al., 2016; Perera et al., 2019), with members

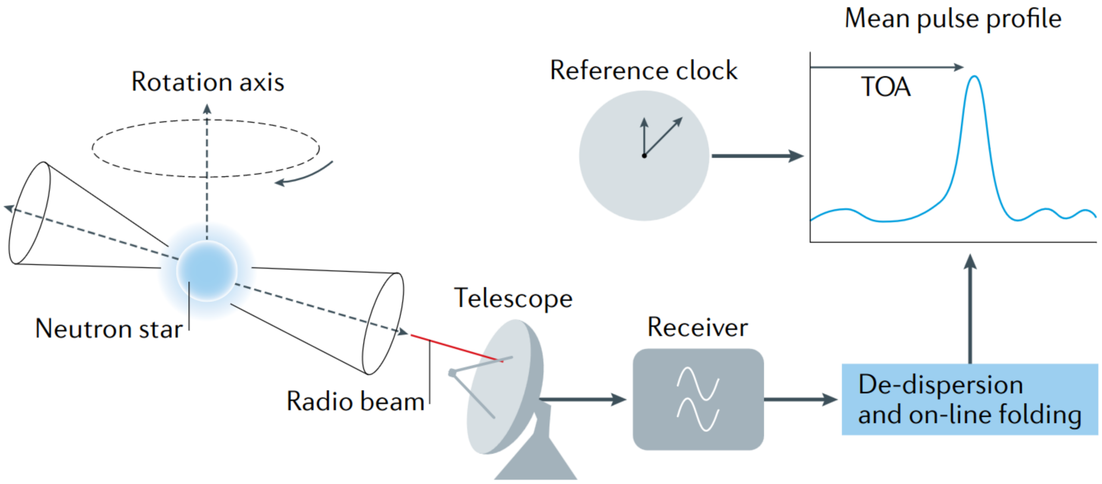

Figure 1.9: The radio signals emitted by a set of pulsars are received on Earth, and corrected for systematic delays (de-dispersion), before the TOAs are compared to look for spatially correlated differences between the set. Figure from Bailes et al. (2021).

NANOGrav, EPTA, PPTA, and InPTA. Constraining the GWB can be achieved before the detection itself takes place; limits have already been placed on the signal, significantly from PPTA placing an amplitude ceiling of $< 1.0 \times 10^{-15}$ (Shannon et al., 2015; Taylor et al., 2016). A potential GWB signal with a median amplitude of 1.9×10^{-15} was subsequently detected within the second 12.5−year data release from NANOGrav (the North American Nanohertz Observatory for Gravitational Waves), although there was not strong enough evidence to confirm the origin of the noise from GWs, which would require quadrupolar spatial correlations (Arzoumanian et al., 2020; Chen et al., 2021). Subsequent examination of this signal by Middleton et al. (2021) gave results in accordance with GWs produced by coalescing MBH binaries. The signal conflicts with the prior upper limits placed on the GWB of $A_{GWB} < 1.45 \times 10^{-15}$ from earlier data releases (Arzoumanian et al., 2018), explained by Arzoumanian et al. (2020) as these constraints were calculated using an analysis that may have underestimated the maximum amplitude.

The detection of a low-frequency signal by PTA with strong evidence for interpretation as a stochastic GWB was recently reported and independently corroborated across the EPTA/InPTA, NANOGrav, PPTA, and CPTA collaborations (Agazie et al., 2023b,a; Afzal et al., 2023; Antoniadis et al., 2023c,b; Reardon et al., 2023; Xu et al., 2023). This signal is powerful evidence for a detection of GWB origin, showing strong evidence for quadrupolar spatial correlations following the Hellings–Downs (HD) curve (Hellings & Downs, 1983; Agazie et al., 2023b). The NANOGrav results showing evidence for HD correlations are shown in Figure 1.10 (Agazie et al., 2023b). It is not yet considered a confirmed GW signal however, as the significance does not quite reach firm detection status. For this, a 5σ significance is required, but the results reported only reach $\sim 2 - 4\sigma$. The signal is consistent with a population of merging MBH binaries, with implications for the population including the coalescence timescales and the MBH-bulge relation if confirmed (Antoniadis et al., 2023a). There is also the possibility the signal could originate from another source such as primordial GWs produced by cosmic inflation. As more information is gathered over time the signal will grow more distinctive, and with confirmation of its origin in merging MBHs it will be possible to place more constraints on the MBH population (Agazie et al., 2023b; Afzal et al., 2023; Antoniadis et al., 2023b,a; Xu et al.,

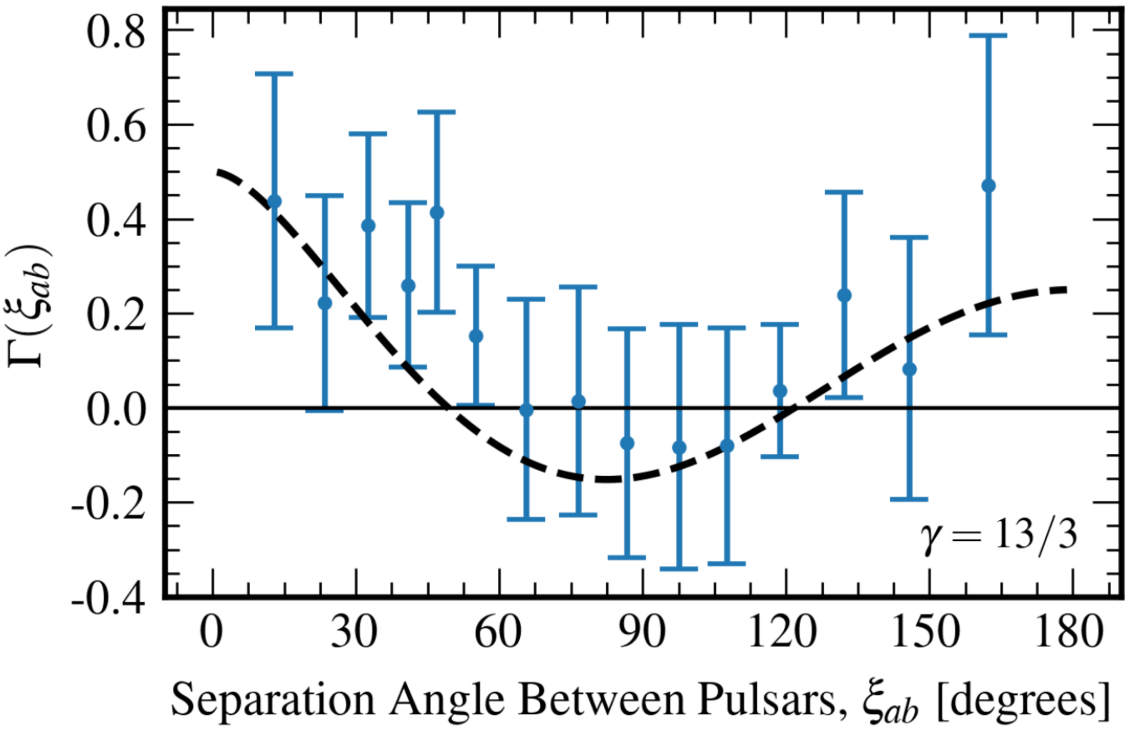

Figure 1.10: Inter-pulsar correlations determined from timing residuals as a function of the angular separation between pulsars (blue points), with the expected Hellings-Downs curve (black dashed line) showing the expected function for a GWB detection. Figure from Agazie et al. (2023b).

2023). PTAs may also be able to detect individual massive MBH binaries distinguished from the GWB as continuous monochromatic (single frequency) sources in the future, but this will require a longer detection timespan potentially with a joint analysis between all the datasets (Kelley et al., 2018; Arzoumanian et al., 2020; Agazie et al., 2023b). The signal portends the dawn of an exciting new frontier in gravitational wave astronomy.

With the recently confirmed evidence of a low-frequency excess signal by PTAs (e.g. Taylor, 2019; Agazie et al., 2023b) and LISA in the final preparations phase before launch, it has become crucial to estimate detection rates for both instruments. Current estimates come from either semi-analytical models or cosmological simulations, and are affected by considerable uncertainties.

1.7 Modelling

In MBH binary modelling, it is necessary to be able to reconcile the large scales required for galaxy mergers with the high resolution needed at the small scales for accurate MBH merger dynamics. This leads to challenges for any simulation attempting to investigate MBH mergers and their associated timescales and expected observations. Current estimates of MBH merger statistics and hence the predicted GW event rates come mainly from semi-analytical models and cosmological simulations, and are affected by significant uncertainties (Rantala et al., 2017; Gualandris et al., 2017; Nasim et al., 2020).

Semi-analytic models can produce merger statistics by tracing the evolution of galaxies and their central MBHs, producing predictions that match observational constraints of the galaxy properties, and following the MBH binary separation with simplified prescriptions on the pairing and evolution (e.g. Somerville et al., 2008; Barausse et al., 2020). Semi-analytic prescriptions can also follow the MBH binary from three-body interactions and GWs phase through to coalescence, extending N-body simulation evolution (Sesana et al., 2009). Cosmological hydrodynamical and N-body simulations study large-scale evolution of baryonic and dark matter, and model galaxies across cosmic time (e.g. Vogelsberger et al., 2020). The MBH binary is followed to the resolution limit of the simulation, for example of the order 1 kpc for Illustris and 300 pc for IllustrisTNG50-1 (Nelson et al., 2019). Predictions of GW signals for detectors have been obtained using the data released thus far, using the properties of merging black hole binaries in cosmological simulations implemented via sub-grid physics, or by using the simulation results as input to semi-analytical modelling. Semi-analytical modelling can also utilise Press-Schechter formalism to determine the initial input (Press & Schechter, 1974; Amaro-Seoane et al., 2022).

1.7.1 Semi-Analytic Models

Semi-analytical models have been used to follow the evolution of MBHs and their host galaxies, including dark matter (DM) halos, within the context of the ΛCDM framework. (Somerville et al., 2008; Volonteri & Natarajan, 2009; Sesana et al., 2014; Lacey et al., 2016). Using a DM merger tree as a basis to link galaxy histories, the component structures are evolved using semi-analytic prescriptions. Recent models have included prescriptions for MBH growth via mergers and accretion, and supernovae feedback, a process that has been shown to regulate the galaxy star formation and MBH growth as described in Sec. 1.3.1 and 1.4.1. These prescriptions have been shown to reproduce observed properties such as morphology, colour, star formation rates and subsequent mass growth, and luminosity functions at low redshift (Driver et al., 2018; Ricarte & Natarajan, 2018; Barausse et al., 2020).

Semi-analytic models are computationally inexpensive to run in comparison to N-body simulations, and with the resulting reduced runtime, they can be used to explore a wide parameter space (Driver et al., 2018; Lagos et al., 2018; Izquierdo-Villalba et al., 2022b). However, they rely on simplified assumptions and prescriptions regarding the pairing and evolution of MBH binaries, with key regimes such as binary hardening due to three-body encounters with stars modelled based on the results of isolated three-body scattering experiments (Izquierdo-Villalba et al., 2022a). Both low and high-mass black hole seeds must be considered for a complete picture of the MBH population at high redshifts, as MBH seed masses are currently largely unconstrained (see Sec. 1.2.1) (Volonteri, 2010; Amaro-Seoane et al., 2022).

Recent semi-analytic models estimating GWB signal predictions from MBH binaries include L-Galaxies (Izquierdo-Villalba et al., 2022a), and the SHARK model (Lagos et al., 2018; Curyło & Bulik, 2022). The event rate predictions give GWB amplitudes in the PTA frequency range of $\sim 1.2 \times 10^{-15}$ (Izquierdo-Villalba et al., 2022a), and $1.4 \times 10^{-16} - 1.1 \times 10^{-15}$ from the SHARK model (Curyło & Bulik, 2022). These predictions lie below the red signal determined from the Arzoumanian et al. (2020) results (see Sec. 1.6.2); Izquierdo-Villalba et al. (2022a) also attempt to match these constraints by employing a boosted gas accretion rate onto the MBHs and obtain a GWB prediction of $1.37 \times 10^{-15} - 2.67 \times 10^{-15}$.

1.7.2 Cosmological Models

In contrast to semi-analytic models, cosmological N-body and hydrodynamic simulations model baryonic matter and dark matter within the Universe on large scales from early times. Cosmological models include consistent modelling of galactic merger mass ratios and encounter geometries in subsequent events, with realistic dynamical friction times. Massive halos can be seeded with black holes, which then grow over time due to gas accretion and mergers. Feedback effects can be included which result in gas expulsion and the quenching of both star formation and MBH growth (Di Matteo et al., 2005; Pontzen et al., 2017; Ricarte et al., 2019; Nelson et al., 2019).

Cosmological models trade large volumes for the resolution constraints that accompany a more computationally expensive method (Springel & Hernquist, 2003; Amaro-Seoane et al., 2022). MBHs have been implemented as a key part of galactic evolution, with MBH feedback affecting the star formation rates and the local environment, but are not typically followed with great accuracy owing to resolution constraints (Kormendy & Ho, 2013; Volonteri et al., 2016; Nelson et al., 2019; Ricarte et al., 2019).

The formation of MBH binaries during mergers is followed to the resolution limit, generally set by the choice of the softening length, which is of order $\sim 1\,\mathrm{kpc}$ in the Illustris simulation suite (Genel et al., 2014), and of order $100\,\mathrm{pc}$ in the recent IllustrisTNG-50 (Nelson et al., 2019; Pillepich et al., 2019). In the context of binary evolution, MBHs have only just begun pairing at these distances, and are still unbound to each other. MBH binaries are then assumed to merge promptly, without any modelling of the hardening phase. A trade-off between volume size and resolution is also present, limiting the statistics of MBH binaries that can be obtained from higher resolution simulations.

The resolution limits in cosmological models hamper their ability to follow MBH binary statistics. The volumes of cosmological simulations also affect the statistics - smaller volumes offer better resolution, but provide less opportunity for MBH mergers to occur, whilst the larger volumes that provide a more complete picture of binary statistics do so with poorer resolution. Examples include the Illustris-TNG cosmological simulation suite of 3 volumes from $50\,\mathrm{Mpc}^3$ with a softening of order $100\,\mathrm{pc}$ to $300\,\mathrm{Mpc}^3$ with a softening of order $\sim 5\,\mathrm{kpc}$ (Nelson et al., 2019; Pillepich et al., 2019; Springel et al., 2018). The population of galaxies hosting MBHs and merging within cosmological simulations can inform the input to semi-analytical models (Amaro-Seoane et al., 2022), and have also been used to explore GW detection rates by post-processing the initial MBH results to account for the delays caused by unresolved binary evolution (e.g. Katz et al., 2020).

The recent KETJU code, first presented in Rantala et al. (2017), provides a new method to address the particle resolution issue that affects black hole binary dynamics within cosmological simulations. By implementing a region of high accuracy around a single or binary MBH modelled with algorithmic regularisation, and with the option for inclusion of Post-Newtonian corrections for the GW radiation phase within the regularised region, KETJU extends the GADGET-3 simulation and achieves a better treatment of the MBH binary evolution and coalescence. In its most recent version (Mannerkoski et al., 2023), gravitational wave recoil can also be included. However, due to the large computational cost of algorithmic regularisation, this approach cannot be taken over a full cosmological simulation - rather it can be used to model individual galaxy mergers or short sequences (Mannerkoski et al., 2019, 2022).

The code GRIFFIN brings new development to the challenge of achieving a high numerical resolution whilst maintaining reasonable computational costs. By employing a modified version of the Fast Multipole Method (FMM) for the force computation (see Sec. 2.1.2) that includes a consideration for the ensuing force errors, the resulting operational scaling of the code can achieve a marked improvement (up to $\mathcal{O}(N^{0.87})$ over the $\mathcal{O}(N)$ of FMM codes) for a reasonable set of input parameters. The code shows an improvement in the force errors over standard tree codes as the long force error tails are significantly curbed (Dehnen, 2014). GRIFFIN also includes a high accuracy treatment of MBH-MBH and MBH-star interactions by direct summation with reduced force softening, making it ideal to simulate the black hole binaries formed in galactic mergers. A novel implementation featuring a chain regularised region is under development (Gualandris et al. in prep.), featuring Post-Newtonian corrections and GW recoil at MBH coalescence. A more detailed discussion of GRIFFIN is given in Sec. 2.2, including its usage.

1.8 Thesis Overview

With PTA detectors already operational and expected to make the first 5σ detection of the GWB within the decade (e.g. Taylor, 2019), and the planned LISA mission in its final preparations, it has become crucial to model GW sources at low frequencies and estimate the detection rates for both instruments. These predictions help constrain expected GW event numbers and aid in the interpretation of the data and their astrophysical implications (Amaro-Seoane et al., 2022). Modelling the mergers of MBHs requires a treatment of both the galaxy-scales of their hosts and the smaller scales at central radii to accurately represent the MBH dynamics; this presents a numerical challenge as the limitations enforced by the resulting computational cost restrict the high resolutions necessary.

In this thesis, I present a numerical scheme to aid in accurately predicting MBH merger dynamics and timescales in isolated galaxy merger N-body simulations. To overcome the issue of increasing model resolution whilst still maintaining a bound on the force errors, I investigate the utility of multi-resolution schemes in the context of merging galaxy models and subsequently their MBH dynamics. I utilise the collisionless FMM code GRIFFIN to simulate the evolution of the binary MBH mergers and their host galaxies, and employ a semi-analytic prescription to follow the mergers to coalescence. GRIFFIN achieves reduced force errors combined with a lower computational cost, enabling an accurate examination of the dynamics surrounding MBH binaries in combination with the multi-resolution scheme.

This thesis is organised as follows: In Chapter 2, I describe the numerical methods involved, including the code GRIFFIN. In Chapter 3 I present a series of models with a multi-resolution scheme applied to both isolated and merging galaxies in comparison with reference resolutions, including a discussion of the differences between the models, and in Chapter 4 I use these multi-resolution models to investigate the MBH mergers following on from their host galaxy mergers. In Chapter 5, I examine subsequent mergers with properties extracted from a cosmological merger tree, considering both binary and triple MBH evolution. I present my conclusions to this work in Chapter 6, including a discussion of the potential for future work.

Numerical Modelling

2.1 Simulations

Galaxies are gravitational systems, with the dynamics of their components evolving over time as they interact with one another. For the accurate modelling of a galaxy, computational simulations are required to evaluate the large number of particle interactions involved in such a system. N-body simulations can perform the force calculations for this evolution for a set of N particles at set time intervals across the evolution time for the galaxy. N-body simulations were first performed computationally to investigate the motion of stars in a stellar cluster by von Hoerner (1960) at a maximum total particle number of $N = 16$, and have since developed into a complex and wide-ranging field. Later simulations were able to consider higher particle numbers, and as such the accuracy of the results has improved with the advancement of computational hardware. The scope possible with these simulations has increased as $N = N_0 2^{(y-y_0)/2}$ since their initial employment, as shown with the sample of simulations displayed in Figure 2.1. Other developments included new algorithms that helped to ameliorate the computational cost of larger particle numbers with approximations to the calculations.

In this chapter, I provide an overview of the different N-body simulation techniques used to model galaxies, including the types of force computation, time-steps, and other set-up considerations, and describe the N-body code GRIFFIN that is utilised for the simulations presented in this thesis.

2.1.1 N-body Simulations

Gravity is the dominant force over the long distances examined in astrophysical simulations, with the point masses considered in an N-body model acting on one another within a given system. Modelling an assembly of N particles, N-body simulations follow the evolution of each particles dynamics that occurs as a result of the calculated gravitational interactions over a set time period. These simulations can model galactic systems, wherein the point masses may represent stars, dark matter, or other components (Binney & Tremaine, 2008). The equations for the gravitational potential and force on a particle in a system from Newton's law are formulated as

$$\Phi(\mathbf{r}_i) = -G \sum_{i \neq j}^{i=N} \frac{m_i m_j}{|\mathbf{r}_i - \mathbf{r}_j|} \tag{2.1}$$

$$\mathbf{F}_i = -G \sum_{i \neq j}^{i=N} \frac{m_i m_j (\mathbf{r}_i - \mathbf{r}_j)}{|\mathbf{r}_i - \mathbf{r}_j|^3} \tag{2.2}$$

for a particle i, where r_i is the position of the particle at a given time relative to an inertial frame. Numerical integration is required to solve Eq. 2.2 for $N > 3$, with particle numbers higher than the solved two-body problem and the approximate solutions for the three-body problem.

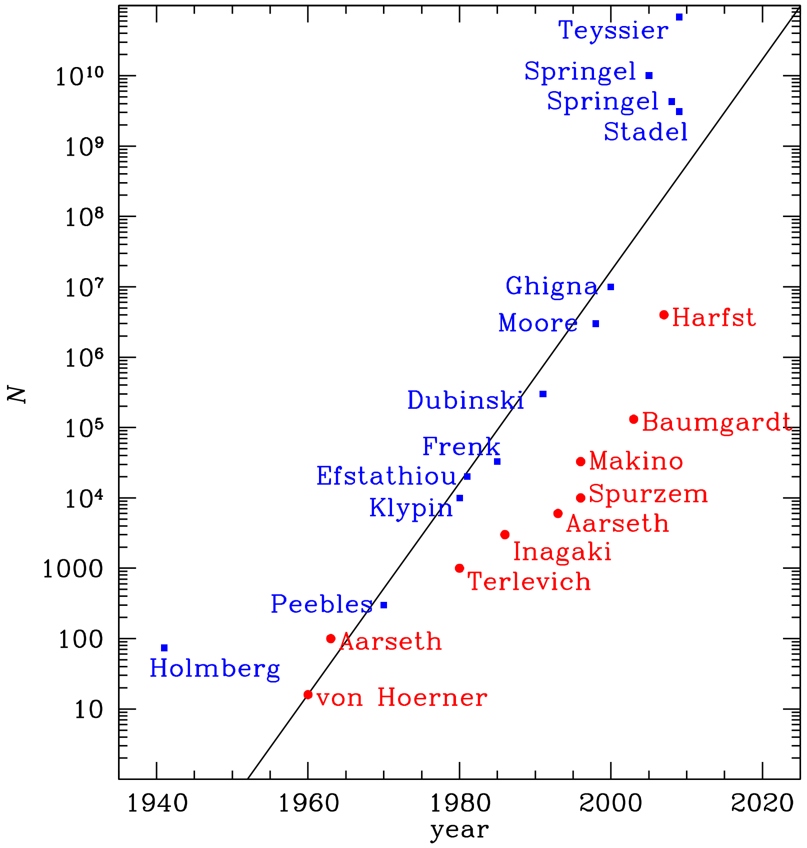

Figure 2.1: The increase in particle numbers for a sample of collisional (red) and collisionless (blue) simulations, shown from the first N-body simulations to 2011. Figure from Dehnen & Read (2011)

Collisionless and Collisional Models

In gravitational simulations, the choice between whether the model should be treated as a collisional or collisionless system lies in the relaxation time, as given by Eq. 1.2. If the system particles are affected by their mutual gravitational interactions within t_{relax}, collisional effects need to be considered by the simulation. Within collisional systems the cumulative effect of small-scale particle interactions induces an equipartition of energy through particle relaxation, with the heavier stars sinking to the centre of the galaxy and the lighter stars moving towards the edges on a timescale of $< t_{relax}$. This is distinct from collisionless systems, in which the time required to for these effects to occur goes beyond the timescale of the system. Galaxies are collisionless systems, as described in Sec. 1.3.2, and are hence treated by collisionless simulations without the need to consider computationally heavy particle encounters. In the context of N-body simulations t_{relax} will decrease with a lower N, and so for collisionless models where the systems typically contain higher particle numbers it is important to maintain a relaxation time longer than the set length of the simulation.

Collisional simulations match their total particle numbers to the typical abundance of the real systems they are modelling, with the particles of the model representing an individual star or DM particle. By contrast for collisionless models, which do not need to model individual interactions between particles, they instead draw a sample of particles from the smooth distribution representing the mass distribution of the system. The collisionless Boltzmann equation describes the distribution function $f(\mathbf{x}, \dot{\mathbf{x}}, t)$ of collisionless systems (Dehnen & Read, 2011)

$$0 = \frac{df}{dt} = \frac{\partial f}{\partial t} + \dot{\mathbf{x}} \cdot \frac{\partial f}{\partial \mathbf{x}} - \frac{\partial \Phi}{\partial \mathbf{x}} \cdot \frac{\partial f}{\partial \dot{\mathbf{x}}} \tag{2.3}$$

for a mass density of stars in six-dimensional phase space defined by the positions and velocities $(\mathbf{x}, \dot{\mathbf{x}})$ at a time t.

For a system in equilibrium, $\partial f/\partial t = 0$, also giving $\partial \Phi/\partial t = 0$; this allows the equation to satisfy the Jeans theorem, in which the f can be given by isolating integrals (integrals that constrain the phase-space) which restricts the system by one degree (Merritt, 2013). This simplification only applies in symmetrical cases, which does not apply to galaxies where some degree of triaxiality is present, such as after galaxy mergers (Gualandris et al., 2017).

Owing to the increased complexity at smaller scales required of collisional simulations, the number of particles that can be modelled is more limited than that of collisionless simulations considering the restrictions imposed by the costs of computational time. Larger particle numbers bring an increased accuracy but trade off with higher computational costs - if N is set too low, the particles will experience stochastic effects that lead to Brownian motion in simulations including particle numbers of up to $N = 10^6$. At the centres of galaxies, the MBH binary may be affected by relaxation during the stellar scattering phase as the star particles experience increased Brownian motion (Bortolas et al., 2016) and artificially increase the binary eccentricity (Nasim et al., 2020; Gualandris et al., 2022). Recent N-body simulations can reach up to 10^6 and approximately 10^9 particles for collisional and collisionless models respectively (Springel, 2005; Trenti & Hut, 2008; Dehnen & Read, 2011).

Determining the galactic particle dynamics at each evolutionary stage requires solving Eqn. 2.3. Given the large number of particles involved, this necessitates approximations to the model else the simulations become computationally unworkable. This is resolved for N-body models, where the particles are not representative of individual stars but instead a sample of the smooth distribution function, and the evolution of the simulation is determined by integrating the trajectories for each particle.

Integrator Choice

To update the particle dynamics in N-body simulations, there is a choice of time integrators of varying complexity. The Euler method is the simplest of these, consisting of a first-order Taylor expansion of the time-step to generate updates to the position and velocity of the particles. As such, it engenders a high error, proportional to Δt^2, unless the time-step is kept very low. It is also not reversible in time (it is not ‘time-symmetric’). Another method for the integration is the leapfrog integrator, a ‘symplectic’ integrator (an integrator that is designed to give solutions to an approximate Hamiltonian) that conserves energy well. This alternates between ‘kick’ steps, in which only the momentum changes in the calculation, and ‘drift’ steps, in which only the position changes. The equations are also second-order Taylor expansions, scaling the error proportional to Δt^3. The Hermite integrator then increases the order reached by the Taylor expansion to the fourth-order, a non-symplectic integrator that creates time-symmetric circular equations which require predictor-corrector steps to solve, in which the new positions and velocities are first predicted, then corrected with the new accelerations and the derivatives of the acceleration (Binney & Tremaine, 2008; Dehnen & Read, 2011).

Collisional simulations usually employ the fourth-order Hermite scheme, owing to the need for accuracy and its utility with short timescales, and use individual time-steps (e.g. Makino, 1991). Collisionless simulations on the other hand widely prefer the leapfrog integrator as it is time-symmetric and hence conserves energy well, and is a simple scheme to implement (e.g. Klypin & Prada, 2018).

Time-steps

Galaxies cover both the short timescales of MBH merger events as the black holes release GWs and coalesce, and the longer scales of galactic mergers. When examined by collisionless simulations, the obvious solution in which every particle shares a time-step and advance together gives rise to high computational costs with the large particle numbers of collisionless models, and so the popular alternative are solutions utilising variable time-steps.

The first of the two main alternatives is setting an individual time-step for each particle, wherein Δt_i is derived from the particle dynamics (Aarseth, 2003; Binney & Tremaine, 2008; Dehnen & Read, 2011). This can be useful at small scales within collisional simulations, but rapidly becomes unwieldy at the higher particle numbers required to model collisionless systems. By utilising block time-steps, this problem can be circumvented. Block (or hierarchical) time-steps sort the particles into discrete groups that evolve all the particles contained in a group together, typically ordered according to their dynamical properties. The applied time-step for a block is defined by

$$\Delta t_n = 2^{-n} \Delta t_0 \tag{2.4}$$

where n refers to the hierarchical group the particles have been placed in, and Δt_0 is the base time-step. These allow for individual time-step groupings without the prohibitive computational costs of assigning a unique time-step for each particle, with the downside that block steps are not time-symmetric (although there have been codes that attempt to bring time-symmetry to these simulations, e.g. by Makino et al. (2006), they require an impractical degree of computational time to run) (Dehnen, 2017; Hernandez & Bertschinger, 2018).

Regularisation

In collisional codes, the close encounters between particles cause the force to diverge and dominate the computation. Regularisation techniques can aid in the calculations of these close encounters in direct summation, by introducing a transformation to the coordinates of the interacting bodies that serves to remove the singularity in Eqn. 2.2 caused as $\mathbf{r}_i \to \mathbf{r}_j$.

The Kustaanheimo-Stiefel (KS) regularisation method presented in Stiefel & Kustaanheimo (1965) first changes the interaction to relative coordinates, solves the new set of equations with a new time coordinate, and obtains a new equation of motion that can be solved without the singularity before a final transformation back to the original, physical coordinates. Chain regularisation (also known as Aarseth-Mikkola regularisation) applies the KS regularisation technique to only the particles with the closest encounters with one another linked in a chain (Mikkola & Aarseth, 1993). KS regularisation is most useful for binaries and three-body interactions, whilst the reduced computations of chain regularisation makes it suitable for a larger number of particles. Chain regularisation can be applied to small N systems such as a simulation examining the stars surrounding an MBH binary (Aarseth, 2003; Dehnen, 2014). Regularisation may also introduce PN corrections for relativistic systems (e.g. Mikkola & Merritt, 2008).

2.1.2 Force Computation

The force calculations for the constituent particles in N-body simulations can be solved either exactly, or with varying degrees of approximation. The approximate calculations of the force are convenient to apply to large collisionless systems by grouping distant stars and approximating the forces as a group rather than making individual calculations, with a choice of different methods for efficiently estimating the total forces in the system in collisionless codes. Collisional simulations instead generally rely on direct summation of the forces to determine the evolution of the system.

Direct Summation

Direct summation is the simplest method for calculating the forces, in which Eqn. 2.2 is calculated directly for each particle against every other body in the system. With $(N-1)$ separate calculations to perform for each particle, this gives a minimum of $N\frac{(N-1)}{2}$ calculations per time-step, and scales as $\mathcal{O}(N^2)$. Direct summation simulations are limited to particle numbers of order 10^6 (Gualandris et al., 2017; Khan et al., 2020) owing to their computational complexity, at which resolution stochastic effects are problematic and lead to spurious Brownian motion (Bortolas et al., 2016) as well as a significant scatter in the eccentricity of the binary (Nasim et al., 2020; Gualandris et al., 2022). Close encounters between particles are treated with regularisation techniques. The lack of approximations and usability at low particle numbers has made direct summation a common feature in the majority of collisional codes where dealing with small-scale interactions between particles with accuracy is paramount, such as the codes ϕ-GRAPE and N-body6 (Harfst et al., 2007; Aarseth, 2003; Wang et al., 2015).

Tree Codes

While direct summation may perform well for collisional codes, for collisionless applications approximation becomes necessary as the particle numbers climb higher and two-body interactions are disregarded. One such type of integrator is tree codes, wherein clusters of particles are defined and grouped by their local densities. These groups undergo further splitting into sub-groups in particularly dense regions where the number of particles in a group exceeds n_{max}. The base cluster here is defined as the 'root' of the 'tree', and the further subdivisions form the rest of the tree. The method then utilises a multipole expansion for these groups to compute the forces. A common method of grouping is the 'oct-tree', in which a cube will split into eight sub-cubes until each group contains only one particle. The gravitational force from these clusters is then assessed in relation to particles distant from a group; if the opening angle that defines the cluster exceeds a set value when considered from the distant particle, as $\theta > \theta_0$, then the multipole expansion of the group does not proceed and the angles associated with the next set of subgroups is considered hierarchically. A smaller θ_0 makes the force computation more accurate, approaching the accuracy of direct summation as $\theta_0 \to 0$ (Barnes & Hut, 1986; Dehnen, 2000). The potentials in this hierarchical structure are computed using Eqn. 2.1, expanded using the multipole series to compute the forces for each group.

The potential for the system is defined by (Dehnen, 2014)

$$\Phi(\mathbf{x}_b) = -\sum_{i\neq j}^{i=N} G\mu_a \phi(\mathbf{x}_b - \mathbf{x}_a) \tag{2.5}$$

where ϕ is the Greens function for the system, μ_a is the particle mass at the source position, and x_b the sink position for a particle in the separate cell B. The Taylor expansion of the Greens function about the distance to $\mathbf{z}_A$ is then

$$\phi(\mathbf{x}_b - \mathbf{x}_a) \approx \sum_{|\mathbf{n}|\leq p} \frac{1}{\mathbf{n}!}(\mathbf{x}_a - \mathbf{z}_A)^{\mathbf{n}} \nabla^{\mathbf{n}} \phi(\mathbf{x}_b - \mathbf{z}_A) \tag{2.6}$$

where the distance between the particle a and the host cell centre is defined as $\mathbf{z}_A$, p is the expansion order, and G is taken into ϕ. The multi-index notation used here gives $\mathbf{n} \equiv (n_x, n_y, n_z)$ for $n_i \geq 0$, $|n| \equiv n_x + n_y + n_z$,$\mathbf{n}! \equiv n_x! n_y! n_z!$, and $\mathbf{r}^{\mathbf{n}} \equiv r_x^{n_x} r_y^{n_y} r_z^{n_z}$ (Dehnen & Read, 2011). Taken with Eqn. 2.5, this becomes

$$\Phi_A \approx - \sum_{|\mathbf{n}|\leq p} \mathcal{M}_{\mathbf{n}}(\mathbf{z}_A) \boldsymbol{\nabla}^{\mathbf{n}}(\mathbf{x}_b - \mathbf{z}_A) \tag{2.7a}$$

$$\mathcal{M}_{\mathbf{n}}(\mathbf{z}_A) = \sum_{a\in A} \mu_a \frac{(-1)^n}{\mathbf{n}!}(\mathbf{x}_a - \mathbf{z}_A)^{\mathbf{n}} \tag{2.7b}$$

with the multipole variable $\mathcal{M}_{\mathbf{n}}(\mathbf{z}_A)$ for cell A with respect to the cell centre. Tree codes scale as $\mathcal{O}(N\log(N))$, an improvement over direct summation for large particle numbers (Binney & Tremaine, 2008; Dehnen & Read, 2011). This method comes with larger force errors than direct summation codes, and although the treatment of mergers is worse than is desirable for a collisional simulation, it marks an improvement on a particle mesh method with the use of particles over a grid. It also allows for parallelisation of the codes, improving on the computational time (Dubinski, 1996).

Fast Multipole Method

The Fast Multipole Method (FMM) can then extend the utility of tree codes by performing the expansion twice, both in the source position as tree codes do, and additionally at the sink position. This local expansion improves the speed of calculations for the total particle number - the expansion in both x_a and x_b allows the local interactions between cells to dominate the force calculations, rather than the distant interactions dominating as they do in tree codes, as such reducing the computational cost of the algorithm. Judging the distances between the particles and their cell centres as distances $\mathbf{z}_A$ and $\mathbf{z}_B$, the vectors can be set as $\mathbf{r} = \mathbf{z}_B - \mathbf{z}_A$, $\mathbf{r}_a = \mathbf{x}_a - \mathbf{z}_A$, and $\mathbf{r}_b = \mathbf{x}_b - \mathbf{z}_B$. These vectors are illustrated in Fig. 2.2. The Taylor expansion of ϕ then becomes

$$\phi(\mathbf{x}_b - \mathbf{x}_a) \approx \sum_{|\mathbf{n}|\leq p} \sum_{|\mathbf{m}|\leq p-n} \frac{(-1)^n}{\mathbf{n}!\mathbf{m}!}(\mathbf{r}_b)^{\mathbf{n}}(\mathbf{r}_a)^{\mathbf{m}} \nabla^{\mathbf{n}+\mathbf{m}} \phi(\mathbf{z}_B - \mathbf{z}_A) \tag{2.8}$$

with G again taken into ϕ. Taking the potential in Eqn. 2.5, the potential of the particles in cell A acting on a point $\mathbf{x}_b$ in cell B is

$$\Phi_{A\rightarrow B}(\mathbf{x}_b) \approx \sum_{|\mathbf{n}|\leq p} \frac{(\mathbf{r}_b)^{\mathbf{n}}}{\mathbf{n}!} \mathcal{F}_{\mathbf{n}}(\mathbf{z}_B) \tag{2.9a}$$

$$\mathcal{F}_{\mathbf{n}}(\mathbf{z}_B) = \sum_{|\mathbf{m}|\leq p-n} \mathcal{M}_{\mathbf{m}}(\mathbf{z}_A) \boldsymbol{\nabla}^{\mathbf{n}+\mathbf{m}} \phi(\mathbf{r}) \tag{2.9b}$$

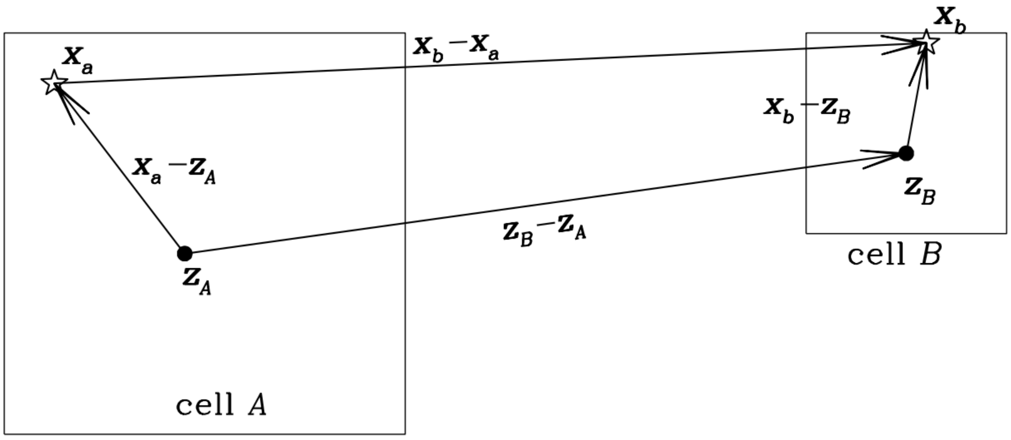

Figure 2.2: An illustration of the vectors between cell interactions in FMM, from a particle at $\mathbf{x}_a$ in cell A to particle at $\mathbf{x}_b$ in cell B. Figure from Dehnen & Read (2011).

with $\mathcal{F}_\mathbf{n}$ denoting the field tensor, a new variable. The computational speed is improved over the $\mathcal{O}(N\log(N))$ of tree codes, with the typical scaling for the computational cost at $\mathcal{O}(N)$ (Dehnen, 2000; Dehnen & Read, 2011).

Particle Mesh

Distinct from the particle based procedures described prior, the particle mesh method uses a grid-based system to compute the forces. These solve the Poisson equation for densities at the nodes of a grid applied across the simulation, where the grid is made up of regularly spaced cells. The differential form of the Poisson equation for the gravitational potential is given by (Binney & Tremaine, 2008)

$$\nabla^2\Phi(r) = 4\pi G\rho(r) \tag{2.10}$$

where ρ is the density. Accelerations for the cells are obtained by differentiation from the Poisson potential; the densities are computed at the nodes of the grid, the fast Fourier transform (FFT) method is then typically used to solve Eqn. 2.10, and the accelerations are then interpolated for each of the particles. The resolution of the model is hence constrained by the number of cells assigned in the mesh (Klypin & Holtzman, 1997; Melott et al., 1997). The cells are sized equally in a fixed grid method, with the alternative adaptive mesh refinement methods improving the resolution by concentrating higher numbers of cells in areas with more particles (Passy & Bryan, 2014). Particle mesh models are typically useful for cosmological models, which do not require a high degree of accuracy at small scales.

2.1.3 Softening

Within collisionless simulations, at small scales as particles approach one another the resulting calculations cause an ultraviolet divergence in the potential. Considering Eqn. 2.2, this issue manifests within simulations as $\mathbf{F}_i \to \infty$ when $|\mathbf{r}_i - \mathbf{r}_j| \to 0$. Whilst collisional simulations include close two-body interactions, collisionless simulations apply a limiting 'softening' length at small scales to avoid infinite forces as particles approach one another

(Dehnen, 2001). A softening parameter, ϵ, is applied to limit this problem by quelling the gravitational force below that distance, substituting individual particles in the galaxy with distributions of the same mass out to the softening length (as touched on in Sec. 2.1.1) (Aarseth, 1963; Dehnen, 2001; Aarseth, 2003). By modifying the gravitational potential, the softening prevents the force from diverging at small scales. This is implemented via a softening kernel. For the gravitational potential and force, as given by Eqn. 2.1 and Eqn. 2.2, with a softening kernel the equations become (Dehnen & Read, 2011)

$$\Phi(\mathbf{r}_i) = -G \sum_{i \neq j}^{i=N} S(r_{ij}, \epsilon) m_i m_j \tag{2.11a}$$

$$F(\mathbf{r}_i) = -G \sum_{i \neq j}^{i=N} S_F(r_{ij}, \epsilon) m_i m_j \frac{\mathbf{r}_i - \mathbf{r}_j}{r_{ij}} \tag{2.11b}$$

where $S(r_{ij}, \epsilon)$ is the softening kernel with $S_F(r_{ij}, \epsilon)$ the first derivative thereof, for a distance $r_{ij} = |\mathbf{r}_i - \mathbf{r}_j|$ between two particles.

Within collisionless N-body simulations, the softening is implemented with the set distance acting as a barrier to the diverging forces that would give rise to impractically high computational costs. This introduces a systematic error to the simulation results, a trade-off against the unphysical behaviour that would otherwise occur. Different forms of the softening kernel can be used, with a bearing on the resultant error. The commonly used Plummer softening represents the particles as Plummer spheres, where ϵ is set to the scale radius of the sphere (Dyer & Ip, 1993; Barnes, 2012). This results in a softening kernel of

$$S(r_{ij}, \epsilon) = -\frac{1}{(r_{ij}^2 + \epsilon^2)^{1/2}} \tag{2.12}$$

and so the softened gravitational force Eqn. 2.11b becomes

$$\mathbf{F}_i = -G \sum_{i \neq j}^{i=N} \frac{m_i m_j (\mathbf{r}_i - \mathbf{r}_j)}{(|\mathbf{r}_i - \mathbf{r}_j|^2 + \epsilon^2)^{\frac{3}{2}}} \; . \tag{2.13}$$

There are different ways to determine the appropriate softening length - the minimum recommended value is to overcome the two-body scattering between particles. For a collisionless system this is given by (Dehnen & Read, 2011)

$$\epsilon_{min} \sim \frac{G\mu}{\sigma^2} \tag{2.14}$$

where μ is the individual particle mass in the simulation, and σ is the stellar velocity dispersion. However, setting the softening at the minimum value is not always the best choice for the simulation, despite the increased accuracy at lower softening values. Another definition can be derived by substituting $M = N\mu^2$ into Eqn. 2.14, for the situation of modelling N star particles. With $G\mu/\epsilon^2 \lesssim GM/R^2$, a constraint on the softening obtained by limiting the maximum force between particles to the mean field strength, then

$$\epsilon \sim \frac{R}{N^{1/2}} \tag{2.15}$$

where the radius of the system is given by R with total mass M (Power et al., 2003; Dehnen & Read, 2011).

The softening length presents an issue for following MBH mergers, as below the set distance the results obtained cannot be trusted. But although smaller softenings allow the merger evolution to be tracked for longer they are also more computationally heavy, and utilising Eqn. 2.14 may not be a feasible choice for simulations with large particle numbers or those running over long time periods.

2.2 GRIFFIN

With semi-analytic models and cosmological models both demonstrating flaws in their analysis of MBH mergers (see Sec. 1.7), there is still a need for new developments in the field for modelling these events. To be able to obtain accurate MBH merger statistics for upcoming GW detections, detailed modelling requires high accuracy numerical techniques able to reduce force errors, and ensure a reliable treatment of the energy and angular momentum transfers with stars (Vasiliev et al., 2014). This includes treatment of the binary phases beyond dynamical friction; both stellar scattering and the final emission of GWs at the MBHs coalesce.

Raising the total number of particles within a simulation whilst simultaneously maintaining a bound on force errors is challenging, with the force calculations requiring an increasingly smaller softening as N grows, becoming progressively more computationally expensive (Dehnen, 2000). The operational scaling for FMM codes can improve to a complexity of $\mathcal{O}(N)$ (Fong & Darve, 2009; Dehnen, 2014), but a better simulation resolution has been achieved in the fast multipole method code GRIFFIN.

2.2.1 An Adaptive Fast Multipole Method

GRIFFIN is a Fast Multiple Method code, with a more detailed discussion of the FMM algorithm provided in Sec. 2.1.2. With a sophisticated monitoring of errors and adaptive choice of parameters, the code improves on the the computational cost of prior FMM models (Dehnen, 2002, 2014). This error monitoring is performed through initial estimations of the force error as a result of the interactions between the particle groups; these estimations then set the ensuing force expansion centre placements. The force expansion centres, here labelled $\mathbf{z}$ and $\mathbf{s}$ for the source and sink cell centres respectively, are taken as the geometric centre of the cell cube in conventional FMM - this choice contributes significantly to the resulting large tail in the resultant force error distribution. In the implementation of the algorithm in GRIFFIN, after the force error estimation is made the positions are instead chosen by finding the centre of the smallest sphere encompassing the group particles, hence reducing the error along with the area considered. Appropriate values for the remaining parameters p and ϵ are then adopted with consideration to minimising the error once again, with p being set by the code after the appropriate softening choice is determined (e.g. by Equation 2.14) for the simulation in question. These parameters then provide the optimum scaling for the given N particles, and with this method GRIFFIN is consequently able to utilise a high particle number whilst keeping force errors in check.

This adaptive parameter selection improves upon the computational cost from $\mathcal{O}(N)$, with a best performance of scaling $\mathcal{O}(N^{0.87})$ for relative force errors of $\sim 10^{-7}$ (Dehnen, 2014). The resulting distribution of force errors is similar to that of a direct summation code, whilst retaining the $\mathcal{O}(N)$ scaling of the FMM technique. With these improvements, GRIFFIN has been shown to perform similarly to a direct summation code in modelling the evolution of MBH binaries formed in galactic mergers (Nasim et al., 2020, 2021).

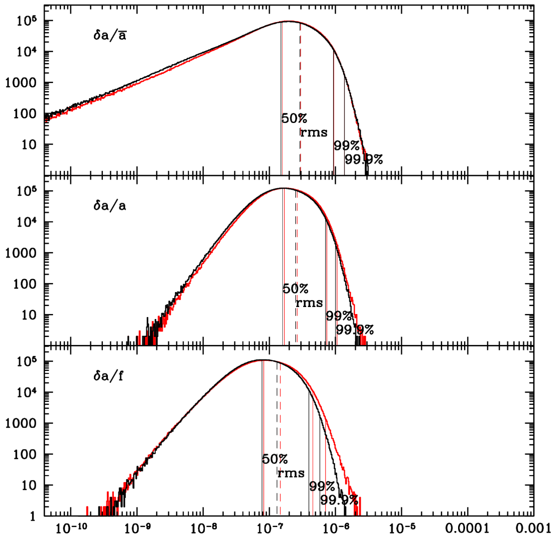

Figure 2.3: The probability distribution function of acceleration errors for $N = 10^7$ particles drawn from a Plummer sphere, with an adaptive FMM run (red lines) and for a direct summation run (black lines) with two variations on softening, with $\epsilon = 2 \times 10^{-7}$ (left) and $\epsilon = 10^{-7}$ (right). The panels show the normalised by the mean acceleration (top), relative (middle), and scaled by the force (bottom) acceleration errors. Figure from Dehnen (2014).

This makes GRIFFIN useful with a sufficient set of assigned parameters in examining the timescales of the different phases of evolution an MBH binary undergoes. Figure 2.3 shows the distribution of acceleration errors for the algorithm including the adaptive parameter selection. The distribution lacks the extended force error tail in the distribution typically seen in FMM, owing to the bound placed on the maximum force error. The adaptive FMM behaviour shown in comparison is similar to the direct summation errors for the same particle number ($N = 10^7$).

By contrast, Gualandris et al. (2017) demonstrated that the standard collisionless tree-code GADGET2 did not provide adequate accuracy in examining the dynamics surrounding the MBHs in the loss-cone, as shown in contrast to the well-performing GRIFFIN and the collisional code ϕ-GRAPE in Figure 2.4.

2.2.2 Usage

The softening length in GRIFFIN has the option of being set with different kernel choices. P_0 denotes the standard Plummer softening, as in Eqn 2.12. The near-Plummer variation given by P_1 is the default setting for the code, with $S(r_{ij}, \epsilon) = -1/(r^2 + \epsilon^2)^{5/2}$. The additional settings P_2–P_3 are also near-Plummer possibilities, where the variation is in the Taylor expansion. As all available kernels are either Plummer or variants on the Plummer softening, there is a significant error induced as a result of giving the kernel an infinite extent, with the modifications in the near-Plummer models serving to bring this error closer to Newtonian gravity (Dehnen, 2001).

The simulation particles are divided into ‘standard’, ‘gas’, and ‘sink’ particles. Dark matter, and stellar particles are all input to GRIFFIN as standard particles, and gas particles labelled as ’gas’. Black holes are labelled as sink particles, for which the particle-to-particle interactions are computed with direct summation rather than the adaptive FMM of the

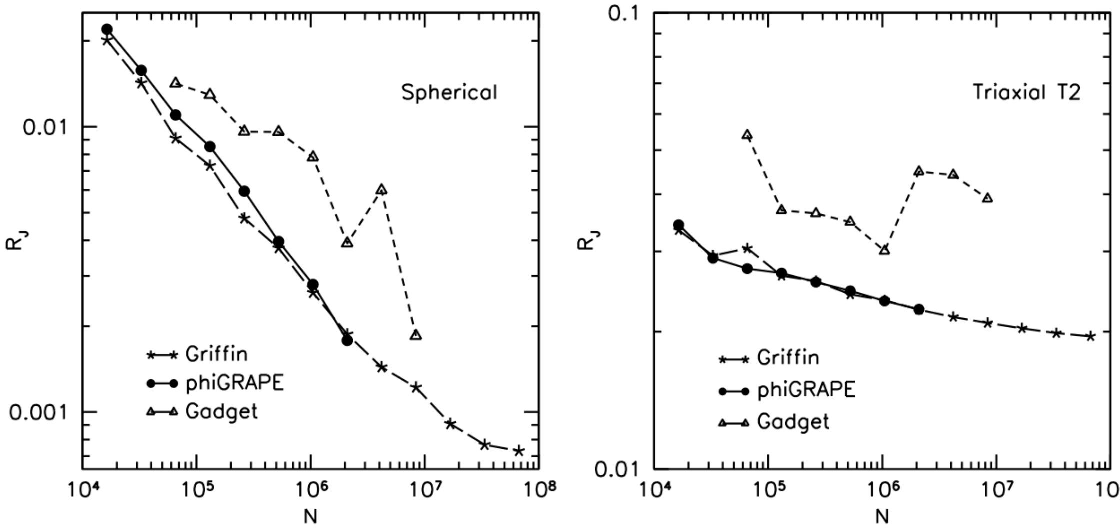

Figure 2.4: The loss-cone repopulation factor R_J against simulation particle number for the codes GRIFFIN, ϕ-GRAPE and GADGET2, with spherical (left) and triaxial (right) models. Figure adapted from Gualandris et al. (2017).

standard particles. This applies to both interactions between BHs with one another, and with standard and gas particles. Different softening lengths may be used for each type of particle, allowing the BHs to be treated with a greater precision than standard particles without compromising the lower computational cost of the simulation.

The Multi-Resolution Scheme

3.1 Introduction

As discussed in Chapter 1, future explorations of GW signals detected at PTA frequencies will require information on MBH binary coalescence timescales for astrophysical interpretation. Modelling of MBHs embedded in merging galaxies is provided by high accuracy simulations of individual mergers by means of direct summation simulations (e.g. Gualandris et al., 2022), hybrid collisionless and collisional simulations (e.g. Nasim et al., 2021), and hybrid collisionless/regularised simulations (e.g. Rantala et al., 2017). Direct summation simulations achieve low force errors by brute force calculations of all pairwise gravitational forces, but are limited to particle numbers of order a million by their $\mathcal{O}(N^2)$ computational scaling (Gualandris & Merritt, 2012b; Gualandris et al., 2022; Khan et al., 2020). At these low resolutions, stochastic effects lead to spurious Brownian motion of the binary (Bortolas et al., 2016) as well as a significant scatter in the eccentricity of the binary (Nasim et al., 2020). Accurate MBH merger timescale estimations hence require a statistically representative sample of the binaries and their hosts, and modelling galaxies and galactic mergers at high resolutions of $N \gtrsim 10^7$ is required to mitigate spurious relaxation and the stochastic effects present in the evolution of an MBH binary (Nasim et al., 2020). This higher resolution can present a numerical challenge owing to the large range of spatial and temporal scales involved in galaxy and MBH binary mergers, as to reach sufficient particle numbers even with a more efficient code such as GRIFFIN the computational time can become prohibitive.

In this chapter, I present a numerical scheme to increase resolution in the central regions of galaxies based on mass refinement. A high resolution at the centres of galaxy simulations is necessary for the proper treatment of the central MBHs, and an accurate calculation of their dynamics to model the phases of MBH binary inspiral. I present results from both isolated and merging galaxies with central MBHs evolved using the adaptive FMM code GRIFFIN (as described in detail in Sec. 2.2), utilising a method that preferentially distributes the stellar and DM particles closer to the central region of interest to generate the initial conditions and comparing with reference models. This multi-resolution method allows for an increase in the effective resolution in the galactic center, the area pertaining to MBH binary dynamics, without any adverse effects on stability or dynamical evolution. In particular, I show that a mass refined $N = 10^6$ galaxy model behaves similarly to a $N = 10^7$ reference galaxy model.

The content of this chapter was adapted from a submission to Monthly Notices of the Royal Astronomical Society (MNRAS), as *A multi-resolution method for modelling galaxy and massive black hole mergers*, Attard, Gualandris, Read, and Dehnen.

3.2 Multi-Resolution Scheme

Multi-resolution models of the type presented in this work have been adopted in the literature to enhance the resolution of a galaxy model within the areas of interest, such as presented in Cole et al. (2012) in which the sampling probability is set by the inverse of a function relating the particle mass ratio and the orbital radius and compensating the oversampling with a corresponding mass increase. The technique allows a reduction in the total particle number by half at the same central resolution without any adverse effects.

Here, I implement a multi-resolution refinement scheme designed to increase the resolution in the central regions of galaxy models, with the aim of accurately modelling the evolution of MBH mergers formed in galactic mergers at a reduced computational cost. These models have previously been used for isolated galaxies; in this work I test the viability of a multi-resolution scheme for both isolated and merger models. Galactic mergers are violent events that affect the distribution of stars at both large and small scales, and as such it is not guaranteed that the refinement will work over time in a merger simulation. However, the 'mixing theorem' shows that N-body simulations should preserve central phase space density, even through mergers (Dehnen, 2005). Following this, the high resolution regions at the centre of each merging galaxy should overlap once the merger is complete.

3.2.1 Refinement Scheme Implementation

I present the implementation of a multi-resolution scheme that works to increase the resolution in the central regions of galaxy models, with the aim of accurately modelling the evolution of MBH binaries formed in galactic mergers at a reduced computational cost. In the case of multi-component models featuring a central MBH, a stellar bulge, and a DM halo, the scheme is applied independently to the bulge and the halo, ensuring the central regions (dominated by bulge particles) will be adequately over-seeded.

Starting from a desired final total particle number for each component, which I denote $N_{\rm b}$ and $N_{\rm h}$, particles were first oversampled by a factor k, termed the multiplication factor, and then coarse-grained based on their radial position. A number of radial zones can be defined such that particles in the innermost zone are left unchanged, while only a given fraction of particles are retained in the outer zones. This retainment fraction decreases in zones moving away from the galaxy centre. The mass of each particle in the outer zones were then increased by the same oversampling factor k to ensure that the total mass in the galaxy and the mass density profile are unaffected. By adopting a larger number of zones for higher multiplication factors, the increase in particle masses at the outermost radii is reduced. With this increase of zones, it is possible to increase the resolution in the central region of the galaxy whilst avoiding large jumps in particle masses between the radial zones, which would otherwise induce spurious mass segregation.

The two different implementations of the scheme utilised, labelled 'a' and 'b', have their parameters listed in Table 3.1. Scheme 'a' is the standard implementation, characterised by $n = 3$ zones, while scheme 'b' is a more aggressively refined scheme with an increased $n = 4$ zones. Scheme 'b' can be considered to be a physically motivated implementation, as the innermost radial bin is equal to twice the radius of the $R_{\rm infl}$ of the central MBH, as given by Eqn. 1.8.

The zone radial boundaries and mass multiplication factors are given in Table 3.1. For scheme 'a', the resolution of the central radial zone is set at 5 times the total particle number, and the extent of the model is initially overseeded by this factor. The number of particles in the central zone remains unchanged from the initial overseeding. The percentage of particles of N_b and N_h contained within the central zone are set at 50%, and the radial boundary of the zone is then set by this. The particle number is then reduced by a factor of 5 for each successive radial zone, and the multiplication factor for the remaining particle masses increases correspondingly. Scheme 'b' is similar, with an additional zone being added to prevent an excessively large increase in mass in the outermost radial zone. This additional zone divides the 50% share of the particles, with

Table 3.1: The parameters of the refinement scheme: scheme identifier, the oversampling factor k, zone number for bulge z_b, zone number for halo z_h, mass multiplication factor m, and start and end radius (r_0-r_1, kpc) of each zone.

Scheme	k	z_b	z_h	m	r_{b0}	r_{b1}	r_{h0}	r_{h1}
a	5	1	1	1	0.0	1.06	0.0	18.70
		2	2	5	1.06	7.15	18.70	62.80
		3	3	25	7.15	–	62.50	–
b	10	1	1	1	0.0	0.18	0.0	4.98
		2	2	2.53	0.18	1.31	4.98	21.50
		3	3	10	1.31	7.15	21.50	62.80
		4	4	40	7.15	–	62.80	–

1% of particles in the innermost zone and 49% in the subsequent zone. The multiplication factor for the additional zone is then set based on these restrictions.

3.3 Initial Conditions

The schemes were applied to a set of multi-component models representative of massive elliptical galaxies consisting of a stellar bulge, a dark matter (DM) halo, and a central MBH. The central MBH is modelled as a Plummer sphere (Plummer, 1911) of zero scale length, and placed at the centre of each model. The stellar bulge follows a Sérsic profile in projection (Eqn. 1.3, Sérsic, 1963; Sersic, 1968) with $n = 4$, appropriate for elliptical galaxies, as in the de Vaucouleurs profile (de Vaucouleurs, 1948). The DM halo follows an NFW profile (Eqn. 1.1, Navarro et al., 1996).

The first step of the initial conditions, the MBH mass, was set by merger trees extracted from the IllustrisTNG-300-1 cosmological simulation, chosen from the IllustrisTNG suite for the highest resolution of the largest volume runs (Pillepich et al., 2019; Springel et al., 2018; Marinacci et al., 2018; Nelson et al., 2019; Naiman et al., 2018). I selected a major merger at low redshift whose central MBH is an expected PTA source, in which the MBH has a mass $M_{\rm bh} = 7.14 \times 10^8\,{\rm M}_\odot$. The parameters for the bulge and halo components were then set using observational scaling relations. The stellar bulge mass $M_{\rm b}$ is derived from the MBH-stellar mass relation (Eqn. 1.6, Kormendy & Ho, 2013; Reines & Volonteri, 2015) with the elliptical parameters $\alpha = 8.95 \pm 0.09$ and $\beta = 1.40 \pm 0.21$. This gives a bulge mass of $M_{\rm b} = 8.54 \times 10^{10}\,{\rm M}_\odot$.

The halo mass $M_{\rm h}$ was then determined from the halo-stellar mass scaling relation of Chae et al. (2014) for massive elliptical galaxies, with a typical value $M_{\rm h} = 5.04 \times 10^{12}\,{\rm M}_\odot$ (see Sec. 1.3.2). The virial radius R_{200} is derived from the relation with the halo mass

$$M_{\rm h} = 200\rho_c \frac{4}{3}\pi R_{200}^3 \,, \tag{3.1}$$

with $\rho_c = 136.05\,{\rm M}_\odot\,{\rm kpc}^{-3}$ (Binney & Tremaine, 2008), which gives $R_{200} = 353.69\,{\rm kpc}$. The scale radius of the NFW profile is given by $a = R_{200}/c$, where the concentration parameter c is derived from the $c - M_{\rm h}$ relation in Dutton & Macciò (2014). Lastly, we set the half-mass radius of the stellar component using the relation $R_{1/2} = 0.015R_{200}$ (Kravtsov, 2013), giving $R_{1/2} = 5.30\,{\rm kpc}$.

The action-based galaxy modelling software library Agama (Vasiliev, 2019) was utilised to sample the total gravitational potential of the multi-component galaxy system, and con-

Table 3.2: Properties of the adopted galaxy models: model identifier, type of model (isolated or merger), total particle number, number of halo particles, number of bulge particles, number of particles within the $5R_{\rm infl}$ in the initial models, minimum halo star to MBH mass ratio, minimum bulge star to MBH mass ratio, and central resolution multiplication factor for the models with mass refinement.

Run	Type	N	$N_{\rm h}$	$N_{\rm b}$	$N(5R_{\rm infl})$	$m_{\rm h}/M_{\rm bh}$	$m_{\rm b}/M_{\rm bh}$	Scheme
I6	Isolated	10^6	9×10^5	1.05×10^5	1.3×10^4	7.84×10^{-3}	1.14×10^{-3}	-
I7	Isolated	10^7	9×10^6	1.05×10^6	1.3×10^5	7.84×10^{-4}	1.14×10^{-4}	-
I6a	Isolated	10^6	9×10^5	1.05×10^5	5.7×10^4	1.57×10^{-3}	2.38×10^{-4}	$k = 5$
I6b	Isolated	10^6	9×10^5	1.05×10^5	6.0×10^4	7.84×10^{-4}	1.14×10^{-4}	$k = 10$
I7a	Isolated	10^7	9×10^6	1.05×10^6	5.7×10^5	1.57×10^{-4}	2.27×10^{-5}	$k = 5$
I7b	Isolated	10^7	9×10^6	1.05×10^6	5.9×10^5	7.84×10^{-5}	1.14×10^{-5}	$k = 10$
M6	Merger	10^6	9×10^5	1.05×10^5	2.5×10^4	7.84×10^{-3}	1.14×10^{-3}	-
M7	Merger	10^7	9×10^6	1.05×10^6	2.5×10^5	7.84×10^{-4}	1.14×10^{-4}	-
M6a	Merger	10^6	9×10^5	1.05×10^5	1.1×10^5	1.57×10^{-3}	2.38×10^{-4}	$k = 5$
M6b	Merger	10^6	9×10^5	1.05×10^5	1.2×10^5	7.84×10^{-4}	1.14×10^{-4}	$k = 10$
M7a	Merger	10^7	9×10^6	1.05×10^6	1.1×10^6	1.57×10^{-4}	2.27×10^{-5}	$k = 5$
M7b	Merger	10^7	9×10^6	1.05×10^6	1.2×10^6	7.84×10^{-5}	1.14×10^{-5}	$k = 10$

struct initial conditions in equilibrium for the simulations. The units were set such that $G = 1$, $R = 1\,\rm kpc$ and $M = M_{\rm b}$. I generated isolated models, denoted with identifier 'I', at two reference resolutions, $N = 10^6$ and $N = 10^7$, and applied the 'a' and 'b' mass refinement schemes described in Section 3.2.1 for each resolution. I then set up equal mass mergers of two independent realisations of the same multi-component model, denoted with identifier 'M', at the same resolutions. Galaxies were placed on bound Keplerian orbits of eccentricity $e = 0.7$ and at an initial distance of $D = 378.6\,\rm kpc$. The initial eccentricity is relatively high, in agreement with typical orbits in large scale cosmological simulations (Khochfar & Burkert, 2006), but not so high to result in a head-on galaxy collision. The initial distance was set to $R \simeq 9\,R_s$, where R_s represents the scale radius of the NFW model describing the halo of the galaxies, defined as the radius where the particle number drops to half of the total.

The parameters of all models are listed in Table 3.2, including the total particle number N, the number of halo and bulge particles, and the ratio of halo/bulge particle mass to the MBH mass. The final column gives the numerical multiplier k adopted in the mass refined schemes, which marks the factor by which the schemes are first overseeded in comparison to the reference model. A commonly adopted mass factor to avoid mass segregation is of order 10 (Alexander & Hopman, 2009), as utilised in both schemes.

While the ratio between a halo particle mass and a bulge particle mass is equal for all models ($m_h/m_b \sim 6.7$), the MBH to bulge particle mass ratio at the innermost radial shell decreases as the refinement scheme becomes more aggressive. In particular, I6b has the same $m_{\rm b}/M_{\rm bh}$ as I7, and the smallest ratio is obtained for I7b.

3.3.1 Numerical Simulations

Each of the models were evolved with the code GRIFFIN (Dehnen, 2014), described in detail in Section 2.2. The simulations each use a multipole expansion order $p = 5$. The softening parameter was initially set to $\epsilon = 30\,\rm pc$ for star-star interactions, and to $\epsilon_{\rm bh} = 10\,\rm pc$ for MBH-MBH and MBH-star interactions for all models. The softening length $\epsilon_{\rm bh}$ in the merger simulations is then reduced to 5 pc after a time ~ 2 Gyr, corresponding to just prior to the end of the dynamical friction phase. This setup allows computational time to be reduced in the early stages of the merger, driven by dynamical friction, and yet to accurately model the evolution of the MBH binary through the rapid hardening phase dominated by encounters with background stars. The softening length choice for the sink particles is always smaller than the radius of influence of the MBH, in order to resolve the dynamical friction phase (Colpi et al., 2019; Tremmel et al., 2015; Pfister et al., 2019). The softening kernel employed is a near-Plummer variation for smooth source particles with a density $\rho \propto (r^2 + \epsilon^2)^{-3.5}$.

All simulations were evolved until the binary reached a separation of the order of softening length $\epsilon_{\rm bh}$, below which the dynamical evolution is no longer reliable. This separation is always ensured to be smaller than the hard-binary separation a_h.

3.4 Evolution of the Multi-Resolution Models

Here I examine the evolution of the isolated and merging multi-resolution galaxy models and compare to the reference resolutions. Of particular interest are the merger models, to see if they can retain the higher central resolutions of the multi-resolution model particle distributions at the initial time throughout the violent merger event.

The distribution of bulge particles in the isolated models, with and without the mass refinement, is shown in Figure 3.1 at the initial time and a late time in the evolution. This illustrates the efficacy of the refinement schemes, with increased population in the central regions of models ‘a’ and ‘b’. The multi-resolution models retain their higher central resolution to later times, in agreement with earlier studies (Cole et al., 2012). Crucially, this holds true in the merger models as well, as shown in Figure 3.2, despite the violent mixing that occurs during the merger process. Models M6a and M6b achieve a population within the central ~ 100 pc similar to model I7.

The radial density profiles shown in Figures 3.3 and 3.4 support these conclusions from the particle distributions. The schemes are effective at populating the central regions of the models, and the distributions are stable over time for both the isolated and merger models. The flattening observed in the inner density profiles of the merger models can be attributed to core scouring during the hardening phase of the black hole binary, as described in Section 1.5.2. The ‘b’ models consistently increase the central resolution more effectively than the ‘a’ models, as expected from the more aggressive application of the scheme, but maintain stability in the models as well as the ‘a’ scheme.

The shape of the modelled galaxies can be characterised through calculation of the axis ratios of an ellipsoid fit to the stellar distribution, defined as

$$1 = \left(\frac{x}{a}\right)^2 + \left(\frac{y}{b}\right)^2 + \left(\frac{z}{c}\right)^2 \tag{3.2}$$

where $a > b > c > 0$ are the axes of symmetry of an ellipsoid. The ratios b/a and c/a are then at perfect sphericity at unity, and depart from this with b and c axis length decreases (de Zeeuw, 1985; Bortolas et al., 2018). Here these ratios are calculated using Pynbody, a Python package for analysis of astrophysical simulations (Pontzen et al., 2013). The triaxiality parameter provides a measure of the departure from sphericity, computed as

$$T = \frac{1 - b^2/a^2}{1 - c^2/a^2} \tag{3.3}$$

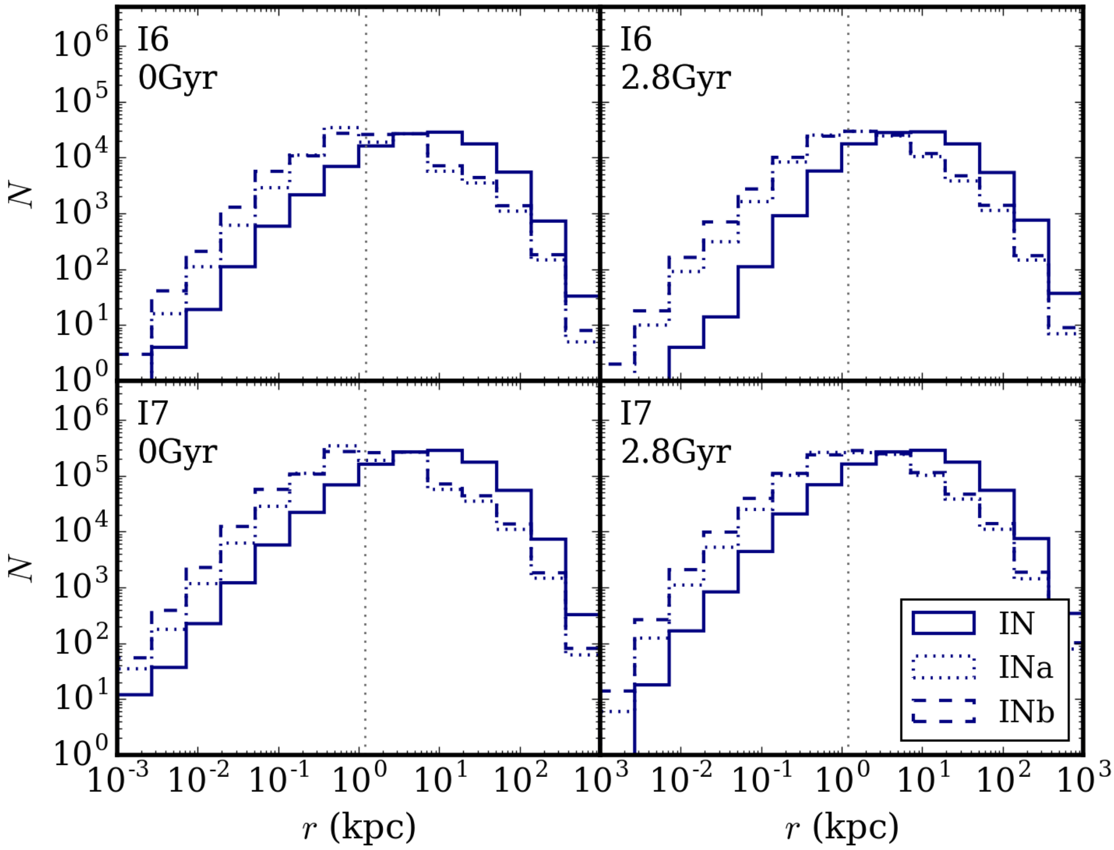

Figure 3.1: Radial distribution of the bulge particles for all isolated models with $N = 10^6$ particles (top panels) and $N = 10^7$ (bottom panels) at two characteristic times: $t = 0\,\text{Gyr}$ (left) and $t = 2.8\,\text{Gyr}$ (right), corresponding to a late time in the evolution. The grey dotted line represents the $5R_{\text{infl}}$ radius. A significant increase in the particle number $< 10\,\text{kpc}$ is observed for the models with the multi-resolution scheme applied, and no significant expansion occurs over time for these models.

which varies as $T > 0.5$ for prolate spheroids, $T < 0.5$ for oblate spheroids, and $T = 0.5$ for perfect triaxiality. The spatial evolution of the axis ratios for the stellar bulge of each simulation, including T for the merger models, are shown for the isolated models in Figure 3.5 and for the merger models in Figure 3.6. In all isolated models, the sphericity is maintained over the time evolution, save for a noticeable departure at the central radii in model I6. This is likely to be the effect of a lower number of particles at the innermost radial bins making the axis ratios harder to evaluate, which is improved in the models with the multi-resolution scheme applied. This evaluation holds for the merger models, with the shape of the stellar distribution remaining unaffected by the usage of the multi-resolution scheme. The merger models display triaxiality, as expected in a galaxy merger remnant, here as prolate ($T > 0.5$) (Gualandris et al., 2017; Bortolas et al., 2018).

The 3D velocity dispersion profiles shown in Figures 3.7 and 3.8 show results in line with the expansion displayed at inner radii by I6 and M6 in the particle distributions, with I6 and M6 here showing an evolution $\gtrsim 0.2\,\text{kpc}$ of increased σ, which is not present in the higher resolution models.

The velocity anisotropy β profiles are shown in Figures 3.9 and 3.10, calculated using

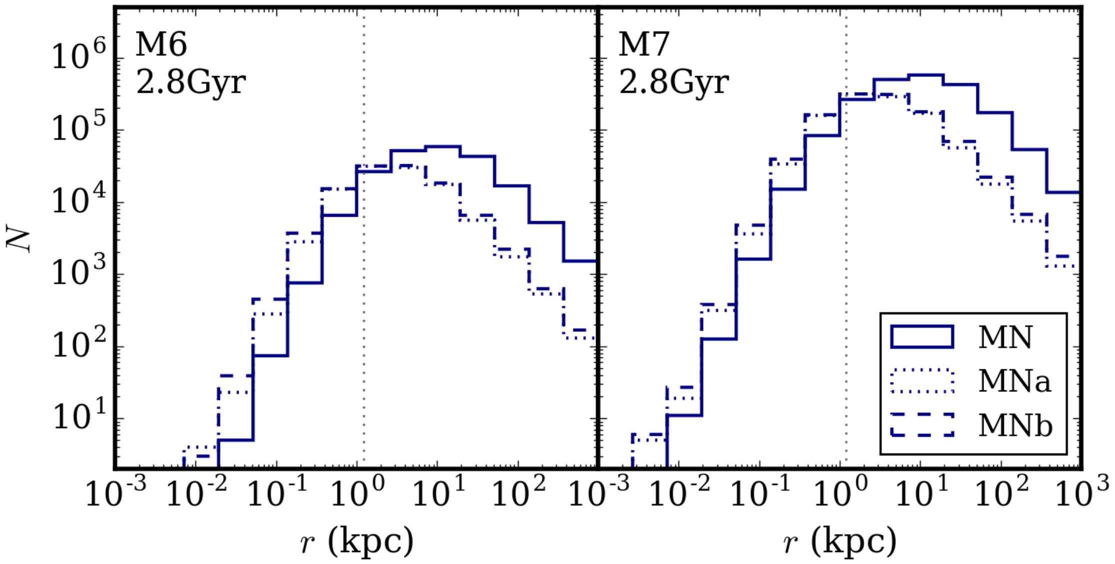

Figure 3.2: Radial distribution of the bulge particles for all merger models with $N = 10^6$ particles (left) and $N = 10^7$ (right), both at the later time $t = 2.8\,\mathrm{Gyr}$ past the end of the merger process. The grey dotted line represents the $5R_{\mathrm{infl}}$ radius. A higher central resolution is maintained for the models with the multi-resolution scheme applied post-merger, most significantly in the M6 models.

Pynbody which utilises the definition (Binney & Tremaine, 2008)

$$\beta(r) = 1 - \frac{\sigma_\theta^2(r)}{\sigma_r^2(r)} \tag{3.4}$$

where $\sigma_\theta(r)$ is the tangential velocity dispersion and $\sigma_r(r)$ is the radial velocity dispersion. β measures the radial anisotropy of the system: for isotropic orbits $\beta(r) = 0$, and and deviates as $\beta(r) > 0$ for radially biased orbits and $\beta \to \infty$ for circular orbits (Binney & Tremaine, 2008; Read et al., 2021). Here, the isolated models show $\beta(r) \simeq 0$ across the run with the exception of the I6 evolution, which displays an increase towards radial bias over time. The merger models display an expected anisotropy with an inner tangential bias, imparted from core scouring as the stellar scattering phase of binary evolution preferentially ejects stars on radial orbits (Quinlan & Hernquist, 1997; Thomas et al., 2014), and an outer radial bias beyond $\sim 300\,\mathrm{pc}$.

Combined with the particle distributions and the density profiles, it can be shown that the scheme does not affect the properties of the isolated models or the remnant galaxy at the central radii, and as such has potential utility in simulations with the purpose of examining galactic dynamics in addition to the MBH studies I focus on here.

The Lagrangian radii shown in Figures 3.11 and Fig. 3.12 for isolated and merger models, respectively, reveal that a small expansion takes place in the bulge particles, and predominantly those at lower radii. This effect is owed to relaxation effects at small radii and at lower resolutions, as indicated by the dependence of the effect on particle number and radius. The expansion lessens with increasing radius, due to an increase in relaxation time with radius, and is almost negligible in both the refined $N = 10^6$ models and all the $N = 10^7$ models. Furthermore, it does not affect the halo particles. The strong variations seen at $t = 2.0 - 2.5\,\mathrm{Gyr}$ in the merger models are a signature of the merger process, and can be taken as a measure of the merger time.

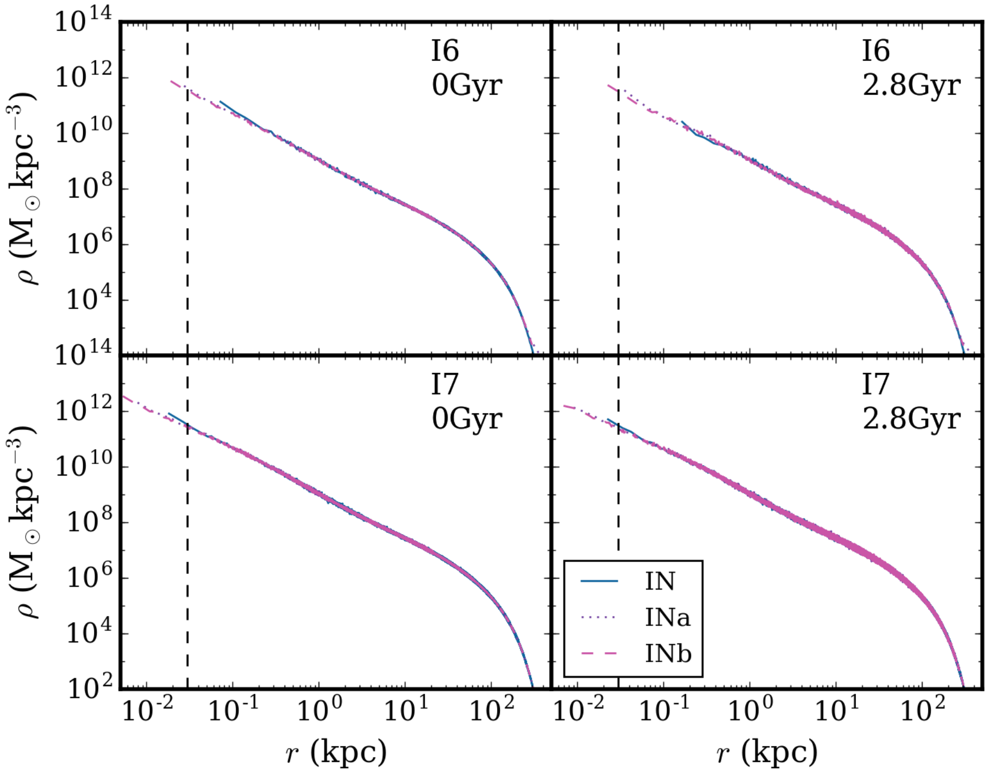

Figure 3.3: Spatial density profiles of the isolated models with $N = 10^6$ particles (top panels) and $N = 10^7$ particles (bottom panels) at time $t = 0.0\,\mathrm{Gyr}$ (left) and at the later time $t = 2.8\,\mathrm{Gyr}$ (right). The dashed vertical line represents the star-star softening length. The profiles show the same trends as the bulge particle distributions, with all the multi-resolution models showing stability at the innermost radii.

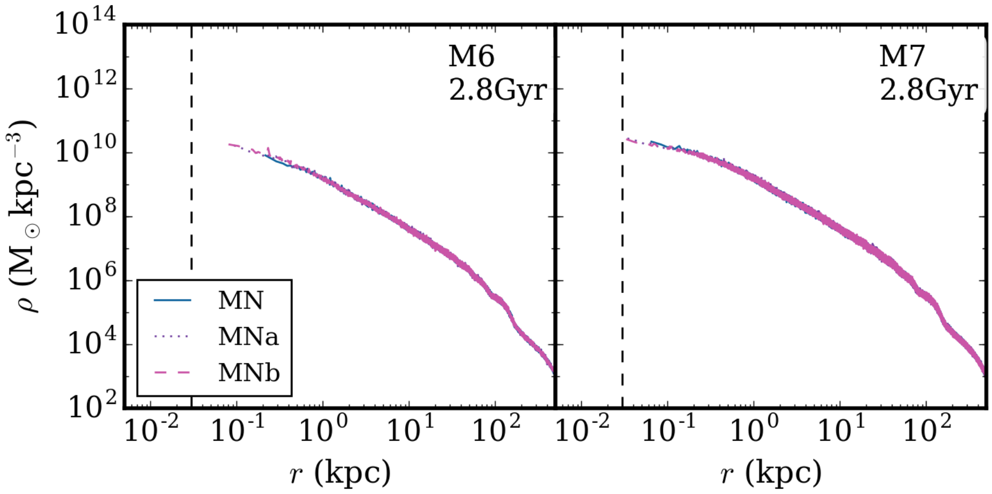

Figure 3.4: Spatial density profiles of the merger models with $N = 10^6$ particles (left) and $N = 10^7$ (right) at the later time $t = 2.8\,\mathrm{Gyr}$. The dashed vertical line represents the star-star softening length.

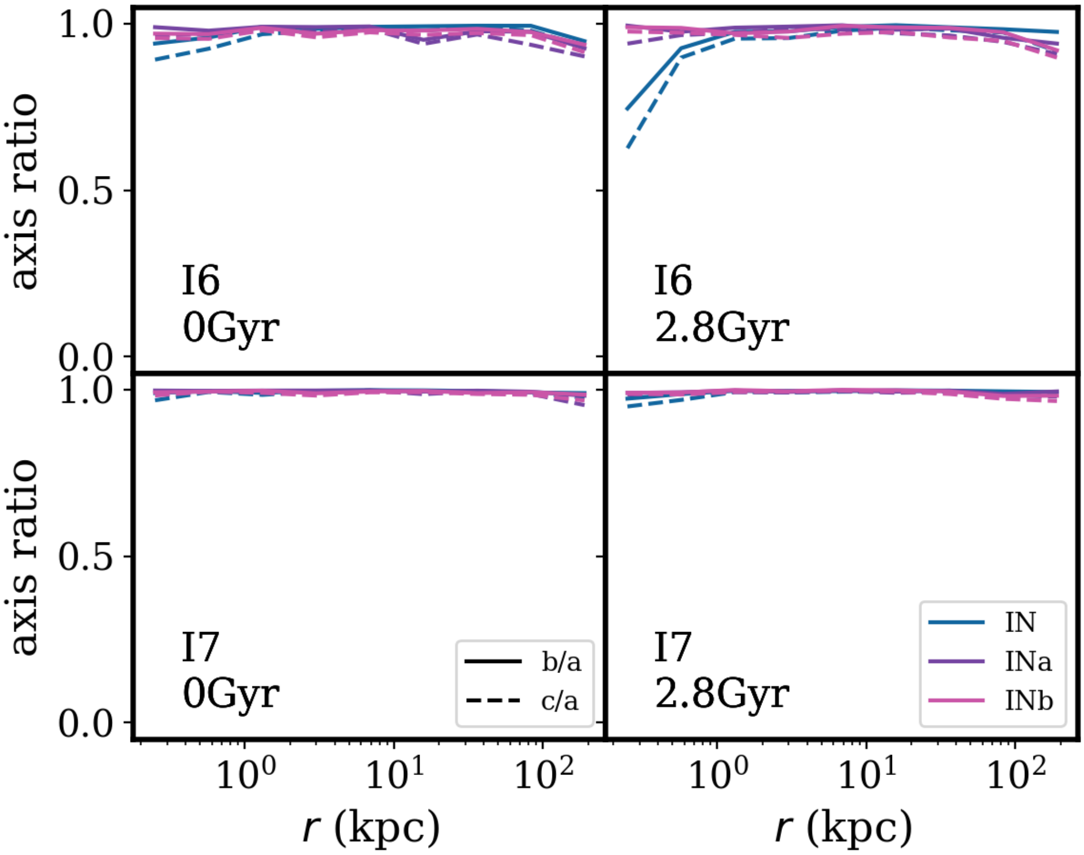

Figure 3.5: Axis ratios of the isolated models calculated as a function of radius with $N = 10^6$ particles (top panels) and $N = 10^7$ particles (bottom panels) at time $t = 0.0\,\mathrm{Gyr}$ (left) and at the later time $t = 2.8\,\mathrm{Gyr}$ (right). The solid lines show the evolution with radius of b/a, and the dashed lines the evolution of c/a, with each of the models maintaining sphericity across their evolution.

The results presented in Figures 3.3 and 3.4 are also in agreement with expectations based on a simple calculation of the dynamical friction timescale for point mass particles. A particle of mass M in a system of lighter particles will sink from a radius r_i on a timescale given by Chandrasekhar's dynamical friction formula (Binney & Tremaine, 2008)

$$T_{\mathrm{df}} = \frac{19\,\mathrm{Gyr}}{5.8} \frac{\sigma}{200\,\mathrm{km\,s^{-1}}} \left(\frac{r_i}{5\,\mathrm{kpc}}\right)^2 \frac{10^8\,\mathrm{M_\odot}}{M} \tag{3.5}$$

where σ is the local stellar velocity dispersion.

The timescale T_{df} of the halo particles is plotted in Fig. 3.13 for both the isolated and merger models as a function of radial distance. The chosen radial positions correspond to the centres of the scheme zones. The horizontal line indicates the total simulation time of 8 Gyr for the isolated models, and 4 Gyr for the merger models. Halo particles in the I6 models are affected by dynamical friction against the sea of bulge particles at distances of $r \lesssim 2\,\mathrm{kpc}$, while the multi-resolution models I6a and I6b are only affected within $r \lesssim 1\,\mathrm{kpc}$. At higher resolution, sinking is expected in model I7 only for particles within the central $\lesssim 500\,\mathrm{pc}$, which is reduced to the central $\lesssim 200\,\mathrm{pc}$ in the multi-resolution models I7a and I7b. It should be noted that the multi-resolution models experience a downturn in

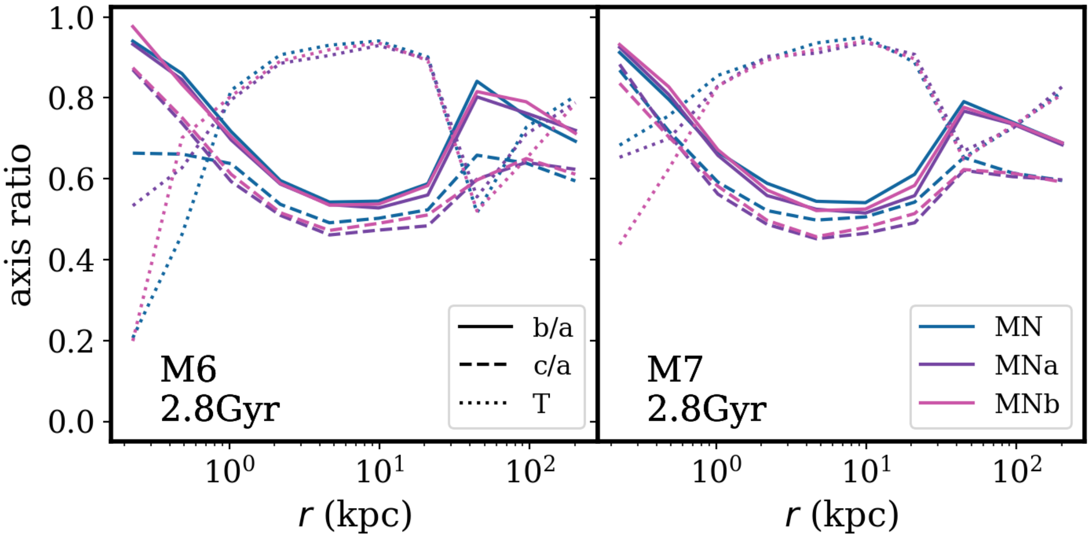

Figure 3.6: Axis ratios of the merger models calculated as a function of radius with $N = 10^6$ particles (left) and $N = 10^7$ particles (right) at the later time $t = 2.8\,\mathrm{Gyr}$. The solid lines show the evolution with radius of b/a, and the dashed lines the evolution of c/a.

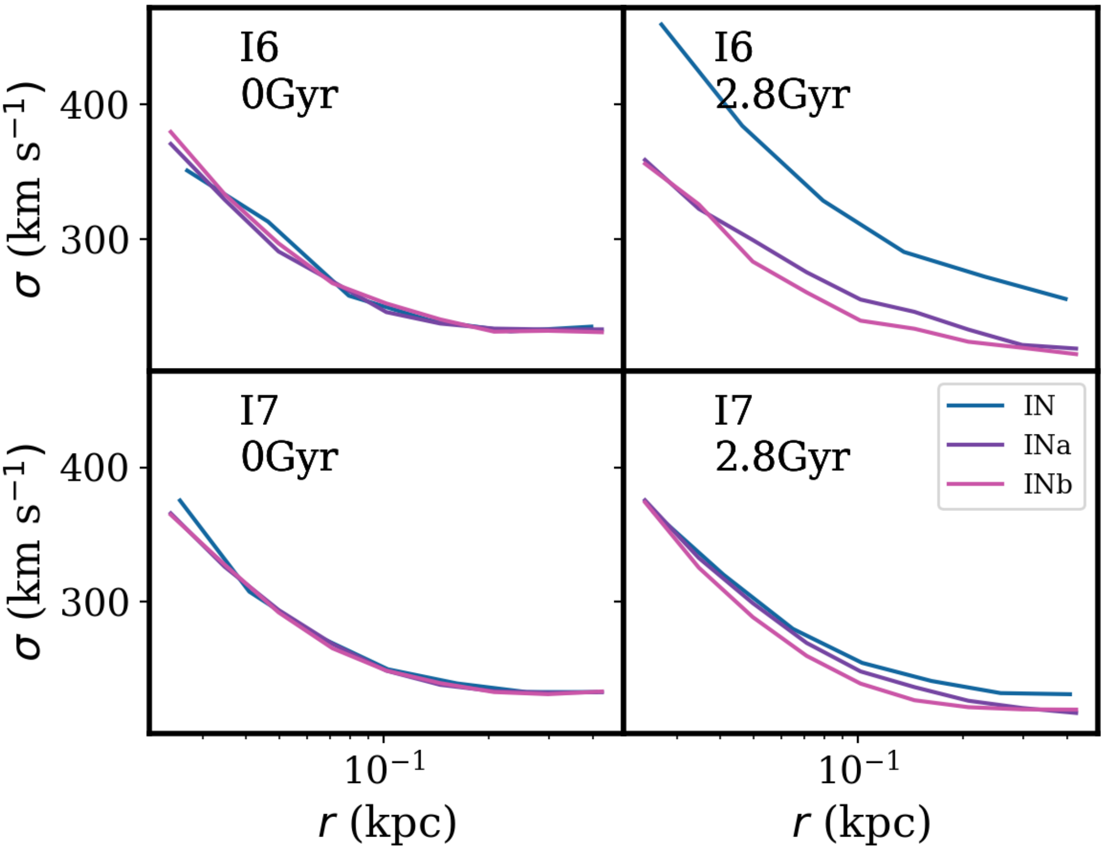

Figure 3.7: 3D stellar velocity dispersion profiles of the isolated models with $N = 10^6$ particles (top panels) and $N = 10^7$ particles (bottom panels) at time $t = 0.0\,\mathrm{Gyr}$ (left) and at the later time $t = 2.8\,\mathrm{Gyr}$ (right).

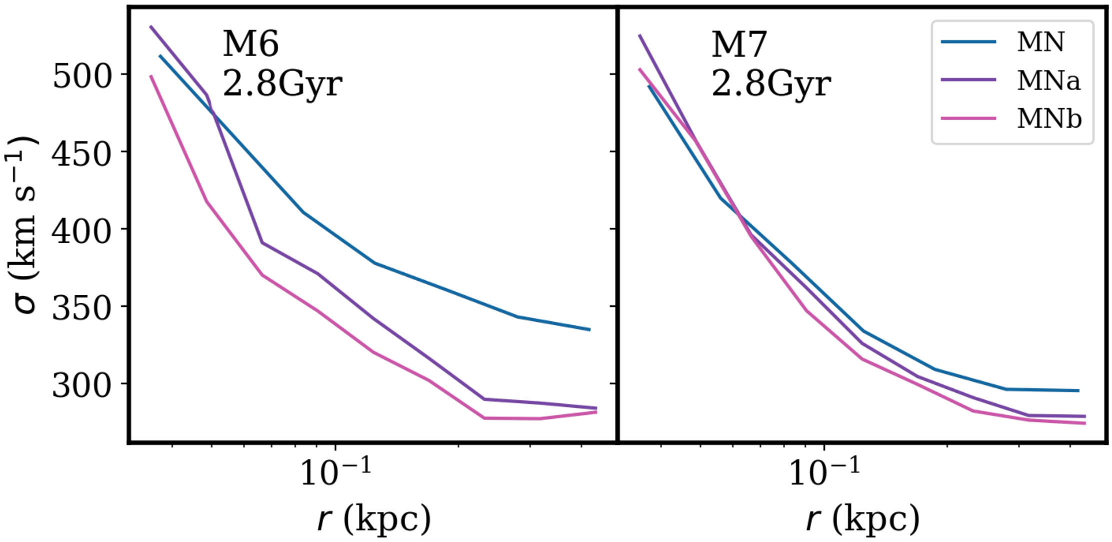

Figure 3.8: 3D stellar velocity dispersion profiles of the isolated models with $N = 10^6$ particles (left) and $N = 10^7$ particles (right) at the later time $t = 2.8\,\mathrm{Gyr}$.

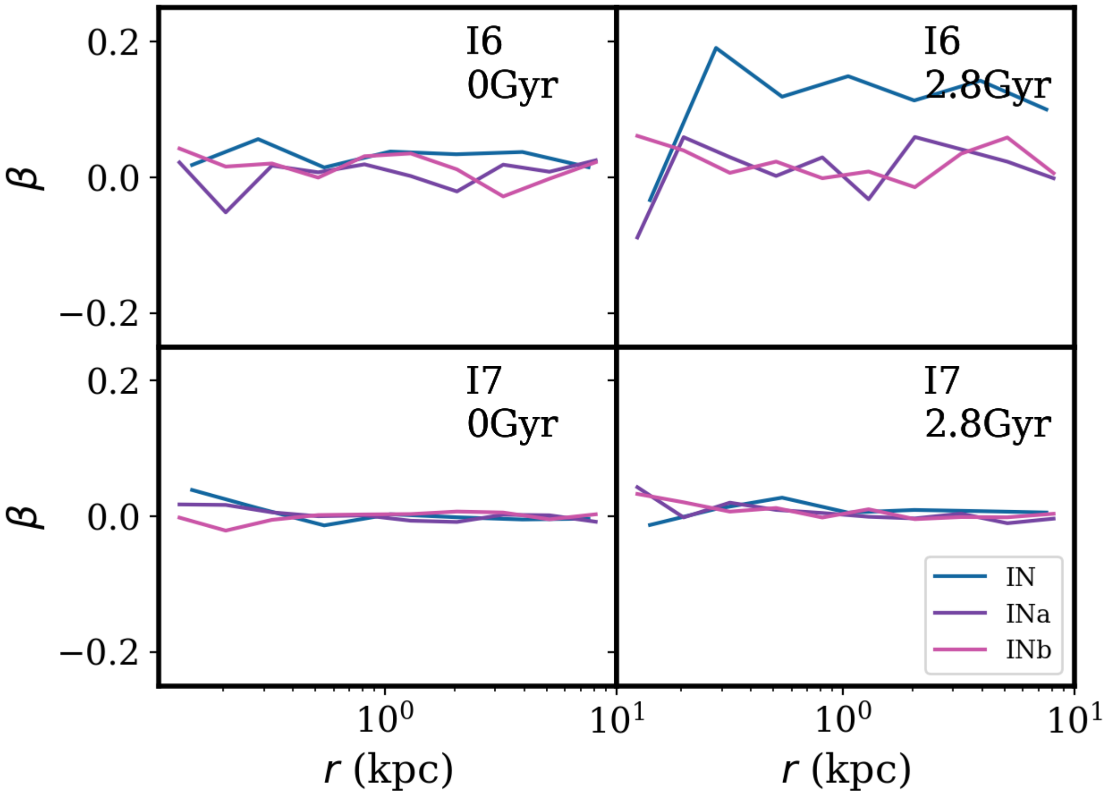

Figure 3.9: The velocity anisotropy profile of the isolated models with $N = 10^6$ particles (top panels) and $N = 10^7$ particles (bottom panels) at time $t = 0.0\,\mathrm{Gyr}$ (left) and at later time $t = 2.8\,\mathrm{Gyr}$ (right). Each of the models maintains $\beta(r) \simeq 0$ across the time evolution, bar I6.

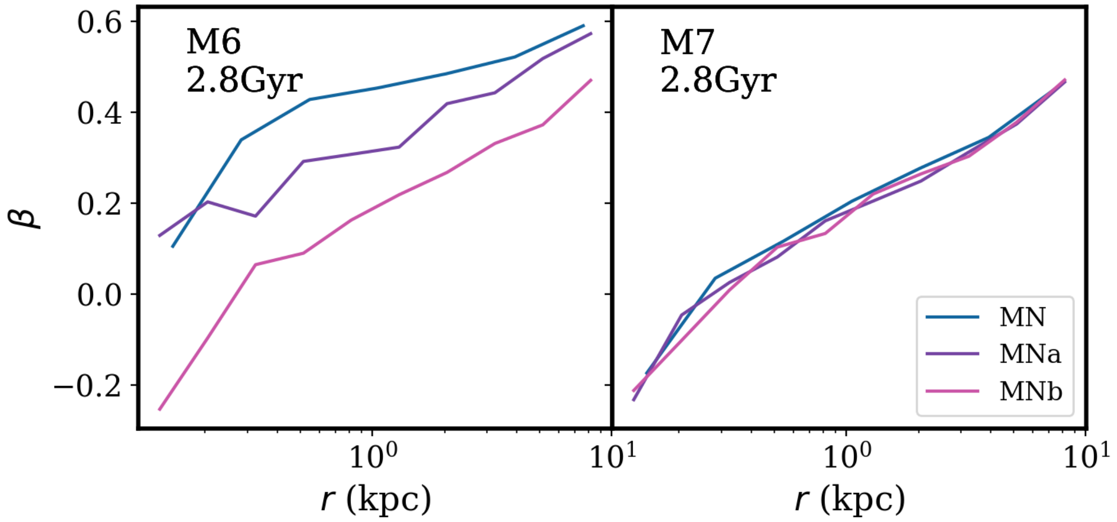

Figure 3.10: The velocity anisotropy profile of the merger models with $N = 10^6$ particles (left) and $N = 10^7$ particles (right) at later time $t = 2.8\,$Gyr.

the calculated $T_{\rm df}$ at large radii $r \gtrsim 10\,$kpc, owing to the increase in particle masses introduced by the schemes to compensate for the reduced particle number. Even so, the schemes appear beneficial out to $\sim 40\,$kpc. The merger models exhibit a very similar behaviour to the isolated models. The lack of mass segregation predicted by Fig. 3.13 is consistent with the results of (Alexander & Hopman, 2009) for the mass factors of order 10 utilised in both schemes.

3.5 Conclusions

In this chapter, I have presented a multi-resolution refinement scheme to improve resolution at the centres of multi-component galaxy models, without impacting their stability and dynamical evolution. The initial model is over-seeded by a set amount, with both halo and bulge particles divided into radial zones. The defined central zone remains unchanged at the higher resolution produced by the over-seeding, whilst in the other radial zones we remove particles and correspondingly increase the masses of the remaining particles to compensate. In this way, the resulting galaxy model has a higher central resolution, necessary to accurately model MBH dynamics, at the same particle number, total stellar mass, and mass density profile.

I introduced two schemes with varying degrees of over-seeding, the standard model ‘a’ and the more aggressive model ‘b’, with ‘b’ models increasing the number of radial zones by 1 to compensate for the increased particle masses at outer radii. These implementations are applied to a set of isolated and merging multi-component galaxy models, each comprised of a dark matter halo, a stellar bulge, and a central MBH. I evolved a set of isolated and equal-mass merger models using the FMM code GRIFFIN, at the reference resolutions of $N = 10^6$ and $N = 10^7$.

The isolated models show that the multi-resolution schemes are effective at increasing resolution in the central regions, and this is maintained over time. Both schemes are also effective at reducing the relaxation-driven expansion of the bulge particles observed in the lower resolution models, and expansion is nearly eliminated in the M6b implementation. I show that the introduction of mass refinement does not affect the stability of the models

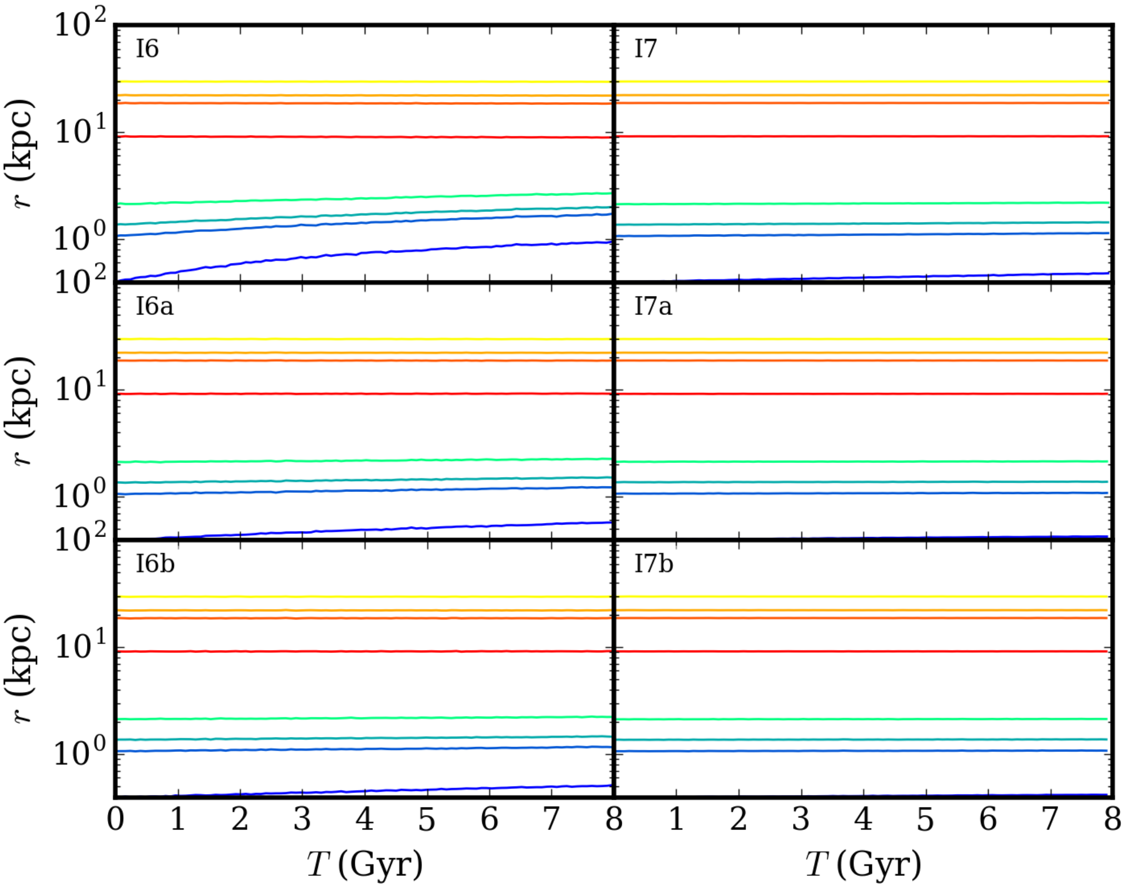

Figure 3.11: Lagrangian radii for bulge (bottom four curves) and halo (top four curves) particles for all isolated models with $N = 10^6$ (left) and $N = 10^7$ (right) across the simulation time. The curves correspond to radii containing mass fractions of 3%, 10%, 13%, and 20% of the total bulge mass. I6 shows a significant expansion at the lowest bulge radius, which is notably reduced in the multi-resolution models. The halo particles remain stable in all models.

nor the subsequent evolution.

With the key result that both the ‘a’ and ‘b’ refinement schemes are effective at increasing central resolution, reducing spurious relaxation and stochastic effects, I conclude that schemes of the type described in this work are extremely effective at increasing resolution in the central regions. For the next stage of analysis, I examine how this affects the MBH binary properties and hence the resulting merger timescales in the following chapter.

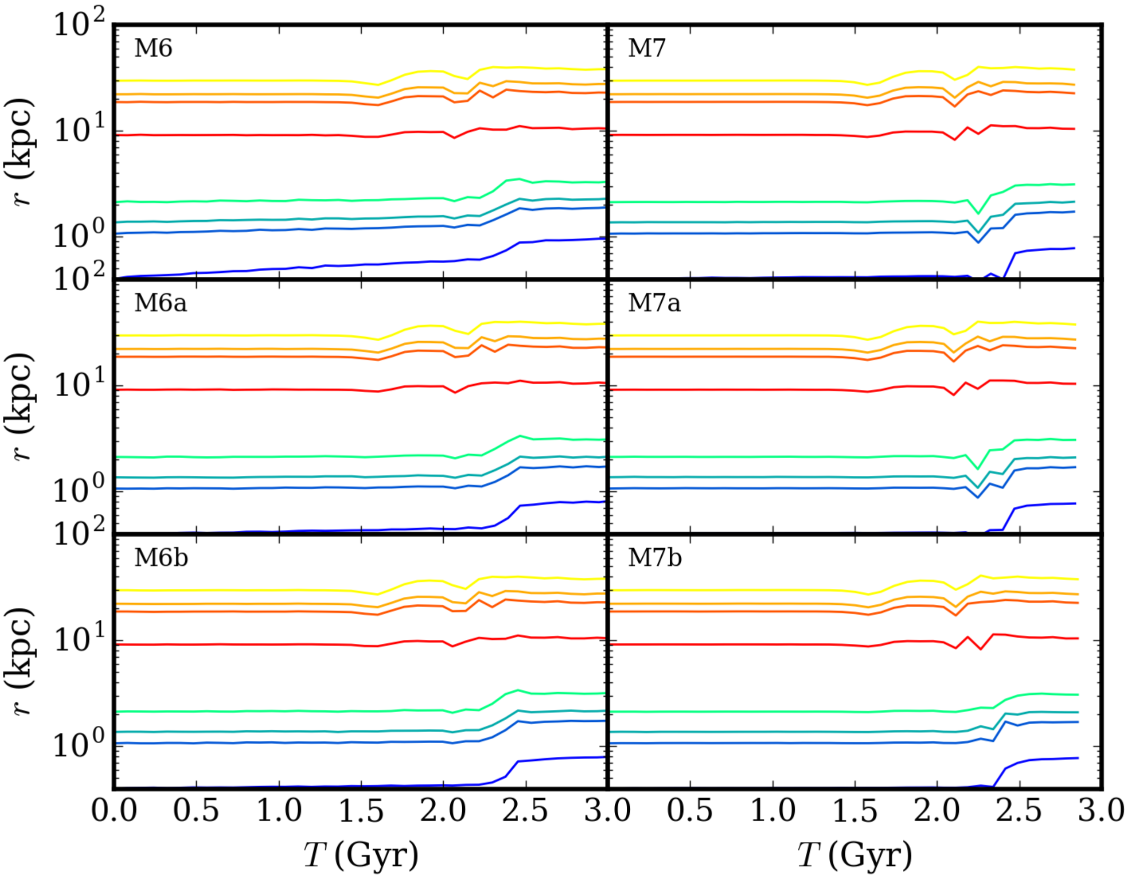

Figure 3.12: Lagrangian radii for bulge (bottom four curves) and halo (top four curves) particles for all merger models with $N = 10^6$ (left) and $N = 10^7$ (right) across the simulation time. The curves correspond to radii containing mass fractions of 3%, 10%, 13%, and 20% of the total bulge mass. The strong disturbance at $t \sim 2.5\,\mathrm{Gyr}$ marks the completion of the merger process. The M6 model shows a significant expansion at the smallest radii, similarly to I6.

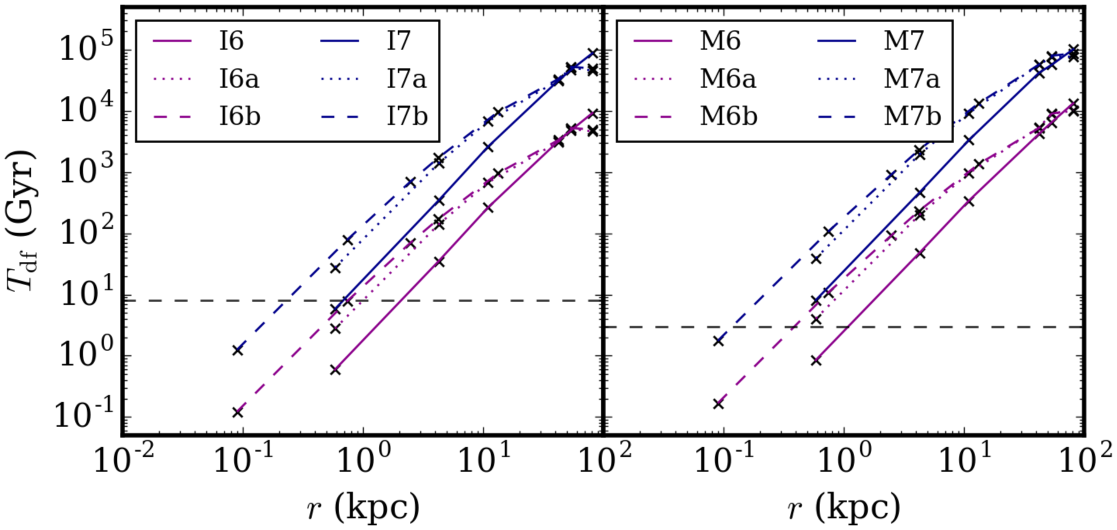

Figure 3.13: Dynamical friction timescale of the halo particles for all models at time $t = 2.8\,$Gyr, for the isolated models (left) and the post-merger models (right). The dashed horizontal lines mark the duration of the simulations (black). The points mark the centres of each radial bin in the multi-resolution schemes. The particles are affected by dynamical friction at $r \lesssim 2\,$kpc in I6, and at $r \lesssim 1\,$kpc in the multi-resolution models. In model I7, dynamical friction only affects particles within the central $\lesssim 500\,$pc, which is reduced to the central $\lesssim 200\,$pc in the multi-resolution models. The multi-resolution models show a downturn in $T_{\rm df}$ at the outer radii, where the particle masses are most increased. The merger models show similar trends to the isolated models.

MBH Binary Timescales with the Multi-Resolution Scheme

4.1 Introduction

In this chapter I present the results of the MBH binary evolution from both the multi-resolution models and the reference resolutions. The three major phases of binary evolution begin with dynamical friction as the MBHs sink to centre of the galaxy merger remnant, and form a bound pair. The binary then hardens due to three-body interactions with stars during the rapid gravitational slingshot phase (Quinlan, 1996; Sesana et al., 2008a; Gualandris et al., 2017), until the binary separation is of order milliparsec or less and the emission of GWs commences. The final inspiral then proceeds quickly in the ensuing GW phase, and the MBHs coalesce. The dynamical friction and stellar scattering phases are followed with the FMM code GRIFFIN until the separation reaches the softening limit of the code, and the ensuing evolution is then followed by a semi-analytic prescription down to the emission of GWs and binary coalescence. With detection of the GWB expected shortly by PTA, the astrophysical interpretation of the results will be aided by accurate estimations of merging MBH timescales and hence the expected GW emissions from a representative sample of MBH binaries.

The multi-resolution scheme presented in Chapter 3 was shown to be effective at increasing the central resolution for merging galaxies without affecting the stability of the models. Here I examine the results of the central MBH binary orbital parameter evolution and the differences between the schemes and reference resolution. The initial conditions of the galaxy models were laid out in Sec. 3.3, from which I continue the analysis. The MBH mergers I follow here are equal-mass mergers, where the MBHs are each of a mass $M_{\mathrm{bh}} = 7.14 \times 10^8\,\mathrm{M}_\odot$, hence with GW emissions from their coalescence that would lie within the PTA frequency band (see Sec. 1.6.2). In this chapter I present the results from following the evolution of the embedded MBHs first with GRIFFIN, obtaining the binary orbital parameters, and then extrapolate the GRIFFIN evolution to coalescence with a semi-analytic prescription that considers three-body interactions and GW emission. I first describe this semi-analytic extension to the models and the projected merger times for each binary, and analyse the MBH binary evolution results for the applications of the scheme for agreement in the results.

The content of this chapter was adapted from a submission to Monthly Notices of the Royal Astronomical Society (MNRAS), as *A multi-resolution method for modelling galaxy and massive black hole mergers*, Attard, Gualandris, Read, and Dehnen.

4.2 Evolution of the Massive Black Hole Binaries

The evolution of the MBHs is followed with GRIFFIN through the dynamical friction phase, the formation of a bound binary and into the collisionless losscone refilling phase. Once the binary separations passed the black hole softening limit, I then employed a semi-analytical prescription to extend the evolution down to coalescence including the final GW emission phase, and compute the merger timescale for each of the different models. I examine the

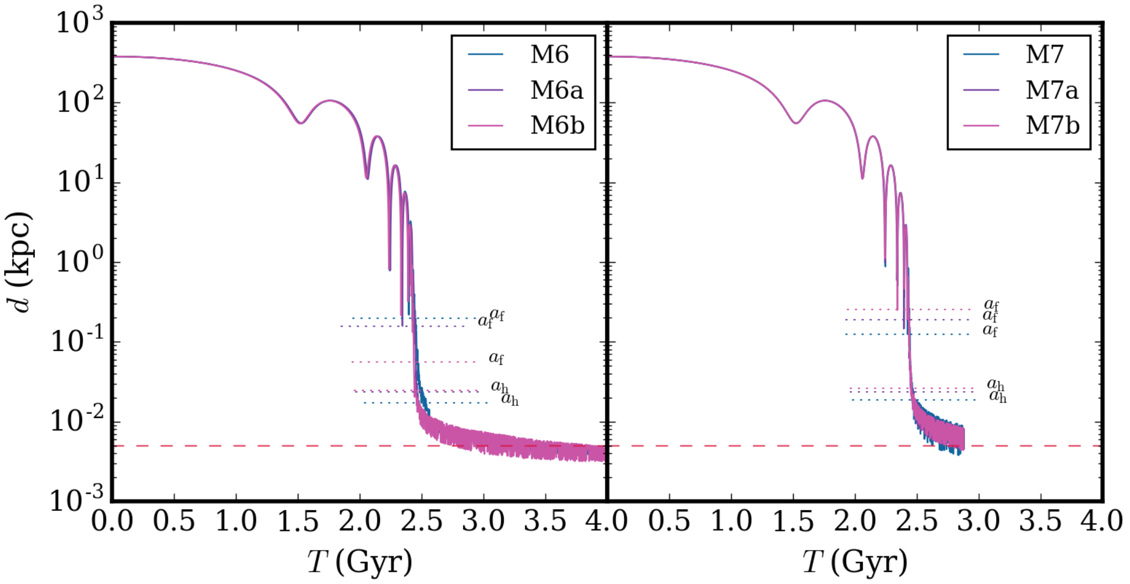

Figure 4.1: The evolution of the separation between the MBHs in the $N = 10^6$ models (left) and $N = 10^7$ models (right). The three characteristic phases of binary evolution are visible in all models, marked by the critical separations a_f and a_h. All models consistently reproduce the evolution of d over time. The dashed line shows the softening length for the BH-BH and BH-particle interactions (red). The dotted lines mark the critical separations of the binary, a_f, approximately where the dynamical friction phase ends, and a_h, the hard binary separation.

effect of resolution and the multi-resolution schemes on the orbital elements of the binary as well as the coalescence timescale.

The three characteristic phases of binary evolution can clearly be seen in Figure 4.1, which shows the distance between the MBHs as a function of time. The galaxies first evolve under the effects of dynamical friction, which brings them together during the merger and, at the same time, causes the MBHs to sink to the centre of the merger remnant, where they form a pair and eventually a bound binary. At the end of this phase, the MBHs are approximately at a separation a_f, where the enclosed stellar mass is equal to twice the mass of the secondary MBH, as defined in Eqn. 1.12.

Three-body interactions between the binary and background stars become increasingly important towards the end of this phase until they dominate the evolution, as the influence of dynamical friction wanes once the binary begins to reach thermal equilibrium with surrounding stars (Antonini & Merritt, 2012; Kelley et al., 2017). Such interactions are known as slingshot interactions as the stars remove energy and angular momentum from the binary, and are ejected to large distances. As a consequence, the MBHs spiral closer together (Begelman et al., 1980; Merritt, 2013) until all stars initially belonging to the losscone are ejected; this occurs roughly at the hard-binary separation a_h, which is of order a parsec for black holes of $M \sim 10^8\,\mathrm{M}_\odot$. There are different definitions of the hard-binary separation in the literature, here I adopt the formal Eqn. 1.20 given by the separation where the relative velocity of the binary surpasses the velocity dispersion of local stars.

Beyond a_h, binary hardening relies on collisionless repopulation of the losscone, until GW emission becomes important (at roughly milliparsec scales) and drives the MBHs to coalescence.

The numerical simulations are terminated once the separation between the MBHs has reached the BH softening length at $\epsilon_{BH} = 5\,\mathrm{pc}$, which was set to be smaller than a_h to ensure that the evolution is followed self-consistently well into the losscone refilling phase.

4.2.1 Binary Coalescence Times

Figure 4.1 shows that all models reproduce the same evolution for the separation between the MBHs all the way down to the BH softening length; the same is not true for the evolution of the semi-major axis and eccentricity of the binary. Figure 4.2 shows the semi-major axis and eccentricity evolution for each of the models, calculated at the apocentre of the orbit. Models M6a and M6b show the same evolution of semi-major axis as model M7, indicating that the mass schemes are effective and allow to reach convergence in semi-major axis at the modest resolution of $N = 10^6$. Model M6, on the other hand, shows a significant deviation from both M6a/b and M7 and cannot be relied upon. Reaching convergence in the binary eccentricity is harder, as may be expected. There is significant scatter in eccentricity in all M6 models, including the mass refined models, though M6b achieves a very similar behaviour to M7. At the highest resolution, however, M7 shows a considerable difference in eccentricity with respect to models M7a/b, implying that mass refinement at $N = 10^7$ is required to reach convergence in eccentricity. Because the coalescence timescale of MBH binaries due to GW emission is strongly dependent on the orbital elements, and in particular on the eccentricity, it is expected that these results will affect the time to coalescence.

Figure 4.3 shows a measure of the convergence in the eccentricity, by taking the highest resolution simulation run M7b as the 'true' value for the eccentricity and calculating the difference between the different resolutions as $(e - e_\mathrm{true})/e_\mathrm{true}$. I calculate the difference at $t = 2.8\,\mathrm{Gyr}$ and take an average of the eccentricity values within $\pm 50\,\mathrm{Myr}$, to reduce the effect of noise. It can be seen that as the resolution increases the simulations tend towards convergence, even considering the effect of stochasticity in the eccentricity.

The late evolution of the binaries was followed with a semi-analytical model that solves the coupled differential equations for the orbital elements under the effects of both stellar hardening and GW emission (Gualandris et al., 2022)

$$\frac{da}{dt} = \left.\frac{da}{dt}\right|_* + \left.\frac{da}{dt}\right|_{GW} \tag{4.1}$$

$$\frac{de}{dt} = \left.\frac{de}{dt}\right|_* + \left.\frac{de}{dt}\right|_{GW} \tag{4.2}$$

where the first term represents the contribution from three-body stellar interactions and the second term models GW emission. The stellar hardening rate is described by (Gualandris et al., 2022)

$$\left.\frac{da}{dt}\right|_* = -s(t)a^2 \tag{4.3}$$

where the time-dependant hardening rate $s(t)$ is defined as

$$s(t) = \frac{d}{dt}\left(\frac{1}{a}\right) \ . \tag{4.4}$$

The contribution to the eccentricity evolution from three-body stellar interactions is

$$\left.\frac{de}{dt}\right|_* = s(t)Ka \ , \tag{4.5}$$

and the dimensionless eccentricity growth rate K is defined as (Quinlan, 1996)

$$K = \frac{de}{d\ln(1/a)} \ . \tag{4.6}$$

The contribution from GW emission can then be calculated according to Equations 1.21 and 1.22 (Peters, 1964). Combining this with the the equations for stellar hardening, it can be seen that GWs will take over as the dominant hardening mode much faster as the eccentricity climbs to higher values.

The time-dependent numerical hardening rate in the hardening phase as simulated with GRIFFIN is computed and an exponential decay is fit to the data over time, as shown in Fig. 4.4. The eccentricity growth rate is approximately constant over the simulated hardening phase and I then adopt its average for all models, as shown in Fig. 4.5, to be used in Equations 1.16 and 1.19, together with the fitted hardening rate.

I begin the semi-analytical integration from time 2.75 Gyr for the M6 models and from time 2.7 Gyr for the M7 models, and continue until coalescence. I take an average of the semi-major axis and eccentricity values within ±50 Myr of the starting value, to reduce noise. The resulting evolution of the binary orbital elements is shown in Fig. 4.6 for each model. The predicted trajectories are shown by the dashed lines for each model, and are consistent with the prior evolution from the GRIFFIN integrations. It should be noted that stochasticity in the N-body evolution significantly affects the extrapolations to late times, as both three-body encounters and GW emission depend strongly on the semi-major axis and, especially, the eccentricity. High resolution and/or the implementation of the multi-resolution schemes are hence required to reduce the spread in the orbital elements.

Table 4.1 gives the time taken for each model to reach the binary critical separations from the start of the N-body integration, alongside the merger timescales obtained from the semi-analytical extrapolations. The merger timescales are determined as the time from the simulation start for either the eccentricity or the semi-major axis to reach 0. In general, the high resolution models give shorter timescales, all under 8 Gyr, a desirable result in terms of detection rates for PTA. The longest timescale is obtained in model M6, at 12 Gyr. At low resolution, model M6b gives the closest result to the $N = 10^7$ models. Because of the strong dependence of the merger timescale on initial binary eccentricity, convergence in the total timescale is not achieved even in models M7a/b, where the coalescence times are within ~ 1 Gyr of each other, and would require even higher resolution and/or more random realisations to verify.

4.3 Conclusions

In this chapter, I have presented the MBH binary timescales for equal mass binaries embedded in galaxy models generated using the multi-resolution scheme described in Chapter 3. Binary formation occurs at ~ 2.5 Gyr for all models. However, while all models are able to reproduce the same behaviour for the separation between the MBHs over time, the orbital elements are sensitive to the resolution. In particular, model M6 shows incongruous behaviour in the semi-major axis compared to mass refined or higher resolution models. Models M6a and M6b are roughly consistent, with M6b behaving similarly to M7. This implies that convergence in the semi-major axis evolution is reached at particle number $N = 10^6$ if a multi-resolution scheme is applied.

The binary eccentricity, however, shows more variation than the semi-major axis, as it is more sensitive to perturbations and low-N effects. A significant scatter is present at the lowest resolution of $N = 10^6$ and some variation still exists at the highest resolution

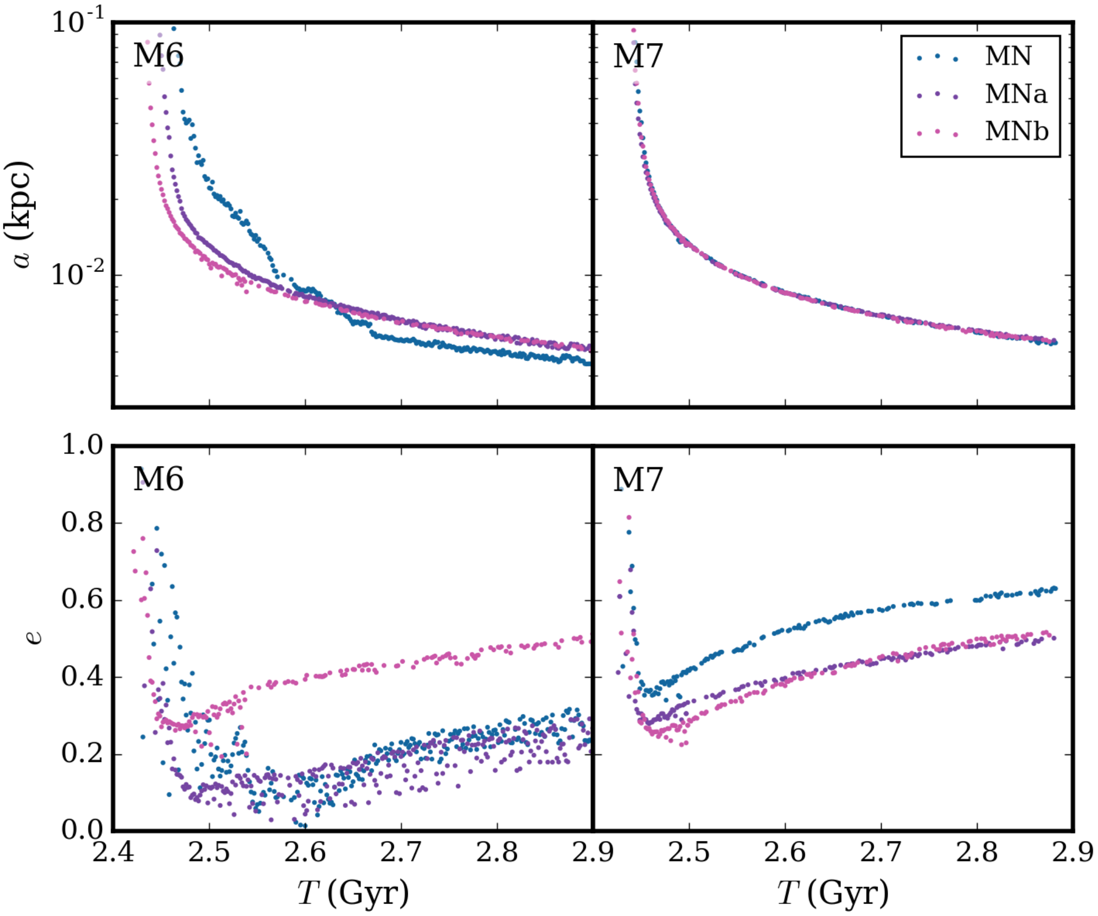

Figure 4.2: The evolution of the semi-major axis a (top) and the eccentricity e (bottom) of the MBH binary with time, computed from the GRIFFIN simulations, at the lower (left) and higher (right) resolution. The evolution of the semi-major axis in the multi-resolution models M6a and M6b is consistent with that in the M7 models, while that in model M6 is markedly different. This shows that the mass-schemes lead to convergence at 10^6 particle resolution, with regard to the semi-major axis. The evolution of the eccentricity, however, is characterised by a large scatter in models M6 and M6a, while M6b shows a smaller scatter as well as a behaviour very similar to model M7. Convergence in eccentricity is challenging to achieve, and barely obtained in models M7a and M7b, implying that a combination of $N = 10^7$ resolution and a mass-refinement scheme is required.

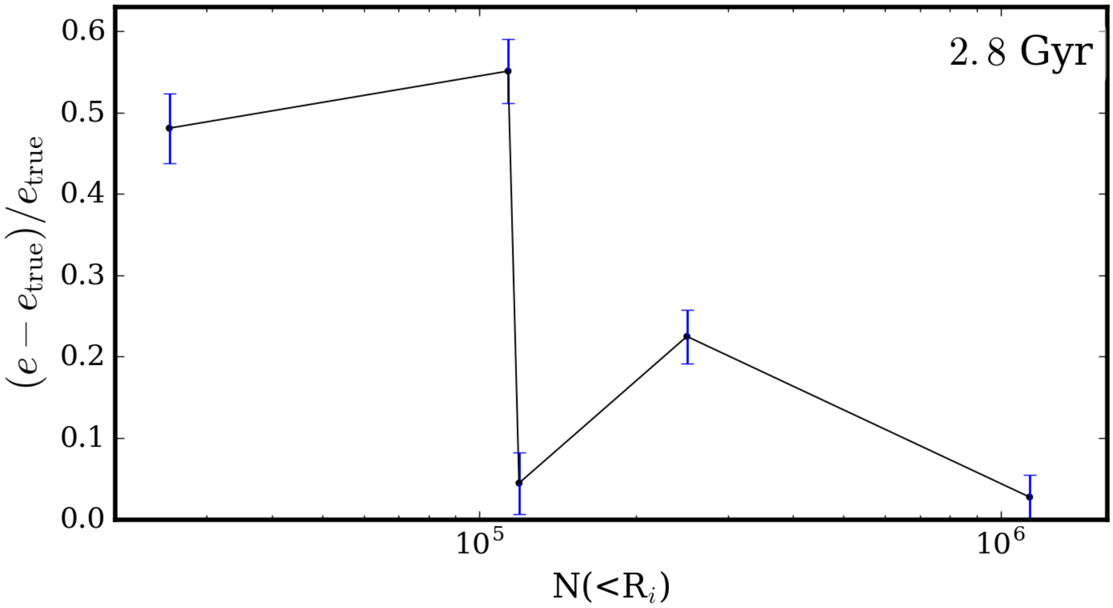

Figure 4.3: The difference between the binary eccentricities, taking the highest resolution M7b run as 'true', at time $t = 2.8\,\mathrm{Gyr}$. The models approach convergence as the resolution increases, with M6b, M7, and M7b all significantly improved over M6 and M6b. Errorbars are determined using eccentricity dispersions from Fig. 8 in Nasim et al. (2020).

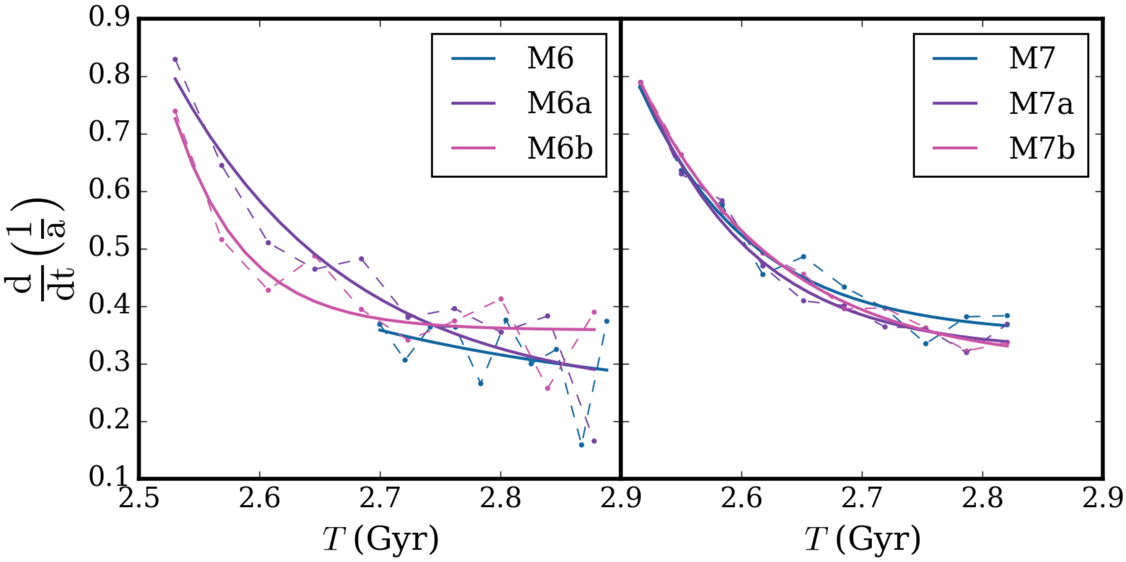

Figure 4.4: Evolution of the hardening rate, computed numerically as in Eq. 1.17, at the lower (left) and higher (right) resolution (points/dashed lines). The solid lines indicate exponential fits over time.

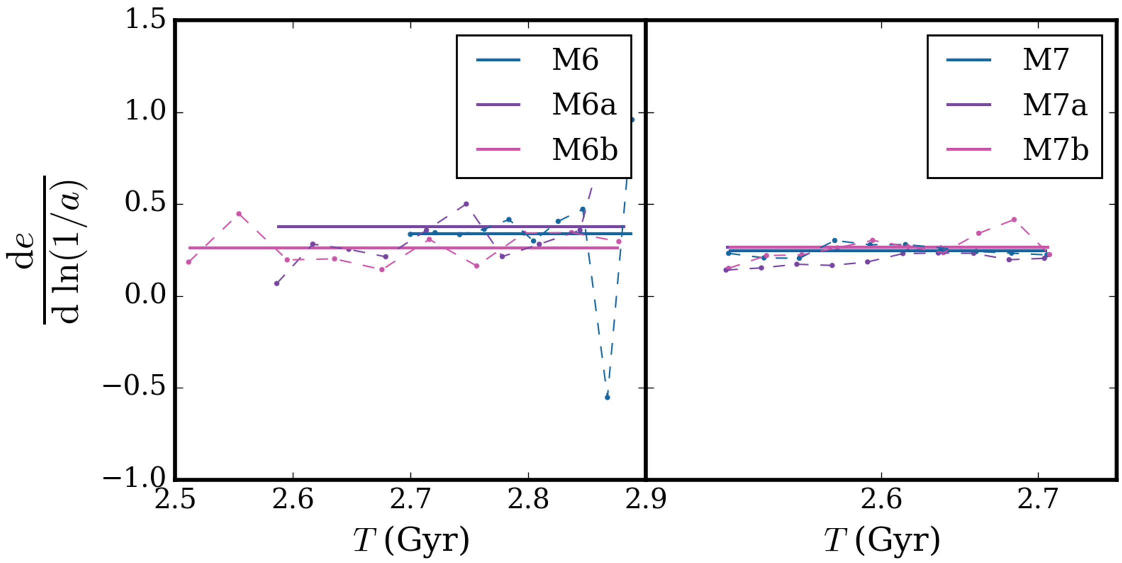

Figure 4.5: Evolution of the eccentricity growth rate, computed numerically as in Eq. 1.18, at the lower (left) and higher (right) resolution (points/dashed lines). The solid lines indicate the calculated mean value.

of $N = 10^7$. The aggressive scheme applied in M6b results in the most similar behaviour to the M7 models.

I have computed the time to coalescence for the MBH binaries in all models by extending the N-body simulations with a semi-analytical calculation of the evolution of the orbital elements under the combined effects of stellar hardening and GW emission. The time-dependent hardening rate is determined directly from the N-body integrations, and its exponential fit is used within the model. I find that merger timescales can vary by a few Gyrs in the M6 models, and are generally longer than in the M7 models. Model M6b, with the most aggressive scheme, gives the most similar evolution and merger timescale to the higher resolution models. By contrast, the $N = 10^7$ models show a much smaller spread in predictions, with models M7a and M7b coming within 1 Gyr of each other.

Variations in merger timescales have also been reported in Gualandris et al. (2022) at particle numbers of order $N = 10^6$, while Nasim et al. (2021) show that a resolution

Table 4.1: Characteristic timescales for the binaries throughout the evolution. From left to right: the simulation identifier, the time to a_f (an estimate of the time spent in the dynamical friction phase), the time until the binary reaches the hard binary separation a_h, the time from end of the numerical integration to coalescence (including stellar hardening and the GW emission phase), and the total time from the start of the simulation to BHB merger.

Scheme	$T_{\rm f}$ (Gyr)	$T_{\rm h}$ (Gyr)	$T_{\rm merg}$ (Gyr)	$T_{\rm tot}$ (Gyr)
M6	2.44	2.53	9.25	12.00
M6a	2.35	2.47	6.91	9.66
M6b	2.44	2.45	4.58	7.33
M7	2.43	2.47	2.94	5.64
M7a	2.42	2.46	4.62	7.32
M7b	2.43	2.46	4.90	7.60

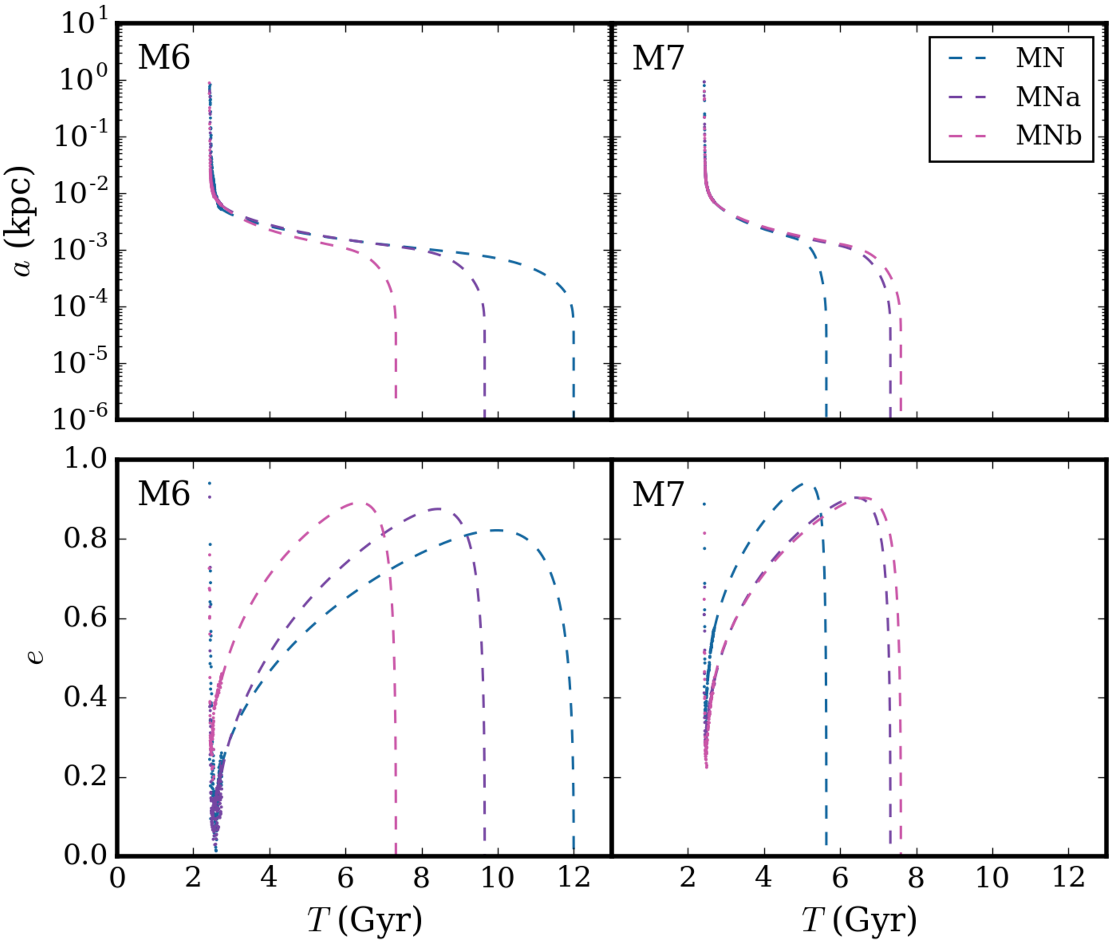

Figure 4.6: The evolution of the semi-major axis a (top) and the eccentricity e (bottom) of the binary with time, from the beginning of the merger to coalescence. The evolution simulated with GRIFFIN is shown with scatter points, whilst the subsequent evolution modelled by a semi-analytic model including GWs is shown by dashed lines. The $N = 10^6$ models show longer merger timescales than the $N = 10^7$ models, though the most aggressive scheme M6b gives the closest result to M7. Convergence in the merger timescales is hard to achieve. We require multi-resolution models at $N = 10^7$ (M7a/b) for the difference in total timescales to fall below 1 Gyr.

in excess of $N = 10^7$ within the half-light radius is required to reduce the scatter in the merger timescale to $\sim 10\%$. I calculate that this corresponds to about $N = 4 \times 10^6$ particles within $5\,R_{\rm infl}$, which is a factor 3 larger than what we achieve in models M7a/b. Taking the results of Nasim et al. (2021) at face value, this implies that the effective resolution in models M7a/b results in a $20 - 30\%$ error in the predicted merger timescale. In order to achieve a 10% error, a combination of $N(< 5R_{\rm infl}) = 4 \times 10^6$ and mass refinement is required. For the multi-component models as presented here, which are designed to represent the massive galaxies which are hosts to typical PTA sources, this corresponds to a total particle number of $N = 3 \times 10^7$.

I conclude that the increased resolution at the galaxy centres provided by the multi-resolution scheme should be combined with an appropriate particle number to reduce scatter in key quantities: a particle number of $N(< 5R_{\rm infl}) = 6 \times 10^4$ is sufficient (e.g. model M6b) to reach convergence in the evolution of the semi-major axis, while a particle number of $N(< 5R_{\rm infl}) = 10^6$ is required to approach convergence in the evolution of the eccentricity and in the time to coalescence. In order to achieve a 10% error on the merger timescale, a resolution $N(< 5R_{\rm infl}) = 4 \times 10^6$ is required. This is due to the strong dependence of both stellar hardening and GW emission on eccentricity.

Finally, it should be noted that the galaxies examined here are all set on initial orbits of $e = 0.7$, i.e. moderately eccentric. Gualandris et al. (2022) have shown that binaries with lower eccentricities exhibit a greater spread in merger timescales. It is therefore expected that somewhat lower variations would be present for highly eccentric orbits (e.g. Nasim et al., 2020, 2021; Mannerkoski et al., 2022).

Subsequent Galaxy Mergers with the Multi-Resolution Scheme

5.1 Introduction

Successive galaxy mergers are expected to occur in the hierarchical structure formation scenario of the ΛCDM paradigm, bringing a new MBH into a galaxy directly after a prior MBH binary has formed, but potentially before the final inspiral has taken place. Mergers of dark matter halos were more common in the early Universe as they clustered under the effect of gravity in the denser environment, as such creating a heightened potential for MBH binaries to form (Begelman et al., 1980; eLISA Consortium, 2013). For an MBH brought in by such a merger intruding on a galaxy that has recently hosted another central MBH binary, the core scouring effects inflicted on the galaxy by the previous binary formation may have effects on the subsequent evolution of the new binary as the depletion of stellar density means there may be fewer stars within the losscone. As such, the three-body interaction phase may not proceed as quickly as prior or the binary could potentially stall (Bonetti et al., 2016). If the lifetime of the previous MBH binary is long enough that it overlaps with a subsequent galaxy merger, triple interactions can also occur between the intruder and the original binary MBH. Triplets MBH systems have been observed in the Universe, indicating this could be a relatively common scenario (e.g. Schawinski et al., 2011; Deane et al., 2014; Liu et al., 2019).

Triple MBH interactions arising from subsequent galaxy mergers can form a hierarchical system, in which the centre of mass of the inner binary orbits with the intruder MBH in the outer binary (Bonetti et al., 2016). Kozai-Lidov (K-L) oscillations may be induced in such hierarchical triples, which take place when the orbit of the intruder MBH is inclined greater than some critical angle compared to the inner binary orbit (Kozai, 1962; Lidov, 1962; Naoz, 2016). This mechanism causes the inner binary eccentricity to secularly increase as it is excited to higher values in timescales greater than the orbital period of both the inner and outer binaries. The GW emission phase has a strong dependence on the eccentricity (as given in Eqns. 1.21-1.22), and as such the K-L oscillations can drive the inner binary to a faster coalescence (Blaes et al., 2002; Bonetti et al., 2016; Liu & Lai, 2017; Bonetti et al., 2018a).

An incoming MBH can also cause the ejection of one of the MBHs in a triple (e.g. Hoffman & Loeb, 2006; Lousto & Zlochower, 2008; Mannerkoski et al., 2021). An intruder MBH of sufficient mass may capture a member of the inner binary after sinking via dynamical friction within range of the original binary, and form a hierarchical triple with the intruder MBH on a wider outer orbit from the inner binary. Exchanges between the inner and outer binaries then become possible as the outer MBH decays close enough to enable strong interactions between the three MBHs. These strong three-body interactions can cause an ejection of one of the MBHs, with the lightest MBH in the triple typically experiencing the largest kick to a wide orbit. Intruders of larger mass and hence greater momentum are more likely to disturb the inner binary in this way. Multiple exchanges can also occur between the MBHs in the inner and outer binary as a result of these strong interactions, before an ejection or merger may take place (Hoffman & Loeb, 2007; Bonetti et al., 2018a; Mannerkoski et al., 2021, 2023).

The dynamics and evolution of MBH binaries under these circumstances hence need to be studied further in the context of the recent PTA evidence for a low-frequency signal to obtain the most accurate idea of merging MBH population, and hence provide interpretation of the signal in the GWB scenario (Bonetti et al., 2018b). To that end, following the formation and evolution of MBH binaries in the cosmological context of successive mergers is important. The results in previous chapters show mergers taking place over Gyrs from the galaxy merger, allowing time for another galaxy merger to occur and hence intrusion by a third MBH, as is expected in the early Universe for the hierarchical galaxy formation scenario.

In this chapter I follow the evolution of the equal-mass MBH binary examined from the previous chapters with the addition of a new incoming galaxy hosting an MBH. The subsequent interactions are followed for a set of models first assuming the prior binary had coalesced by the time of the next galaxy merger, and then if the merger had not yet completed. Two merger scenarios are considered, with differing intruder MBH masses based on the mass ratios between the intruder and the total original binary mass. I investigate if the core scouring resulting from the previous binary formation have an effect on the subsequent binary evolution and coalescence, and examine the resultant trajectories and triple evolutions in the case of three MBH interactions.

5.2 Model Set-Up

5.2.1 Initial Conditions

I continued the evolution of the previous galaxy merger by taking the remnant galaxy and contained MBH binary of model M6b, as described in Chapters 3-4. I chose M6b for the marked improvement in reducing particle expansion over the unrefined models, and the similarity to M7 at the central radii, but taking advantaged of the reduced computational time. I then set up two sets of models, distinguished by containing a higher and lower MBH mass ratio to the original galaxy, selected from subsequent mergers in the same merger tree of the IllustrisTNG-300-1 simulation as the original equal-mass MBH merger. The chosen incoming black holes also lie within the expected PTA detection range, with masses of $4.44 \times 10^8\,\mathrm{M}_\odot$ and $9.83 \times 10^8\,\mathrm{M}_\odot$. Each incoming model was again modelled as a massive elliptical galaxy consisting of a stellar bulge, a DM halo, following a Sérsic profile in projection with $n = 4$ and an NFW profile respectively. The central MBHs are modelled as Plummer spheres with zero scale length.

For the galaxy models hosting each of the MBHs, I then repeated the methodology of Section 3.3, using observational scaling relations to find the parameters for the bulge and halo components of each galaxy: M_b was derived from the MBH-stellar mass relation (Eqn. 1.6 Kormendy & Ho, 2013; Reines & Volonteri, 2015) with the elliptical parameters $\alpha = 8.95 \pm 0.09$ and $\beta = 1.40 \pm 0.21$. M_h was then determined from the halo-stellar mass scaling relation of Chae et al. (2014). R_{200} was determined from Eqn. 3.1, and the stellar bulge half-mass radius using the Kravtsov (2013) relation. The multi-resolution scheme ‘b’ as described in Section 3.2 was applied to each of the galaxies, as the most effective scheme at improving the central resolution (see Chapter 3).

The galaxy parameters are given in Table 5.1, and the two galaxy models are labelled ‘L’ and ‘H’ for the lower and higher MBH mass ratios respectively, with this group further labelled as binary ’B’ models. The MBH mass ratio, q, was taken in comparison to the

Table 5.1: The parameters of the halo and bulge components of the incoming galaxies: model identifier, mass ratio between the original binary and intruder MBH, intruder MBH mass ($M_\odot$), half-mass radius of the stellar component (kpc), halo mass ($M_\odot$), and NFW scale radius (kpc).

LH	q	MBH Mass	M_b	$R_{1/2}$	M_h	R_{200}
L	0.31	4.44×10^8	6.08×10^{10}	4.27	2.63×10^{12}	284.60
H	0.69	9.83×10^8	6.28×10^{10}	6.28	8.38×10^{12}	418.95

total mass of the previous binary

$$q = \frac{M_{intr}}{M_1 + M_2} \tag{5.1}$$

where M_{intr} is the mass of the intruder MBH.

For each of the incoming galaxies, I then examined two different scenarios: one in which the original MBHs had undergone coalescence at the time of the incoming galaxy intrusion, and one in which the binary had not yet merged.

The starting snapshot from the original galaxy model is taken at 3.2 Gyr, after the galaxy merger from the M6b run and once the hard binary formation is complete. One set-up replaces the central MBH binary with the merger product, of total mass $M_{12} = 1.43 \times 10^9\,\mathrm{M}_\odot$. The other scenario leaves the binary unchanged, as predicted by the higher resolution models. The incoming galaxy models were then generated using the Agama package (Vasiliev, 2019) with the parameters in Table 5.1. The particles were sampled with the 'b' scheme applied to match the original galaxy model, and the particle numbers were adjusted to mimic the original mass ratio in order to prevent segregation between the models. The resulting particles numbers are hence set to $N \simeq 5 \times 10^5$, and the ratio between a halo particle mass and a bulge particle mass in the incoming galaxies is $m_\mathrm{b}/M_\mathrm{bh} = 3.3 \times 10^{-4}$ for L and $m_\mathrm{b}/M_\mathrm{bh} = 2.6 \times 10^{-4}$ for H.

I then set up the initial orbit between the original and intruder galaxy models. The distance at $t = 0.0$ Gyr between the original and the intruder galaxy was set to $D = 223$ kpc at $\sim 5R_s$ for both models, and the initial eccentricity was set to $e = 0.9$, both reflecting the high eccentricities ($e \gtrsim 0.7$) observed in galaxy mergers within cosmological simulations (e.g. Khochfar & Burkert, 2006; Ebrová & Łokas, 2017), and resulting in rapid galaxy mergers that bring down the computational time.

5.2.2 Model Evolution

Each of the models was evolved with the code griffin (Dehnen, 2014), described in detail in Section 2.2, again each using a multipole expansion order $p = 5$. The softening parameter was initially set to $\epsilon = 30$ pc for the star-star interactions, and to $\epsilon_{bh} = 10$ pc for the MBH-MBH and MBH-star interactions for all models. This set-up allows for computational time to be reduced in the early stages of the merger, before the softening length ϵ_{bh} was then reduced to 3 pc after a time ~ 1 Gyr, corresponding to just prior to the end of the dynamical friction phase for all models. The softening kernel employed is a near-Plummer variation for smooth source particles with a density $\rho \propto (r^2 + \epsilon^2)^{-3.5}$.

All simulations were evolved until the binary reached a separation of the order of softening length ϵ_{bh}, below which the dynamical evolution is no longer reliable.

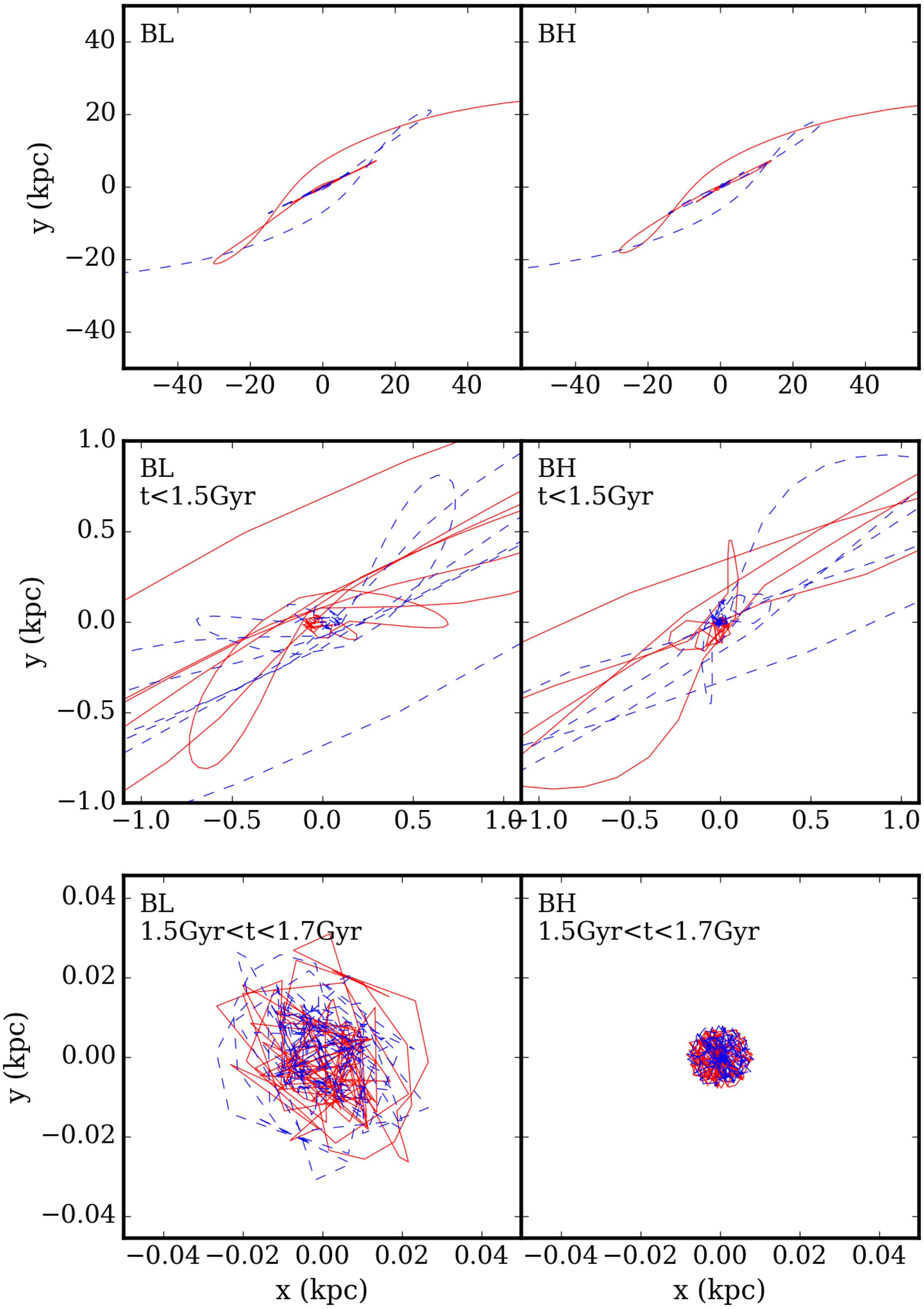

Figure 5.1: The trajectories of the B models for the lower (left panels) and higher mass ratios (right panels). The middle and bottom panels introduce cuts in the time to better show the evolution of the orbits. The H model binary orbit decays more rapidly than the L model, as seen in the bottom panel time cut.

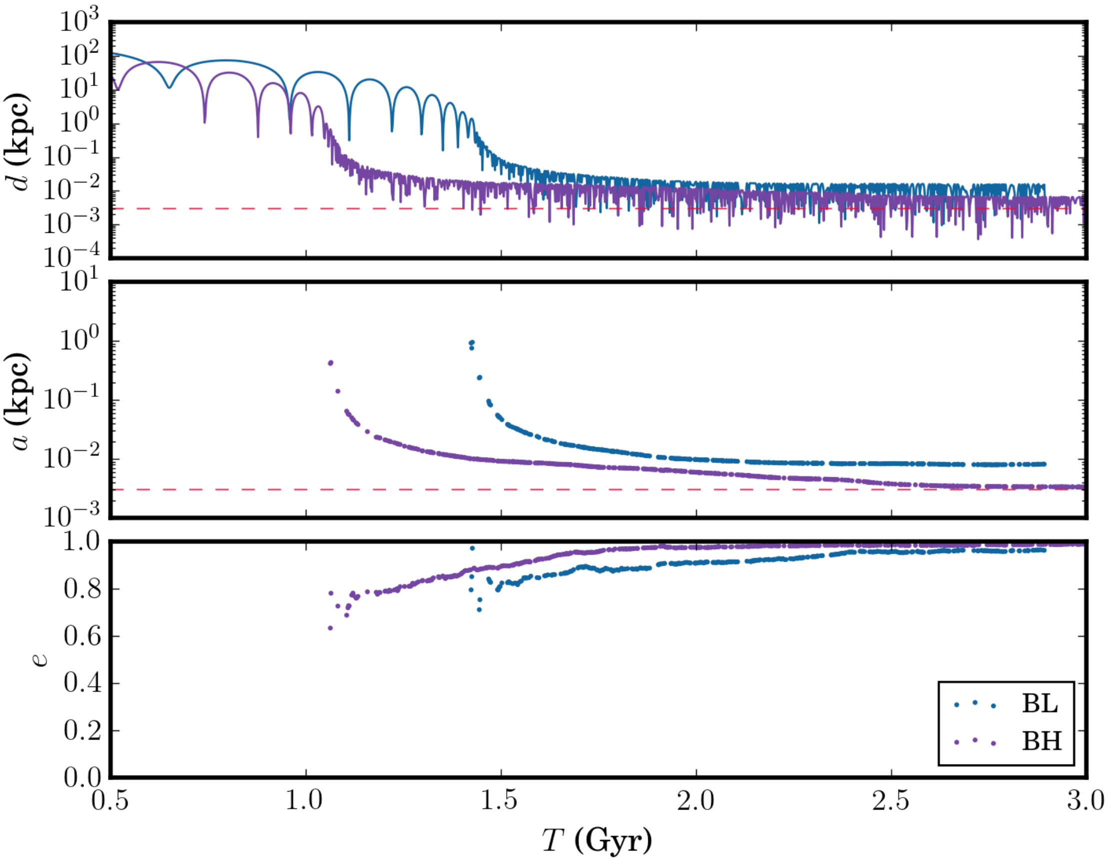

Figure 5.2: The evolution of the separation between the MBHs (top), and the binary parameters the semi-major axis (middle) and eccentricity (bottom) for the B models. The interactions are shown for both the L (blue) and H (purple) scenarios. The dashed line shows the softening length for the BH-BH and BH-particle interactions (red). The lower intruder mass MBH forms a binary noticeably more slowly than the higher mass ratio model.

5.3 MBH Binary Evolution

In this section I present the results of the MBH evolution for the binary models as followed first with GRIFFIN to the softening limit, and beyond this with the semi-analytical prescription to include the GW emission phase as described in Section 4.2.1. It should be noted that I do not impart a recoil velocity to the MBH resulting from binary coalescence. This is motivated by the fact that most recoil kicks are modest (of order $\lesssim 200\,\mathrm{km\,s^{-1}}$) and not sufficient to cause a large displacement or eject the MBH from the host galaxy (Campanelli et al., 2007; Lousto & Zlochower, 2011; Lousto et al., 2012; Nasim et al., 2021). However, including recoil kicks would be of interest for future work - as there is no assumption made here about the spin of MBHs, a kick velocity would need to be sampled from an appropriate distribution, or multiple values would need to be used. The expected effect of such a kick is in the additional growth of a galactic core, as shown in Nasim et al. (2021).

The trajectories of the intruder and original MBHs are shown in Figure 5.1 for the evolution of the BL and BH simulations. The higher mass intruder MBH has a significant effect on the evolution of the orbits, with the BH model binary orbit having decayed

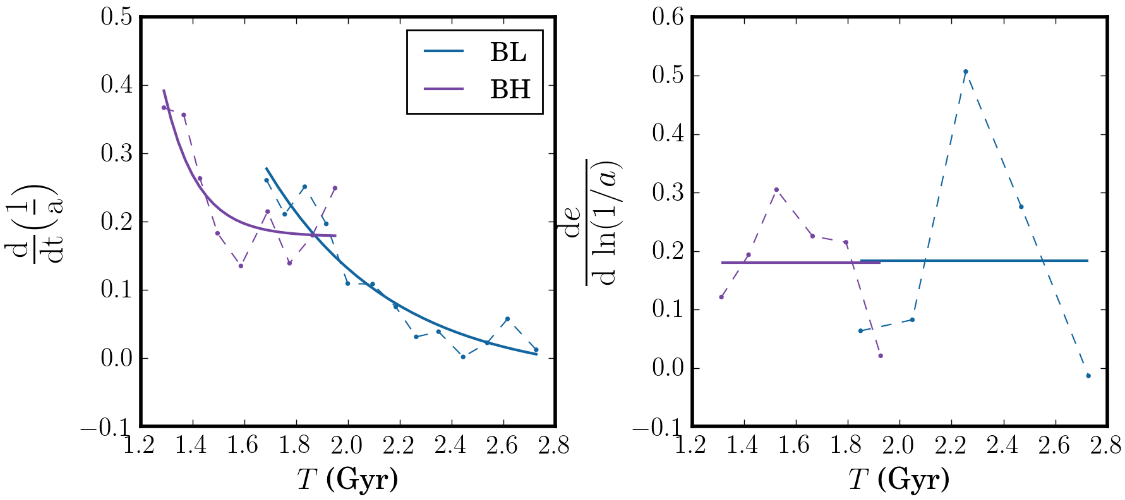

Figure 5.3: The evolution of the hardening rate (left) and the eccentricity growth rate (right), computed numerically for the L (blue) and H (purple) models. The solid lines indicate the exponential fits and calculated mean values for the hardening rate and eccentricity growth rate respectively. The BL hardening rate sinks to oscillate around 0 beyond $t \gtrsim 2.4$ Gyr, indicating a stalled evolution.

noticeably more rapidly than the BL model by $t = 1.5$ Gyr, as expected from Eqn. 3.5 which predicts shorter dynamical friction timescales for heavier mass perturbers.

This faster evolution of the higher mass ratio binary is reflected in the evolution of the separations and orbital parameters for both BL and BH binary models, as shown in Figure 5.2. The BL model takes significantly longer to form a binary than the higher mass ratio model, with a $\simeq 0.3$ Gyr difference between the respective bound binary separation a_f, and a $\simeq 0.5$ Gyr difference between the respective hard binary separation a_h. Further differences between the models can also be discerned from the orbital parameters, as the semi-major axis evolution appears to stall in the BL model at $\gtrsim 2.2$ Gyr, whilst the BH semi-major axis evolution continues to decay. The eccentricity increases to $e > 0.9$ for both models, with the BL eccentricity continuing to evolve past the point at which the semi-major axis appears to stall. Some stochasticity is still evident in the eccentricity evolution, but the models continue to display an improvement over the unrefined M6 and less aggressively refined M6a models of Figure 4.2.

5.3.1 Binary Coalescence Times

For the semi-analytic model, I reproduce the semi-major axis and eccentricity growth for each model to follow the late evolution of the binaries. The time-dependent binary hardening rate $s(t)$ and the eccentricity growth rate K as simulated with GRIFFIN are shown in Figure 5.3 for the BL and BH models, computed numerically using Eqn. 1.17 and Eqn. 1.18 respectively. An exponential decay is fit to $s(t)$ over time, and the eccentricity growth rate remains approximately constant over the evolution and thus I adopt an average for both models. The higher mass intruder MBH displays a slightly slower but similar hardening rate evolution to the previous mergers shown in Figure 4.4, whereas the lower mass intruder sinks to oscillate around 0 beyond $t \gtrsim 2.4$ Gyr, indicating the binary has evolution has stalled. The contribution from GW emission can then calculated be according to the Peters equations Eqn. 1.21 and Eqn. 1.22, and coupled with the equations

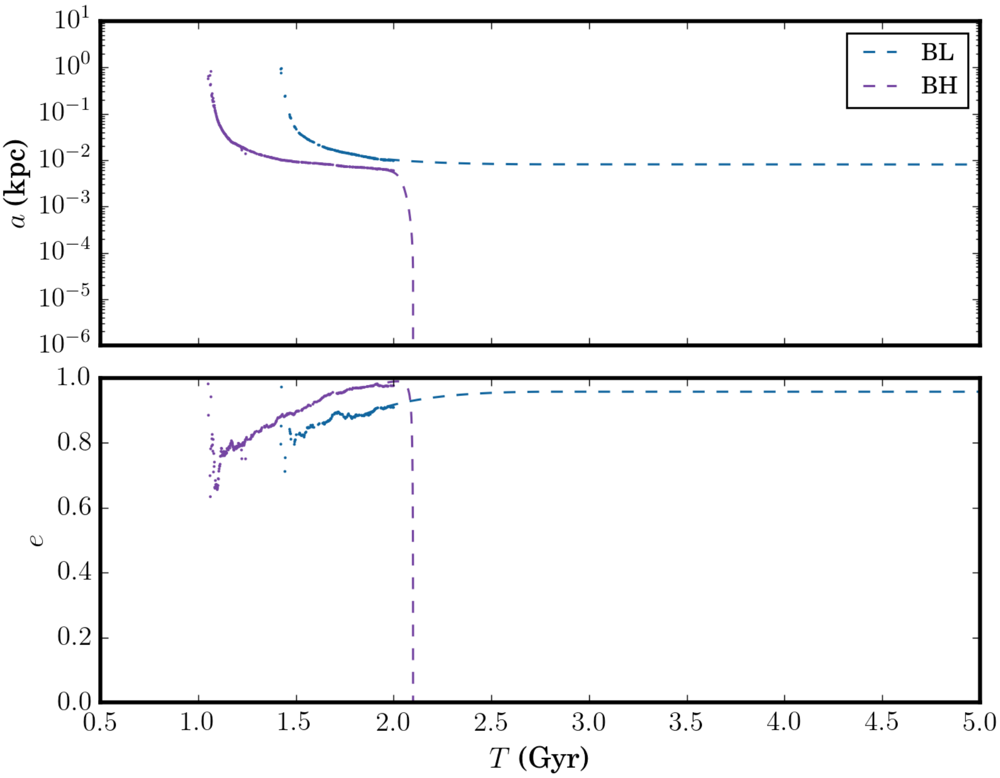

Figure 5.4: The evolution of the semi-major axis a (top) and the eccentricity e (bottom) of the binary with time, from the beginning of the merger. The calculation does not extend beyond a Hubble time but is truncated here to better show the evolution. The evolution simulated with GRIFFIN is shown with scatter points, whilst the subsequent evolution modelled by a semi-analytic model including GWs is shown by dashed lines. The BH model coalesces within ~ 2 Gyr of binary formation, whilst the BH model does not merge.

for stellar hardening Eqn. 1.16 and Eqn. 1.19.

I begin the semi-analytical integration at time 1.85 Gyr for each model. I take an average of the semi-major axis and eccentricity values within ±50 Myr of the starting value, to reduce noise. The resulting evolution of the binary orbital elements is then shown in Figure 5.4, with the predicted trajectories being shown by the dashed lines. The trajectories are consistent with the prior evolution of the semi-major axis. The eccentricity shows a more stochastic evolution, but the predicted trajectories are consistent with the overall trend of the evolution.

The time taken for each model to reach the binary critical separations from the start of the N-body integration, alongside the merger timescales obtained from the semi-analytical extrapolations are given in Table 5.2. The merger timescales are determined as the time from the simulation start for either the eccentricity or the semi-major axis to reach 0. The BH model reaches coalescence at $t = 2.10$ Gyr, but for the BL model GWs do not take over as the dominant hardening method within a Hubble time and the binary does not merge. This is likely due to an insufficient supply of stars to the binary during the stellar scattering phase, after the core scouring of the previous merger has ejected all the stars in the loss cone to large distances. In the future, I plan to run an equivalent model at higher resolution to study if this stalling is merely a numerical effect of insufficient resolution

Table 5.2: Characteristic timescales for the binaries throughout the evolution. From left to right: the simulation identifier, the time to a_f (an estimate of the time spent in the dynamical friction phase), the time until the binary reaches the hard binary separation a_h, the time from end of the numerical integration to coalescence (including stellar hardening and the GW emission phase), and the total time from the start of the simulation to BHB merger.

Scheme	$T_{\rm f}$ (Gyr)	$T_{\rm h}$ (Gyr)	$T_{\rm merg}$ (Gyr)	$T_{\rm tot}$ (Gyr)
BL	1.39	1.75	–	–
BH	1.05	1.21	0.25	2.10

even in the presence of the multi-resolution scheme, or if a core has been carved in the stellar distribution.

5.4 Triples

For the second scenario in which the original MBH binary was left unchanged, I then examine the resulting triple interactions between the binary and the intruder MBH. The lower mass ratio scenario involves an intruder MBH with a mass less than the individual MBHs of the original binary, whereas the intruder MBH of the higher mass ratio scenario has a mass higher than the original MBH.

The trajectories of the intruder and original MBHs are shown in Figure 5.5, with this group further labelled as triple 'T' models, for the evolution of the TL and TH simulations over a selection of timescales. The higher mass intruder MBH again makes a difference, with the TH trajectories show evidence of swapping between the intruder and the original MBHs in the bottom panel between 1.5 Gyr $< t <$ 1.7 Gyr as the intruder MBH (black lines) moves into a closer orbit with an original MBH (blue dashed lines), whilst the other original MBH moves to a wider orbit (red lines).

The same trends identified in the trajectories can then be seen in Figure 5.6 for the TL model and Figure 5.7 for the TH model, which shows the orbital parameters and distances between the MBHs as a function of time. The MBHs are labelled 1 - 2 for the original binary, and the intruder is labelled MBH 3. The dashed line shows the softening length for the BH-BH and BH-particle interactions (red). The intruder MBH in the TL galaxy remnant never disturbs the original binary enough to swap with one of the MBHs, but does experience strong interactions with the intruder MBH the result in it being kicked to a wider orbit without being ejected. The TH model by contrast shows swapping between the MBHs in the inner binary, with the higher mass intruder MBH first taking the place of MBH 1 then exchanges occurring between the original MBHs. Both models appear to briefly form hierarchical triplets: at the later times of $\gtrsim 3.2$ the intruder MBH of the TL galaxy sinks to $\sim$ pc scale distance and the semi-major axes between MBH 3 and the original binary becomes positive and more coherent. The TH model shows a clearer coherent trend in the in the semi-major axes between MBH 3 and the original binary at times 2.1 Gyr $\geq t \geq$ 2.5 Gyr, sinking to a $\sim$ 10 pc scale distance. The same trends are visible again in Figure 5.8, which shows the specific energy of the binaries and provides another clear image of the strong interactions between the MBHs, particularly at times $t \simeq 1.5$ Gyr and $t \simeq 2.0$ Gyr for TL, and $t \simeq 2.4$ Gyr for TH. The exchanges between the MBHs in the inner binary for model TH are also evident here.

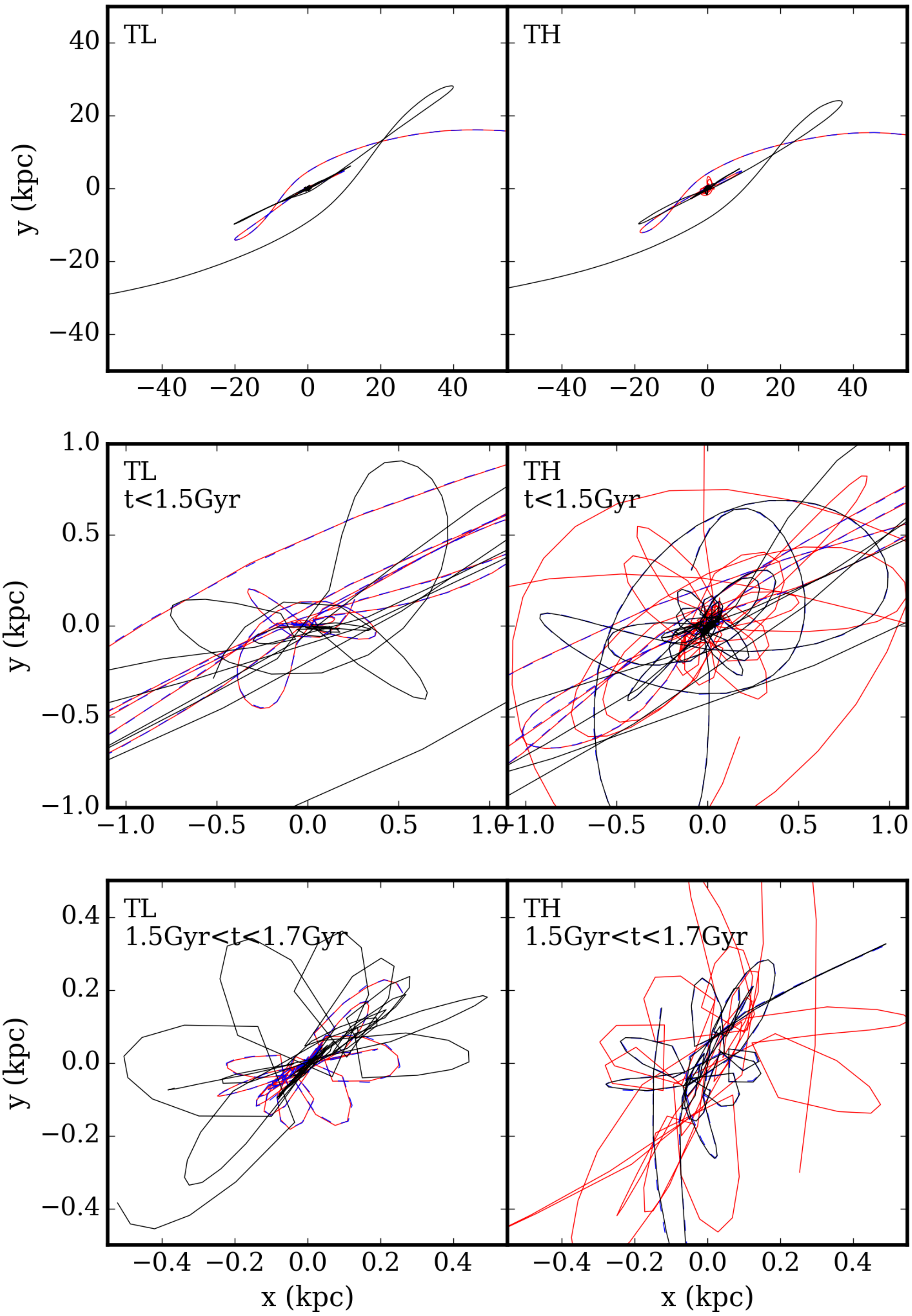

Figure 5.5: The trajectories of the B models for the lower (left panels) and higher mass ratios (right panels). The middle and bottom panels introduce cuts in the time to better see the evolution of the orbits. The intruder MBH is shown with solid black lines, and the original binary MBHs are shown with solid red and dashed blue lines. The TH trajectories show evidence of swapping between the intruder and the original MBHs in the bottom panel between 1.5 Gyr $< t <$ 1.7 Gyr.

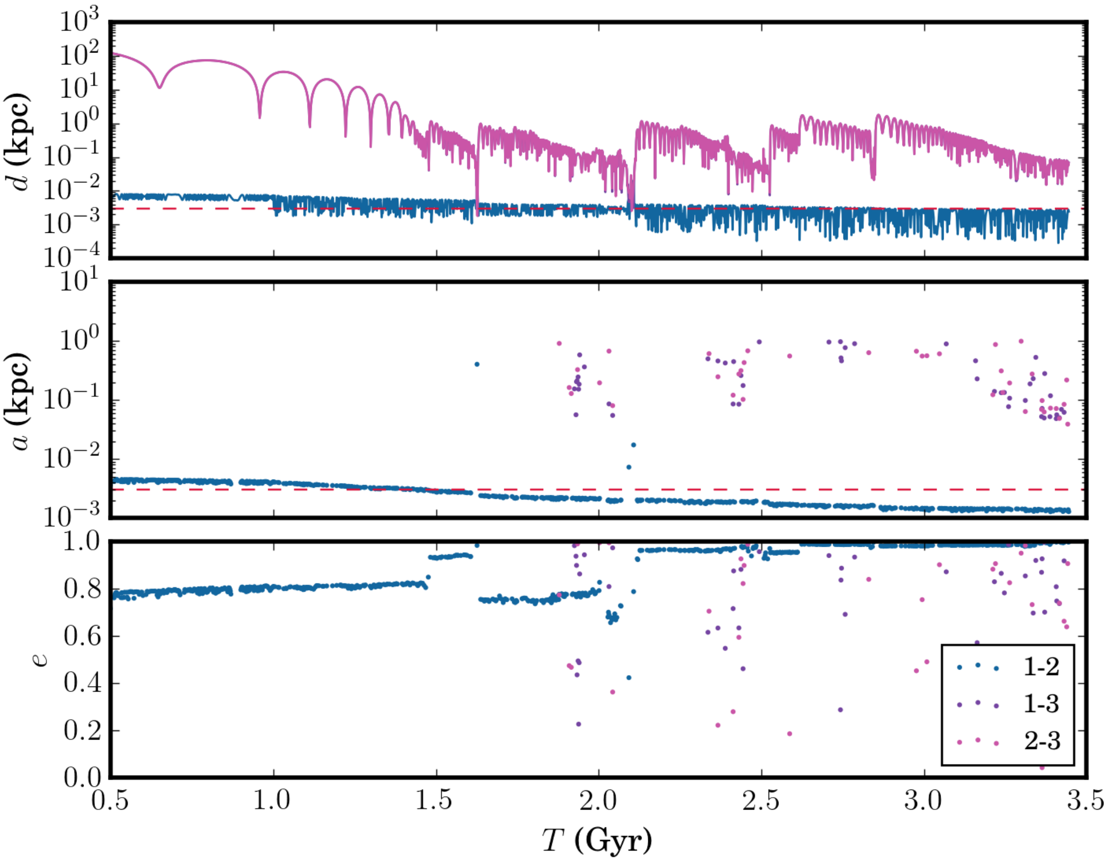

Figure 5.6: The evolution of the separation between the MBHs (top) and the orbital parameters semi-major axis (middle) and eccentricity (bottom) for the T models, in the lower mass ratio scenario. The interactions are shown in three columns between the original MBH binary (1-2), and the intruder MBH (3). The dashed line shows the softening length for the BH-BH and BH-particle interactions (red). The MBH distances and binary parameters show no exchanges take place, but there are several strong interactions with the intruder MBH that incur an effect on the binary eccentricity, e.g. at $t = 1.5\,\mathrm{Gyr}$.

5.5 Conclusions

In this chapter, I have presented the evolution of two sets of galaxy mergers hosting MBHs, taking place after one galaxy has recently experienced a previous merger. Each galaxy model is modelled with a stellar bulge and a DM halo component. One set of models assumes the central MBHs from the prior merger have coalesced, and the other assumes an unmerged binary that can hence form a triple with the intruder MBH. Each of the models has an aggressive multi-resolution scheme implemented to increase the central resolution of the galaxies around the central MBHs. Two different scenarios are presented for both sets of models, in which the intruder MBH has either a higher or lower mass ratio with the original MBH binary. The galaxies were set on initial orbits of $e = 0.9$, in agreement with the high eccentricities observed in cosmological simulations (e.g. Khochfar & Burkert, 2006; Ebrová & Łokas, 2017).

For the models with merged original binaries, I follow the evolution of the resulting binary formed with the intruder MBH first with GRIFFIN and with a semi-analytic model past the softening limit. The trajectories of the orbits and evolution of the distances

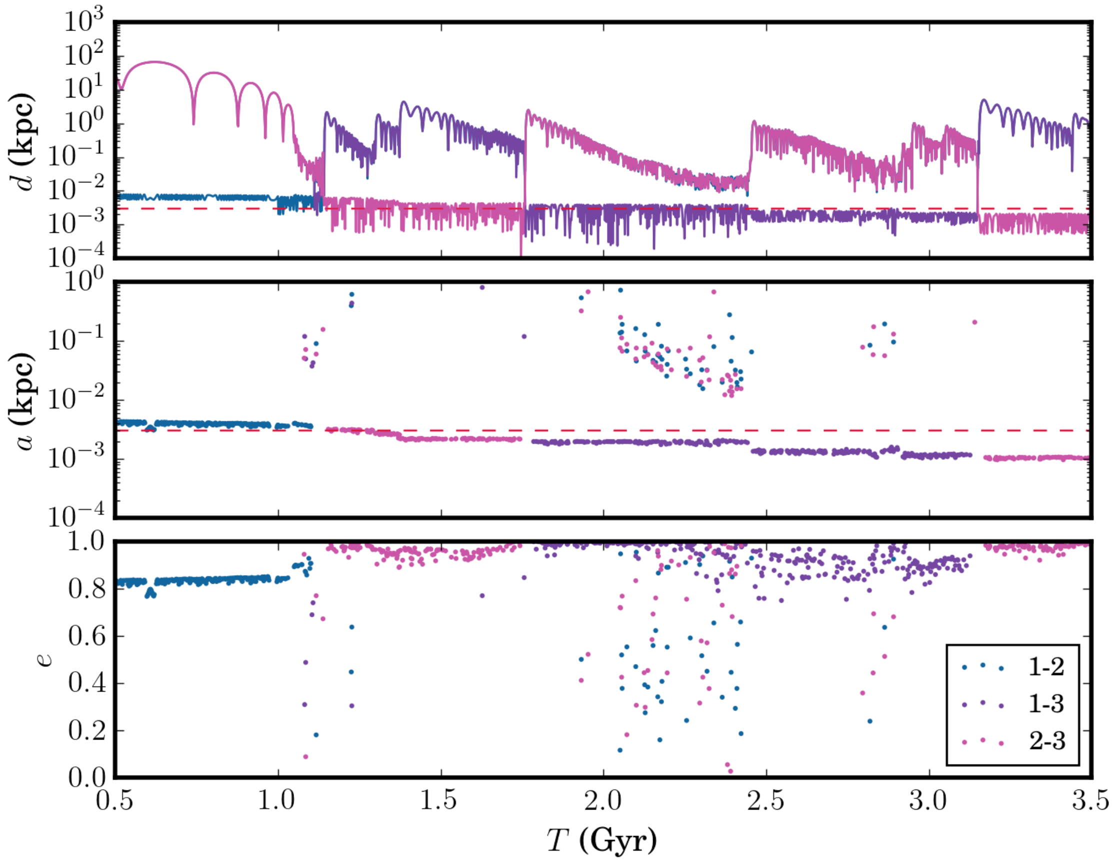

Figure 5.7: The evolution of the separation between the MBHs (top) and the orbital parameters semi-major axis (middle) and eccentricity (bottom) for the T models, in the higher mass ratio scenario. The interactions are shown in three columns between the original MBH binary (1-2), and the intruder MBH (3). The dashed line shows the softening length for the BH-BH and BH-particle interactions (red). The MBH distances and binary parameters show several exchanges, initially between the higher mass intruder MBH and subsequently between the original binary MBHs within the inner binary.

between the MBHs show the higher mass intruder MBH has a significant effect on the timescale of the binary evolution, with the higher mass MBH sinking through dynamical friction faster than its lighter mass counterpart. The lower mass ratio binary orbital parameters also appear to show potential stalling in the semi-major axis, in comparison to the higher mass ratio binary which continues to evolve over the simulation lifetime. I then computed the time to coalescence for the MBH binaries by extending the N-body simulations with a semi-analytical calculation of the evolution of the orbital elements under the combined effects of stellar hardening and GW emission. The binary formed with the lower mass intruder never reaches coalescence as the evolution stalls, but the binary in the higher mass ratio model merges within a Hubble time. A potential cause lies in the core scouring from the previous binary resulting in a reduced particle number at the centre of the remnant galaxy, while the higher mass binary system is better able to overcome this obstacle.

I then examine the evolution of the system of MBHs in the triple case. Both the lower mass and higher mass intruder models for the triple MBHs showcase strong interactions with the intruder MBH and the original MBH binary, with noticeable effects on the orbital

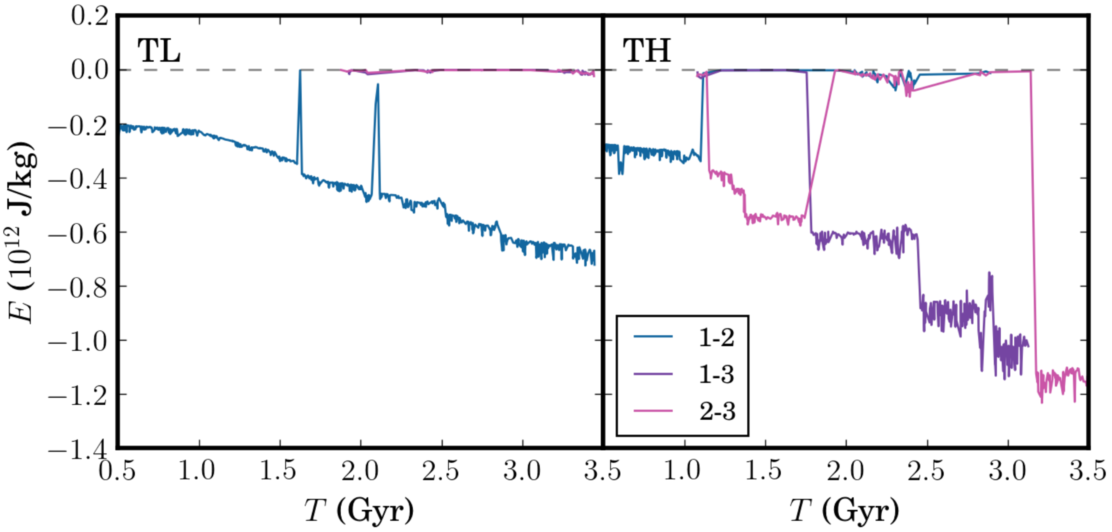

Figure 5.8: The evolution of the binary specific energy for the T models, in the L (left) and H (scenarios). The dashed lines mark the point at which the energy is at 0. The L model shows several strong interactions with the intruder MBH, and the H model shows exchanges between the MBHs as the binary evolves.

parameters calculated between each MBH. Strong interactions in the TH model result in exchanges between the MBHs, with the intruder MBH displacing one of the original binary and subsequently the original MBHs swapping in and out of the inner binary. By contrast, the lower mass MBH in TL never experiences an exchange in the binary, but the strong interactions cause significant discontinuities in the evolution of the binary eccentricity. No ejections are noted amongst the MBHs in either of the models.

More work is needed to explore the results presented here in full. A range of further simulations with varying intruder MBH masses, and different resolutions to investigate the effects of core scouring in greater depth on both the binary and the triple models. The effect of intruder MBHs in the case of an unmerged original binary can then also be investigated further, to observe if for example ejections occur when followed over a longer evolution timescale. It would also be interesting to see if a stable inner binary is formed in a case with MBH exchanges, either through ejection of the outer MBH or extending the evolution of the inner binary past the softening limit to coalescence.

Conclusions

In this chapter, I summarise the work presented in this thesis, which was undertaken with the aim of furthering the understanding of evolution of massive black hole binary mergers. With the coalescence of two MBHs, GWs are released in the low-frequency end of the GW spectrum, a process of significant relevance in light of the recent detection by PTA of a common red signal (e.g. Taylor, 2019). The interpretation of a GWB signal requires a detailed understanding of MBH coalescence timescales. For such an examination of MBH binary mergers, I have utilised a multi-resolution scheme applied to N-body simulations of both isolated and merging galaxies, and followed the mergers both to coalescence and through a subsequent merger, the results of which I conclude here.

6.1 The Multi-Resolution Scheme

The multi-resolution scheme was presented in Chapter 3 with the objective of selectively increasing the resolution at the centre of galaxy simulations where MBH binaries reside, without increasing the total particle number. This will help avoid issues of computational scaling that come with the high resolutions required to adequately resolve these events. Previous uses have only applied such multi-resolution schemes to isolated galaxies (e.g. Cole et al., 2012), here I have investigated the utility of higher central resolutions in merging galaxy models. The scheme first overseeds the galaxy by a set factor, before preferentially removing particles in outer radial zones and simultaneously increasing the remaining particle masses within those zones to compensate and maintain the galaxy density profile.

Here I considered two resolutions that were evolved at $N = 10^6$ and $N = 10^7$, with two variants on the multi-resolution scheme implemented alongside a reference resolution for each. The scheme models were labelled the 'a' and 'b' models, with 'b' the more aggressive implementation at a higher overseeding factor and an increased number of radial zones. I considered both isolated and equal-mass merging galactic simulations with each resolution set, for multi-component galaxies with a stellar bulge and DM halo, all with an MBH planted at the galaxy centres.

Through an analysis of the galaxy properties of both the isolated and merging models, I have shown that the refinement scheme does not impact the stability or the kinematic properties of the models. The central resolution increase is maintained over time, including over the merger events that involve violent mixing of the two galaxies, in line with the 'mixing theorem' which shows N-body simulations should maintain the phase space density at galaxy centres (Dehnen, 2005). Both the 'a' and 'b' schemes are effective at scaling up the resolution, and reduce the spurious particle relaxation and stochastic effects seen in the lower resolution models, particularly the $N = 10^6$ reference resolution. The 'b' model also shows are marked improvement over the 'a' model at the $N = 10^6$ resolution, with trends more in line with the $N = 10^7$ reference resolution within the central region. This is maintained over both the isolated and the merger models. Thus, multi-resolution schemes of the kind laid out in this thesis have been shown to be effective at their goal of raising central resolution without adverse effects on the galaxy properties.

In Chapter 4, I then utilised the increased resolution at the centres of the merging galaxy models to probe the equal-mass MBH binary formation ensuing from their host galaxy mergers and the subsequent binary evolution. The timescales for the mergers of each binary were determined after following the evolution to the softening limit of GRIFFIN, and then down to coalescence with a semi-analytic prescription accounting for three-body interactions and GW emission. Each of the models shows the same behaviour in the MBH separation, but the orbital elements (semi-major axis and eccentricity) prove to be sensitive to the resolution of the different simulations. The eccentricity in particular displays a noticeably increased stochasticity with lower resolution, with only the highest resolution models showing an apparent convergence in the eccentricity for the M7a and M7b models. This has an impact on the computation of the merger timescales which rely on predicting the trajectories of orbital elements past the N-body simulation softening limit, as both the stellar scattering and GW emission depend strongly on eccentricity. The merger timescales follow on from this, showing large variation at lower resolutions, with the difference in total timescales only falling below 0.5 Gyr for the M7a and M7b models.

Previous studies by Nasim et al. (2020); Gualandris et al. (2022) have also reported merger timescale variations at lower resolutions, with Nasim et al. (2020) showing that a total resolution $N > 10^7$ within the half-light radius is required for a reduction in merger timescales of $\sim 10\%$. The models presented in this thesis appear to produce converged results at the resolution of $N(< 5R_{\text{infl}}) = 6 \times 10^4$ for the semi-major axis, but require $N(< 5R_{\text{infl}}) = 10^6$ to approach agreement in the eccentricity evolution. Here I conclude that it is clear that extreme resolution is required to produce reliable results in the MBH binary dynamics. Implementation of the multi-resolution scheme aids in this challenge when combined with an appropriate particle resolution.

6.2 Subsequent Mergers

I have investigated the impact of subsequent galaxy mergers on the remnant galaxies and the evolution of their central MBHs in Chapter 5. I follow the models at resolution of $N = 10^6$ with the aggressive mass refinement scheme applied, with two scenarios: one in which the previous MBH binary is assumed to have merged, and one in which it has not. Two incoming galaxy models are considered for both scenarios, with a lower and a higher mass ratio to the original MBHs.

I first followed the binary models past the GRIFFIN softening limit with the semi-analytic prescription for three-body interactions and GW emission, as before. Core scouring induced by the previous MBH binary merger affects the number of stars within the inner radii, thus reducing the number of stars available to interact with the new MBH binary. This effect is seen in particular in the lower mass ratio binary model which is not able to reach coalescence within a Hubble time as the semi-major axis evolution stalls, likely to be due to the lack of stars within the loss cone. The higher mass ratio model however is better able to overcome this, and reaches coalescence within ~ 1.2 Gyr of the binary formation.

Finally, the triple models both show strong interactions between the original binary and the intruder MBH, with these interactions resulting in exchanges between the MBHs in the inner binary for the higher mass intruder MBH model. The lower mass ratio model does not experience exchanges, but the strong interactions induce significant effects on the inner binary eccentricity. Each strong interaction kicks the outer MBH to a larger orbit, but no ejections take place in either model.

6.3 Future Prospects

Work in the future will build on the multi-resolution scheme I have laid out here. One such change could be sorting the particles based on their binding energy rather than their radial positions - this is easy to implement, and will compensate for particles on radial orbits. An exploration of other varieties of multi-resolution schemes would also be useful, for example increasing the resolution with on-the-fly splitting and merging of simulation particles under certain conditions (such as pre-set times or proximity to MBHs) to raise the resolution, for comparison with simulations using the multi-resolution scheme for initial conditions. The scheme could also be useful in galactic dynamics as none of the properties of the merger remnant examined here are affected by its usage, and potentially implemented in fully cosmological simulations.

For the subsequent mergers, more work in particular is needed to fully investigate the potential effects of prior mergers on both subsequent binary evolution and triple interactions. A suite of simulations with a range of intruder MBH masses at different resolutions can give information on predicted merger timescales for binary models, and in the case of triples look for ejections and potential inner binary mergers over a longer timescales. To explore the effect prior core scouring has on the binary dynamics, an equivalent model to the lower mass ratio binary model run at higher resolution will study if the binary stalling observed here is just a numerical effect of insufficient resolution, or if a genuine galactic core has been formed in the stellar density profile. This can lead to an investigation of full merger trees from the IllustrisTNG simulation, giving a clearer picture of the evolution of an MBH through the mergers in a cosmological environment and hence a better idea of the expected PTA merger rates.

GRIFFIN also supports the inclusion of gas, but the implementation will require adaptations to be suitable to model galaxy mergers. Once GRIFFIN is ready to fully accommodate gas in galaxy evolution, it will mean that future work will not be confined to analysis of the highest mass MBHs, as it will also be possible to investigate the lower mass galaxies with a gas component and include analysis of black hole mergers in the LISA range, alongside mergers in elliptical galaxies that host significant residual gas.

Bibliography

Aarseth S. J., 1963, MNRAS, 126, 223

Aarseth S. J., 2003, Gravitational N-Body Simulations

Abbott B. P. et al., 2016a, Phys. Rev. Lett., 116, 241102

Abbott B. P. et al., 2016b, ApJ, 818, L22

Abbott B. P. et al., 2017, Annalen der Physik, 529, 1600209

Afzal A. et al., 2023, ApJ, 951, L11

Agazie G. et al., 2023a, ApJ, 951, L9

Agazie G. et al., 2023b, ApJ, 951, L8

Aggarwal N. et al., 2021, Living Reviews in Relativity, 24, 4

Alexander T., Hopman C., 2009, ApJ, 697, 1861

Amaro-Seoane e. a., 2013, GW Notes, 6, 4

Amaro-Seoane P. et al., 2022, arXiv e-prints, arXiv:2203.06016

Amaro-Seoane P. et al., 2017, ArXiv e-prints

Antoniadis J. et al., 2023a, arXiv e-prints, arXiv:2306.16227

Antoniadis J. et al., 2023b, arXiv e-prints, arXiv:2306.16214

Antoniadis J. et al., 2023c, arXiv e-prints, arXiv:2306.16224

Antonini F., Gieles M., Gualandris A., 2019, MNRAS, 486, 5008

Antonini F., Merritt D., 2012, ApJ, 745, 83

Armano M. et al., 2016, Phys. Rev. Lett., 116, 231101

Armano M. et al., 2018, Phys. Rev. Lett., 120, 061101

Arzoumanian Z. et al., 2020, ApJ, 905, L34

Arzoumanian Z. et al., 2018, ApJ, 859, 47

Askar A., Davies M. B., Church R. P., 2021, MNRAS, 502, 2682

Bailes M. et al., 2021, Nature Reviews Physics, 3, 344

Barack L. et al., 2019, Classical and Quantum Gravity, 36, 143001

Barausse E., Dvorkin I., Tremmel M., Volonteri M., Bonetti M., 2020, ApJ, 904, 16

Barnes J., Hut P., 1986, Nature, 324, 446

Barnes J. E., 2012, MNRAS, 425, 1104

Becerra F., Greif T. H., Springel V., Hernquist L. E., 2015, MNRAS, 446, 2380

Begelman M. C., Blandford R. D., Rees M. J., 1980, Nature, 287, 307

Begelman M. C., Blandford R. D., Rees M. J., 1984, Reviews of Modern Physics, 56, 255

Begelman M. C., Volonteri M., Rees M. J., 2006, MNRAS, 370, 289

Behroozi P. S., Wechsler R. H., Conroy C., 2013, ApJ, 770, 57

Beifiori A., Courteau S., Corsini E. M., Zhu Y., 2012, MNRAS, 419, 2497

Bellovary J. M., Cleary C. E., Munshi F., Tremmel M., Christensen C. R., Brooks A., Quinn T. R., 2019, MNRAS, 482, 2913

Bentz M. C., Peterson B. M., Netzer H., Pogge R. W., Vestergaard M., 2009, ApJ, 697, 160

Bentz M. C., Peterson B. M., Pogge R. W., Vestergaard M., Onken C. A., 2006, ApJ, 644, 133

Bernardi M. et al., 2003, AJ, 125, 1866

Berti E., Yagi K., Yang H., Yunes N., 2018, General Relativity and Gravitation, 50, 49

Bertola F., Capaccioli M., 1975, ApJ, 200, 439

Binney J., Tremaine S., 2008, Galactic Dynamics: Second Edition

Blaes O., Lee M. H., Socrates A., 2002, ApJ, 578, 775

Blanchet L., 2014, Living Reviews in Relativity, 17, 2

Blandford R., Meier D., Readhead A., 2019, ARA&A, 57, 467

Bond H. E., 1981, ApJ, 248, 606

Bonetti M., Haardt F., Sesana A., Barausse E., 2016, MNRAS, 461, 4419

Bonetti M., Haardt F., Sesana A., Barausse E., 2018a, MNRAS, 477, 3910

Bonetti M., Sesana A., Barausse E., Haardt F., 2018b, MNRAS, 477, 2599

Bortolas E., Gualandris A., Dotti M., Read J. I., 2018, MNRAS, 477, 2310

Bortolas E., Gualandris A., Dotti M., Spera M., Mapelli M., 2016, MNRAS, 461, 1023

Burke-Spolaor S. et al., 2019, A&A Rev., 27, 5

Camp J. B., Cornish N. J., 2004, Annual Review of Nuclear and Particle Science, 54, 525

Campanelli M., Lousto C., Zlochower Y., Merritt D., 2007, ApJ, 659, L5

Cappellari M. et al., 2006, MNRAS, 366, 1126

Carlsten S. G., Greene J. E., Beaton R. L., Greco J. P., 2022, ApJ, 927, 44

Carr B., Kohri K., Sendouda Y., Yokoyama J., 2021, Reports on Progress in Physics, 84, 116902

Carr B. J., 2003, in Quantum Gravity: From Theory to Experimental Search, Giulini D., Kiefer C., Laemmerzahl C., eds., Vol. 631, pp. 301–321

Chae K.-H., Bernardi M., Kravtsov A. V., 2014, MNRAS, 437, 3670

Chan C.-H., Piran T., Krolik J. H., Saban D., 2019, ApJ, 881, 113

Chandran A., 2022, Spot the difference: Imaging sagittarius a* and m87*. Accessed on June 16, 2023

Chandrasekhar S., 1943, ApJ, 97, 255

Chen Z.-C., Wu Y.-M., Huang Q.-G., 2021, arXiv e-prints, arXiv:2109.00296

Christensen N., 2019, Reports on Progress in Physics, 82, 016903

Ciotti L., Bertin G., 1999, A&A, 352, 447

Clark P. C., Glover S. C. O., Klessen R. S., 2008, ApJ, 672, 757

Cole D. R., Dehnen W., Read J. I., Wilkinson M. I., 2012, MNRAS, 426, 601

Collins M. L. M. et al., 2013, ApJ, 768, 172

Colpi M. et al., 2019, arXiv e-prints, arXiv:1903.06867

Cornish N., Robson T., 2017, in Journal of Physics Conference Series, Vol. 840, Journal of Physics Conference Series, p. 012024

Creighton J., Anderson W., 2011, Gravitational-Wave Physics and Astronomy: An Introduction to Theory, Experiment and Data Analysis.

Curyło M., Bulik T., 2022, A&A, 660, A68

Davies M. B., Miller M. C., Bellovary J. M., 2011, ApJ, 740, L42

Davies R. L., Efstathiou G., Fall S. M., Illingworth G., Schechter P. L., 1983, ApJ, 266, 41

Dawson K. S. et al., 2013, AJ, 145, 10

Dayal P., Rossi E. M., Shiralilou B., Piana O., Choudhury T. R., Volonteri M., 2019, MNRAS, 486, 2336

De Lucia G., Springel V., White S. D. M., Croton D., Kauffmann G., 2006, MNRAS, 366, 499

de Vaucouleurs G., 1948, Annales d'Astrophysique, 11, 247

de Zeeuw T., 1985, MNRAS, 216, 273

Deane R. P. et al., 2014, Nature, 511, 57

Dehnen W., 2000, ApJ, 536, L39

Dehnen W., 2001, MNRAS, 324, 273

Dehnen W., 2002, Journal of Computational Physics, 179, 27

Dehnen W., 2005, MNRAS, 360, 892

Dehnen W., 2014, Computational Astrophysics and Cosmology, 1, 1

Dehnen W., 2017, MNRAS, 472, 1226

Dehnen W., Read J. I., 2011, European Physical Journal Plus, 126, 55

Desroches L.-B., Quataert E., Ma C.-P., West A. A., 2007, MNRAS, 377, 402

Desvignes G. et al., 2016a, MNRAS, 458, 3341

Desvignes G. et al., 2016b, MNRAS, 458, 3341

Devecchi B., Volonteri M., 2009, ApJ, 694, 302

Di Matteo T., Springel V., Hernquist L., 2005, Nature, 433, 604

Dirkes A., 2018, International Journal of Modern Physics A, 33, 1830013

Dong-Páez C. A., Volonteri M., Beckmann R. S., Dubois Y., Trebitsch M., Mangiagli A., Vergani S., Webb N., 2023, arXiv e-prints, arXiv:2303.00766

Dosopoulou F., Antonini F., 2017, ApJ, 840, 31

Dressler A., Richstone D. O., 1988, ApJ, 324, 701

Driver S. P. et al., 2018, MNRAS, 475, 2891

Dubinski J., 1996, New Astronomy, 1, 133

Dubois Y., Volonteri M., Silk J., 2014, MNRAS, 440, 1590

Dubois Y., Volonteri M., Silk J., Devriendt J., Slyz A., Teyssier R., 2015, MNRAS, 452, 1502

Düchting N., 2004, Phys. Rev. D, 70, 064015

Dutton A. A., Macciò A. V., 2014, MNRAS, 441, 3359

Dyer C. C., Ip P. S. S., 1993, ApJ, 409, 60

Eardley D. M., Lee D. L., Lightman A. P., Wagoner R. V., Will C. M., 1973, Phys. Rev. Lett., 30, 884

Ebrová I., Łokas E. L., 2017, ApJ, 850, 144

Einstein A., 1915, Sitzungsberichte der Königlich Preussischen Akademie der Wissenschaften, 844

Einstein A., 1916, Sitzungsberichte der Königlich Preußischen Akademie der Wissenschaften (Berlin, 688

Einstein A., 1918, Sitzungsberichte der Königlich Preussischen Akademie der Wissenschaften, 154

El-Badry K. et al., 2023, MNRAS, 518, 1057

eLISA Consortium, 2013, arXiv e-prints, arXiv:1305.5720

Ene I. et al., 2018, MNRAS, 479, 2810

Enoki M., Inoue K. T., Nagashima M., Sugiyama N., 2004, ApJ, 615, 19

Event Horizon Telescope Collaboration et al., 2022, ApJ, 930, L12

Faber S. M., Jackson R. E., 1976, ApJ, 204, 668

Faber S. M. et al., 1997, AJ, 114, 1771

Fabian A. C., 2012, ARA&A, 50, 455

Fabian A. C. et al., 2000, MNRAS, 318, L65

Fakhouri O., Ma C.-P., Boylan-Kolchin M., 2010, MNRAS, 406, 2267

Ferguson H. C., Binggeli B., 1994, A&A Rev., 6, 67

Ferrarese L., 2002, ApJ, 578, 90

Ferrarese L. et al., 2006a, ApJ, 644, L21

Ferrarese L. et al., 2006b, ApJS, 164, 334

Ferrarese L., Ford H., 2005, Space Sci. Rev., 116, 523

Fong W., Darve E., 2009, Journal of Computational Physics, 228, 8712

Franx M., Illingworth G. D., 1988, ApJ, 327, L55

Frigo M., Naab T., Rantala A., Johansson P. H., Neureiter B., Thomas J., Rizzuto F., 2021, MNRAS, 508, 4610

Gebhardt K. et al., 2000, ApJ, 539, L13

Gebhardt K. et al., 2001, AJ, 122, 2469

Genel S. et al., 2014, MNRAS, 445, 175

Genzel R., Eisenhauer F., Gillessen S., 2010, Reviews of Modern Physics, 82, 3121

Giacobbo N., Mapelli M., 2018, MNRAS, 480, 2011

Gillessen S., Eisenhauer F., Trippe S., Alexander T., Genzel R., Martins F., Ott T., 2009, ApJ, 692, 1075

Goddi C. et al., 2019, The Messenger, 177, 25

Goncharov B. et al., 2021, MNRAS, 502, 478

Graham A. W., 2013, in Planets, Stars and Stellar Systems. Volume 6: Extragalactic Astronomy and Cosmology, Oswalt T. D., Keel W. C., eds., Vol. 6, pp. 91–140

Graham A. W., 2019, Publ. Astron. Soc. Aus., 36, e035

Graham A. W., Driver S. P., 2005, Publ. Astron. Soc. Aus., 22, 118

Graham A. W., Erwin P., Trujillo I., Asensio Ramos A., 2003, AJ, 125, 2951

GRAVITY Collaboration et al., 2018, A&A, 618, L10

Greene J. E., Strader J., Ho L. C., 2020, ARA&A, 58, 257

Greif T. H., Johnson J. L., Klessen R. S., Bromm V., 2008, MNRAS, 387, 1021

Gualandris A., Khan F. M., Bortolas E., Bonetti M., Sesana A., Berczik P., Holley-Bockelmann K., 2022, MNRAS, 511, 4753

Gualandris A., Merritt D., 2012a, ApJ, 744, 74

Gualandris A., Merritt D., 2012b, ApJ, 744, 74

Gualandris A., Read J. I., Dehnen W., Bortolas E., 2017, MNRAS, 464, 2301

Gültekin K. et al., 2009, ApJ, 698, 198

Habouzit M., Volonteri M., Dubois Y., 2017, MNRAS, 468, 3935

Haehnelt M. G., Kauffmann G., 2002, MNRAS, 336, L61

Haemmerlé L., Klessen R. S., Mayer L., Zwick L., 2021, A&A, 652, L7

Haemmerlé L., Woods T. E., Klessen R. S., Heger A., Whalen D. J., 2018, ApJ, 853, L3

Haiman Z., Loeb A., 2001, ApJ, 552, 459

Harfst S., Gualandris A., Merritt D., Spurzem R., Portegies Zwart S., Berczik P., 2007, New Astronomy, 12, 357

Harris W. E., Pritchet C. J., McClure R. D., 1995, ApJ, 441, 120

Harrison C. M., Costa T., Tadhunter C. N., Flütsch A., Kakkad D., Perna M., Vietri G., 2018, Nature Astronomy, 2, 198

Hawking S., 1971, MNRAS, 152, 75

Hazard C., Mackey M. B., Shimmins A. J., 1963, Nature, 197, 1037

Heckman T. M., Best P. N., 2014, ARA&A, 52, 589

Heger A., Fryer C. L., Woosley S. E., Langer N., Hartmann D. H., 2003, ApJ, 591, 288

Hellings R. W., Downs G. S., 1983, ApJ, 265, L39

Hernandez D. M., Bertschinger E., 2018, MNRAS, 475, 5570

Hickox R. C., Alexander D. M., 2018, ARA&A, 56, 625

Hirano S., Hosokawa T., Yoshida N., Umeda H., Omukai K., Chiaki G., Yorke H. W., 2014, ApJ, 781, 60

Hoffman L., Loeb A., 2006, ApJ, 638, L75

Hoffman L., Loeb A., 2007, MNRAS, 377, 957

Hopkins P. F., Richards G. T., Hernquist L., 2007, ApJ, 654, 731

Hu J., 2008, MNRAS, 386, 2242

Hu W., Dodelson S., 2002, ARA&A, 40, 171

Hubble E. P., 1926, ApJ, 64, 321
Inayoshi K., Visbal E., Haiman Z., 2020, ARA&A, 58, 27
Izquierdo-Villalba D., Sesana A., Bonoli S., Colpi M., 2022a, MNRAS, 509, 3488
Izquierdo-Villalba D., Sesana A., Colpi M., 2022b, arXiv e-prints, arXiv:2207.04064
Johnson J. L., Bromm V., 2007, MNRAS, 374, 1557
Johnson J. L., Whalen D. J., Li H., Holz D. E., 2013, ApJ, 771, 116
Kalaja A., Bellomo N., Bartolo N., Bertacca D., Matarrese S., Musco I., Raccanelli A., Verde L., 2019, , 2019, 031
Katz M. L., Kelley L. Z., Dosopoulou F., Berry S., Blecha L., Larson S. L., 2020, MNRAS, 491, 2301
Kauffmann G., Colberg J. M., Diaferio A., White S. D. M., 1999, MNRAS, 303, 188
Kauffmann G., Haehnelt M., 2000, MNRAS, 311, 576
Kelley L. Z., Blecha L., Hernquist L., 2017, MNRAS, 464, 3131
Kelley L. Z., Blecha L., Hernquist L., Sesana A., Taylor S. R., 2018, MNRAS, 477, 964
Kelvin L. S. et al., 2014, MNRAS, 439, 1245
Kesden M., Sperhake U., Berti E., 2010, ApJ, 715, 1006
Khan F. M., Berczik P., Just A., 2018, A&A, 615, A71
Khan F. M., Mirza M. A., Holley-Bockelmann K., 2020, MNRAS, 492, 256
Khochfar S., Burkert A., 2006, A&A, 445, 403
King A., 2003, ApJ, 596, L27
Klypin A., Holtzman J., 1997, arXiv e-prints, astro
Klypin A., Prada F., 2018, MNRAS, 478, 4602
Kormendy J., 1982, Saas-Fee Advanced Course, 12, 115
Kormendy J., Djorgovski S., 1989, ARA&A, 27, 235
Kormendy J., Fisher D. B., Cornell M. E., Bender R., 2009, ApJS, 182, 216
Kormendy J., Ho L. C., 2013, ARA&A, 51, 511
Kozai Y., 1962, AJ, 67, 591
Kravtsov A. V., 2013, ApJ, 764, L31
Krtička J., Kubát J., 2006, A&A, 446, 1039
Krumholz M. R., Tan J. C., 2007, ApJ, 654, 304
Lacey C. G. et al., 2016, MNRAS, 462, 3854
Lagos C. d. P., Tobar R. J., Robotham A. S. G., Obreschkow D., Mitchell P. D., Power C., Elahi P. J., 2018, MNRAS, 481, 3573
Larson R. B., 1975, MNRAS, 173, 671
Lauer T. R. et al., 1995, AJ, 110, 2622
Leach R., 1981, ApJ, 248, 485
Lee K. J., Wex N., Kramer M., Stappers B. W., Bassa C. G., Janssen G. H., Karuppusamy R., Smits R., 2011, MNRAS, 414, 3251
Li K., Bogdanović T., Ballantyne D. R., 2020, ApJ, 896, 113
Li L.-X., 2012, MNRAS, 424, 1461
Lidov M. L., 1962, Planet. Space Sci., 9, 719
Liu B., Lai D., 2017, ApJ, 846, L11
Liu X. et al., 2019, ApJ, 887, 90
Łokas E. L., Mamon G. A., 2001, MNRAS, 321, 155
Lousto C. O., Zlochower Y., 2008, Phys. Rev. D, 77, 024034
Lousto C. O., Zlochower Y., 2011, Phys. Rev. Lett., 106, 041101
Lousto C. O., Zlochower Y., Dotti M., Volonteri M., 2012, Phys. Rev. D, 85, 084015
Lupi A., Colpi M., Devecchi B., Galanti G., Volonteri M., 2014, MNRAS, 442, 3616
Madau P., Rees M. J., 2001, ApJ, 551, L27

Maiolino R. et al., 2017, Nature, 544, 202
Makino J., 1991, ApJ, 369, 200
Makino J., Hut P., Kaplan M., Saygın H., 2006, New Astronomy, 12, 124
Mamon G. A., Łokas E. L., 2005, MNRAS, 363, 705
Mannerkoski M., Johansson P. H., Pihajoki P., Rantala A., Naab T., 2019, ApJ, 887, 35
Mannerkoski M., Johansson P. H., Rantala A., Naab T., Liao S., 2021, ApJ, 912, L20
Mannerkoski M., Johansson P. H., Rantala A., Naab T., Liao S., Rawlings A., 2022, ApJ, 929, 167
Mannerkoski M., Rawlings A., Johansson P. H., Naab T., Rantala A., Springel V., Irodotou D., Liao S., 2023, arXiv e-prints, arXiv:2306.04963
Mapelli M., 2016, MNRAS, 459, 3432
Marconi A., Hunt L. K., 2003, ApJ, 589, L21
Marinacci F. et al., 2018, MNRAS, 480, 5113
Martín-Navarro I., Brodie J. P., Romanowsky A. J., Ruiz-Lara T., van de Ven G., 2018, Nature, 553, 307
Martín-Navarro I., Mezcua M., 2018, ApJ, 855, L20
Martynov D. V. et al., 2016, Phys. Rev. D, 93, 112004
Massey R., Kitching T., Richard J., 2010, Reports on Progress in Physics, 73, 086901
Matthews T. A., Sandage A. R., 1963, ApJ, 138, 30
McConnell N. J., Ma C.-P., 2013, ApJ, 764, 184
McConnell N. J., Ma C.-P., Gebhardt K., Wright S. A., Murphy J. D., Lauer T. R., Graham J. R., Richstone D. O., 2011, Nature, 480, 215
McGaugh S. S., Schombert J. M., Bothun G. D., de Blok W. J. G., 2000, ApJ, 533, L99
Melott A. L., Shandarin S. F., Splinter R. J., Suto Y., 1997, ApJ, 479, L79
Merritt D., 2013, Dynamics and Evolution of Galactic Nuclei
Merritt D., Mikkola S., Szell A., 2007, ApJ, 671, 53
Merritt D., Milosavljević M., 2005, Living Reviews in Relativity, 8, 8
Middleton H., Sesana A., Chen S., Vecchio A., Del Pozzo W., Rosado P. A., 2021, MNRAS, 502, L99
Mikkola S., Aarseth S. J., 1993, Celestial Mechanics and Dynamical Astronomy, 57, 439
Mikkola S., Merritt D., 2008, AJ, 135, 2398
Milosavljević M., Merritt D., 2001, ApJ, 563, 34
Milosavljević M., Merritt D., 2003a, ApJ, 596, 860
Milosavljević M., Merritt D., 2003b, in American Institute of Physics Conference Series, Vol. 686, The Astrophysics of Gravitational Wave Sources, Centrella J. M., ed., pp. 201–210
Minkowski R., 1960, ApJ, 132, 908
Mo H., van den Bosch F. C., White S., 2010, Galaxy Formation and Evolution
Moore C. J., Cole R. H., Berry C. P. L., 2015, Classical and Quantum Gravity, 32, 015014
Morawski J., Giersz M., Askar A., Belczynski K., 2018, MNRAS, 481, 2168
More S., van den Bosch F. C., Cacciato M., Skibba R., Mo H. J., Yang X., 2011, MNRAS, 410, 210
Morganti R., 2017, Frontiers in Astronomy and Space Sciences, 4, 42
Moster B. P., Somerville R. S., Maulbetsch C., van den Bosch F. C., Macciò A. V., Naab T., Oser L., 2010, ApJ, 710, 903
Naab T., Ostriker J. P., 2017, ARA&A, 55, 59
Naiman J. P. et al., 2018, MNRAS, 477, 1206
Naoz S., 2016, ARA&A, 54, 441

Nasim I., Gualandris A., Read J., Dehnen W., Delorme M., Antonini F., 2020, MNRAS, 497, 739

Nasim I. T., Gualandris A., Read J. I., Antonini F., Dehnen W., Delorme M., 2021, MNRAS, 502, 4794

Navarro J. F., Frenk C. S., White S. D. M., 1996, ApJ, 462, 563

Nelson D. et al., 2019, MNRAS, 490, 3234

Neumayer N., Seth A., Böker T., 2020, A&A Rev., 28, 4

Neureiter B., de Nicola S., Thomas J., Saglia R., Bender R., Rantala A., 2023, MNRAS, 519, 2004

Novikov I. D., Polnarev A. G., Starobinskii A. A., Zeldovich I. B., 1979, A&A, 80, 104

Olivier G. M., Lopez L. A., Rosen A. L., Nayak O., Reiter M., Krumholz M. R., Bolatto A. D., 2021, ApJ, 908, 68

Omukai K., Tsuribe T., Schneider R., Ferrara A., 2005, ApJ, 626, 627

Orlofsky N., Pierce A., Wells J. D., 2017, Phys. Rev. D, 95, 063518

Ostriker E. C., 1999, ApJ, 513, 252

Pacucci F., Loeb A., 2020, ApJ, 895, 95

Pacucci F., Natarajan P., Volonteri M., Cappelluti N., Urry C. M., 2017, ApJ, 850, L42

Padovani P. et al., 2017, A&A Rev., 25, 2

Passy J.-C., Bryan G. L., 2014, ApJS, 215, 8

Peebles P. J. E., 1972, ApJ, 178, 371

Perera B. B. P. et al., 2019, MNRAS, 490, 4666

Peters P. C., 1964, Physical Review, 136, 1224

Peterson B. M., 1993, PASP, 105, 247

Pezzulli E., Valiante R., Schneider R., 2016, MNRAS, 458, 3047

Pezzulli E., Volonteri M., Schneider R., Valiante R., 2017, MNRAS, 471, 589

Pfister H., Volonteri M., Dubois Y., Dotti M., Colpi M., 2019, MNRAS, 486, 101

Piana O., Dayal P., Volonteri M., Choudhury T. R., 2021, MNRAS, 500, 2146

Pillepich A. et al., 2019, MNRAS, 490, 3196

Planck Collaboration et al., 2016, A&A, 594, A13

Planck Collaboration et al., 2020, A&A, 641, A6

Plummer H. C., 1911, MNRAS, 71, 460

Pontzen A., Roškar R., Stinson G., Woods R., 2013, pynbody: N-Body/SPH analysis for python. Astrophysics Source Code Library, record ascl:1305.002

Pontzen A., Tremmel M., Roth N., Peiris H. V., Saintonge A., Volonteri M., Quinn T., Governato F., 2017, MNRAS, 465, 547

Portegies Zwart S. F., McMillan S. L. W., 2002, ApJ, 576, 899

Postman M., Geller M. J., 1984, ApJ, 281, 95

Power C., Navarro J. F., Jenkins A., Frenk C. S., White S. D. M., Springel V., Stadel J., Quinn T., 2003, MNRAS, 338, 14

Press W. H., Schechter P., 1974, ApJ, 187, 425

Pringle J. E., Rees M. J., 1972, A&A, 21, 1

Quinlan G. D., 1996, New Astronomy, 1, 35

Quinlan G. D., Hernquist L., 1997, New Astronomy, 2, 533

Rantala A., Pihajoki P., Johansson P. H., Naab T., Lahén N., Sawala T., 2017, ApJ, 840, 53

Read J. I. et al., 2021, MNRAS, 501, 978

Reardon D. J. et al., 2016a, MNRAS, 455, 1751

Reardon D. J. et al., 2016b, MNRAS, 455, 1751

Reardon D. J. et al., 2023, ApJ, 951, L6

Rees M. J., 1984, ARA&A, 22, 471

Regan J. A., Downes T. P., Volonteri M., Beckmann R., Lupi A., Trebitsch M., Dubois Y., 2019, MNRAS, 486, 3892

Reines A. E., Volonteri M., 2015, ApJ, 813, 82

Ricarte A., Natarajan P., 2018, MNRAS, 474, 1995

Ricarte A., Tremmel M., Natarajan P., Quinn T., 2019, MNRAS, 489, 802

Romano J. D., Cornish N. J., 2017, Living Reviews in Relativity, 20, 2

Rosado P. A., Sesana A., Gair J., 2015, MNRAS, 451, 2417

Rubin V. C., Burstein D., Ford, W. K. J., Thonnard N., 1985, ApJ, 289, 81

Rubin V. C., Ford, W. Kent J., 1970, ApJ, 159, 379

Ryder L., 2009, Introduction to General Relativity

Savorgnan G. A. D., Graham A. W., Marconi A., Sani E., 2016, ApJ, 817, 21

Schawinski K., Urry M., Treister E., Simmons B., Natarajan P., Glikman E., 2011, ApJ, 743, L37

Scheel M. A., Boyle M., Chu T., Kidder L. E., Matthews K. D., Pfeiffer H. P., 2009, Phys. Rev. D, 79, 024003

Schmidt M., 1963, Nature, 197, 1040

Schwarzschild K., 1916, Abh. Konigl. Preuss. Akad. Wissenschaften Jahre 1906,92, Berlin,1907, 1916, 189

Seigar M. S., James P. A., 2002, MNRAS, 337, 1113

Sérsic J. L., 1963, Boletin de la Asociacion Argentina de Astronomia La Plata Argentina, 6, 41

Sersic J. L., 1968, Atlas de Galaxias Australes

Sesana A., 2013, Classical and Quantum Gravity, 30, 224014

Sesana A., 2016, Phys. Rev. Lett., 116, 231102

Sesana A., Barausse E., Dotti M., Rossi E. M., 2014, ApJ, 794, 104

Sesana A., Haardt F., Madau P., 2008a, ApJ, 686, 432

Sesana A., Vecchio A., Colacino C. N., 2008b, MNRAS, 390, 192

Sesana A., Vecchio A., Volonteri M., 2009, MNRAS, 394, 2255

Shajib A. J., Treu T., Birrer S., Sonnenfeld A., 2021, MNRAS, 503, 2380

Shannon R. M. et al., 2014, MNRAS, 443, 1463

Shannon R. M. et al., 2015, Science, 349, 1522

Smidt J., Whalen D. J., Johnson J. L., Surace M., Li H., 2018, ApJ, 865, 126

Smith B. D., Regan J. A., Downes T. P., Norman M. L., O'Shea B. W., Wise J. H., 2018, MNRAS, 480, 3762

Soltan A., 1982, MNRAS, 200, 115

Somerville R. S., Hopkins P. F., Cox T. J., Robertson B. E., Hernquist L., 2008, MNRAS, 391, 481

Springel V., 2005, MNRAS, 364, 1105

Springel V., Hernquist L., 2003, MNRAS, 339, 289

Springel V. et al., 2018, MNRAS, 475, 676

Stiefel E., Kustaanheimo P., 1965, Journal für die reine und angewandte Mathematik, 218, 204

Tanaka T., Haiman Z., 2009, ApJ, 696, 1798

Taylor S., 2019, in American Astronomical Society Meeting Abstracts, Vol. 233, American Astronomical Society Meeting Abstracts #233, p. 149.15

Taylor S. R., Vallisneri M., Ellis J. A., Mingarelli C. M. F., Lazio T. J. W., van Haasteren R., 2016, ApJ, 819, L6

The LIGO Scientific Collaboration et al., 2021, arXiv e-prints, arXiv:2111.03606

Thomas J., Saglia R. P., Bender R., Erwin P., Fabricius M., 2014, ApJ, 782, 39

Thorne K. S., Price R. H., 1975, ApJ, 195, L101

Toyouchi D., Inayoshi K., Li W., Haiman Z., Kuiper R., 2023, MNRAS, 518, 1601

Tremmel M., Governato F., Volonteri M., Quinn T. R., 2015, MNRAS, 451, 1868

Trenti M., Hut P., 2008, arXiv e-prints, arXiv:0806.3950

Trujillo I., Erwin P., Asensio Ramos A., Graham A. W., 2004, AJ, 127, 1917

Tsai C.-W. et al., 2018, ApJ, 868, 15

Valiante R. et al., 2021, MNRAS, 500, 4095

Vasiliev E., 2019, MNRAS, 482, 1525

Vasiliev E., Antonini F., Merritt D., 2014, ApJ, 785, 163

Vasiliev E., Antonini F., Merritt D., 2015, ApJ, 810, 49

Vasiliev E., Merritt D., 2013, ApJ, 774, 87

Verbiest J. P. W. et al., 2016, MNRAS, 458, 1267

Vogelsberger M., Marinacci F., Torrey P., Puchwein E., 2020, Nature Reviews Physics, 2, 42

Volonteri M., 2010, A&A Rev., 18, 279

Volonteri M., Begelman M. C., 2010, MNRAS, 409, 1022

Volonteri M., Dubois Y., Pichon C., Devriendt J., 2016, MNRAS, 460, 2979

Volonteri M., Lodato G., Natarajan P., 2008, MNRAS, 383, 1079

Volonteri M., Natarajan P., 2009, MNRAS, 400, 1911

Volonteri M., Rees M. J., 2005, ApJ, 633, 624

Volonteri M., Silk J., Dubus G., 2015, ApJ, 804, 148

von Hoerner S., 1960, ZAp, 50, 184

Walker M. G., Mateo M., Olszewski E. W., Peñarrubia J., Evans N. W., Gilmore G., 2009, ApJ, 704, 1274

Wang F. et al., 2021a, ApJ, 908, 53

Wang F. et al., 2021b, ApJ, 907, L1

Wang L., Spurzem R., Aarseth S., Nitadori K., Berczik P., Kouwenhoven M. B. N., Naab T., 2015, MNRAS, 450, 4070

Wanner G., 2019, Nature Physics, 15, 200

Wechsler R. H., Tinker J. L., 2018, ARA&A, 56, 435

White S. D. M., Frenk C. S., 1991, ApJ, 379, 52

White S. D. M., Rees M. J., 1978, MNRAS, 183, 341

Windhorst R. A. et al., 2018, ApJS, 234, 41

Wolf J., Martinez G. D., Bullock J. S., Kaplinghat M., Geha M., Muñoz R. R., Simon J. D., Avedo F. F., 2010, MNRAS, 406, 1220

Woods T. E., Patrick S., Elford J. S., Whalen D. J., Heger A., 2021, ApJ, 915, 110

Xu H. et al., 2023, Research in Astronomy and Astrophysics, 23, 075024

Yang J. et al., 2020, ApJ, 897, L14

Yu Q., 2002, MNRAS, 331, 935

Yu Q., Tremaine S., 2002, MNRAS, 335, 965

Zwicky F., 1933, Helvetica Physica Acta, 6, 110